LEGIBILITY NOTICE

A major purpose of the Technical Information Center is to provide the broadest dissemination possible of information contained in DOE's Research and Development Reports to business, industry, the academic community, and federal, state and local governments.

Although a small portion of this report is not reproducible, it is being made available to expedite the availability of information on the research discussed herein.

ORNL/tr--88/31

DE89 001417

MEASUREMENT OF THE HADRONIC BACKGROUND IN THE IDENTIFICATION OF MUONS

Reinhard Leuchs

Translated from German.* Diploma thesis in Physics submitted to Fachabteilung fuer Mathematik und Physik, Rheinisch-Westfaelische Technische Hochschule, October 1982, 62 pp. plus 5 tables and 44 figures.

Prepared for the
OAK RIDGE NATIONAL LABORATORY
Oak Ridge, Tennessee 37831
operated by
MARTIN MARIETTA ENERGY SYSTEMS, INC.
for the
U.S. DEPARTMENT OF ENERGY
under Contract No. DE-AC05-84OR21400

* By LANGUAGE SERVICES, Knoxville, Tennessee

ORNL/TR-88/31

MEASUREMENT OF THE HADRONIC BACKGROUND IN THE IDENTIFICATION OF MUONS

by

Reinhard Leuchs

Diploma Thesis in Physics
Submitted to the
Division for Mathematics and Physics of the
Rhenish-Westphalian Technological Institute

(Fachabteilung für Mathematik und Physik
der Rheinisch-Westfälischen Technischen Hochschule

Aachen

Prepared in the
Third Physical Institute, Chair A

Contents

Contents

Lass die Moleküle rasen
was sie auch zusammenknobeln!
Lass das Tüfteln, lass das Hobeln,
heilig halte die Ekstasen!*
(C. Morgenstern)

---

*) Let the molecules race, whatever they may cobble together! Cease fiddling, cease smoothing, consider ecstasies holy!

1) Introduction

In the year 1967 Glashow, Salam, and Weinberg developed a theory which united the electromagnetic and weak interactions (WEI67). This theory requires three new particles as the carriers of the weak force, the massive intermediate vector bosons W^+, W^-, and Z^o, while the electromagnetic force is exchanged by means of zero-mass neutral photons. W^+ and W^- mediate the charged current, and Z^o the neutral current. In this theory the masses of the bosons depend on only a single free parameter, the Weinberg angle Θ_W:

$$M_W^2 = M_Z^2 \cos^2(\Theta_W) = \frac{\pi \alpha \sqrt{2}}{G} \frac{1}{\sin^2(\Theta_W)}$$

With the value of the Weinberg angle known today by experimental measurements to be $\sin^2(\Theta_W) = 0.229 \pm 0.010$ (KIM81) one obtains the masses $M_W = 78$ GeV and $M_Z = 89$ GeV. For several years now there have been ample experimental indications that this theory is correct (GSW). However, because of the large mass of the bosons it has not been possible to date to produce these particles directly and detect them.

For this reason it was proposed by C. Rubbia in 1976 at the Aachen Neutrino Conference that the existing super Proton Synchrotron in the European Nuclear Research Center CERN be rebuilt as a $p\bar{p}$ storage ring, and thus be able to reach a center-of-mass energy of 540 GeV (RUB76). This reconstruction has now been accomplished.

Experimentally it is easiest to detect the vector bosons without large impurities by their purely leptonic decays:

$$p + \bar{p} \rightarrow Z^{o} + \text{hadrons}, \qquad Z^{o} \rightarrow \mu^{+} + \mu^{-} \text{ or } e^{+} + e^{-}$$

$$p + \bar{p} \rightarrow W^{+} + \text{hadrons}, \qquad W^{+} \rightarrow \mu^{+} + \nu \text{ or } e^{+} + \nu$$

In such measurements Z^{o} is easier to recognize than the charged boson, for which it is never possible to measure anything but the muon energy, due to a resonance peak in the distribution of the invariant mass of the lepton pairs, while the neutrino unobservably carries away a part of the total energy.

However, even using the $p\bar{p}$ storage ring, the production rate remains very low. Even if the desired luminosity of $L = 10^{30}\ cm^{-2}\ s^{-1}$ is achieved, only about one charged boson is produced per hour. It is necessary to filter these events out of a large number of other charged particles. With about 5×10^{4} interactions per second, approximately 10^{9} of these background events are produced in the time in which a single charged boson is created. In order to detect the decay products of these bosons the muon detector was built in the Third Physics Institute as a contribution to the UA1 Experiment at the $p\bar{p}$ storage ring, and a muon trigger was built. In this diploma thesis we shall begin by studying the properties of the muon detector. In the second part of the work we shall investigate the effect that the hadronic background has on the muon identification, and how it may be possible to reduce this background. The background consists primarily of hadrons that reach the muon detector and may there be mistaken for a muon.

2) Muon Identification

As it passes through material a muon interacts only electromagnetically and via the weak force, and is therefore capable of traversing large material thicknesses. In contrast, hadrons, due to their being subject to the strong force, produce cascades of particles. After a few interaction path lengths such a cascade is almost completely absorbed. High-energy electrons and photons produce an electromagnetic cascade that can be removed by an absorber.

For this reason a typical muon filter consists of a thick block of material. Electrons, photons, and hadrons with a typical energy of 10 GeV cannot, for example, penetrate as much as 1.5 meters of iron, while a muon with the same starting energy loses only 1.75 GeV, and its direction will have changed only by about 20 milli-radians due to multiple scattering.

2.1) Separating Muons from Electrons and Photons

As a charged particle passes through matter it continuously loses energy by collisions with the shell electrons of the atoms. This causes the atoms to become excited or even ionized. Under the assumption that the mass of the particle M is very much larger than the mass of the electron m_e, the energy loss due to ionization is given by the Bethe-Bloch equation (ROS52):

$$-\frac{dE}{dx_{ion}} = 4\pi N_0 e^4 \frac{Z}{A} \frac{z^2}{m_e v^2} \left(\ln \frac{2 m_e v^2}{I} \gamma^2 - \beta^2 \right)$$

This energy loss is shown in Fig. 1 as function of $P/Mc = \beta\gamma$, where

N_o = the Loschmidt number
e = the electron charge
Z = the atomic number
A = the atomic weight
z = the particle charge
m_e = the mass of the electron
v = the velocity of the particle
I = the ionization potential
β = v/c
= $(1 - \beta^2)^{-1/2}$, the Lorentz factor.

The energy loss has the following properties:

1) It depends only on the particle velocity v.
2) As the velocity increases the curve initially falls off as $1/v^2$.
3) At P/Mc = 3 the curve has a broad minimum, which is called the minimum ionization region.
4) As P/Mc increases the energy loss increases in proportion to ln (γ).

In addition to the energy loss due to ionization charged particles also lose energy due to radiative effects, such as, for example, bremsstrahlung. The total radiative energy loss calculates to be

$$-\frac{dE}{dx}_{rad} = E \frac{4 N_o Z^2 r_e^2}{137 A} \left(\frac{m_e}{M}\right)^2 \ln\left(\frac{183}{Z^{1/3}}\right)$$

where $r_e = (e^4)/(m_e^2 c^4)$

The radiative loss is proportional to the square of the mass ratios (M/m_e). In comparison to the electron ($M/m_e = 1$) the muon ($M/m_e = 1/207$) loses hardly any energy due to radiation.

The energy loss rises with the atomic number of the absorber. ($-dE/dx$ is proportional to Z^2).

From this it follows that high-energy electrons can best be separated from muons by using an absorber with large Z (lead!). Energetic photons can also be filtered out using such a material since the can produce $e^+ - e^-$ pairs, and be scattered by the Compton effect. The total energy of the particles is completely transferred to the medium.

The absorption process of a high-energy electron or photon is due to a combination of all the processes described above. An electromagnetic cascade, a shower, is produced: An electron radiates a photon, this photon then produces a pair, which again radiates photons, etc. The number of electrons and photons in the cascade increases rapidly. This avalanche-like effect terminates when the energy of the photons is no longer high enough to cause the production of $e^+ - e^-$ pairs. The number of particles then decreases exponentially. Above 1 GeV the cross sections for pair production and bremsstrahlung are almost constant, and it is possible to define a mean free path which is called the radiation length:

$$X_o = 716(A/Z^2)\ln(183\ Z^{-1/3}) \quad (\text{in g/cm}^2)$$

The radiation length is a measure of the absorption capability of a material for electromagnetic processes.

There is a critical energy, ϵ, at which the energy loss due to radiation is equal to that due to ionization:

$$\epsilon = 600 \text{ MeV}/Z.$$

Fabian describes a parameterization of the shower (FAB80):

1) The shower maximum is found at a depth $t_{max} = \ln(E_o/\epsilon) - 1$ (radiation lengths).
2) The longitudinal shower depth D amounts to $D = t_{max} + \lambda_{att}$ (radiation lengths) (λ_{att} indicates how strongly the shower is attenuated.)
3) The longitudinal and transverse shower spreads are correlated (Bathow et al. BAT70). The shape is scale-invariant.

Fig. 2 shows the particle multiplicity in an electromagnetic shower.

In addition all charged particles undergo Coulomb scattering as they traverse matter; this is caused by elastic scattering from atoms of the medium. This results in a mean solid angle of scattering of (ROS41) :

$$\langle \Theta^2 \rangle = \left(\frac{E_s}{P \beta c} \right)^2 \frac{X}{X_o} \quad \text{with} \quad E_s = \left(\frac{4\pi}{2\alpha} \right)^{1/2} m_e c^2 = 21 \text{ MeV}$$

2.2) Separating Muons from Hadrons

As hadrons pass through matter they interact predominantly via the strong interaction. They may excite nucleons or collide with them inelastically. Inelastic collisions produce further hadrons. The majority of these are pions. The secondary hadrons then also interact, thus creating a

hadronic shower. Since there are many different processes that contribute to particle production and each one is quite complicated when considered in detail, it is difficult to formulate a simple theory of hadronic showers. Nevertheless, some statements can be made:

1) A nuclear absorption length L_{abs} exists. Beyond the shower maximum, in the fall-off region of the curve, the decay, which is, to first approximation, exponential, is characterized by L_{abs}. For mesons in iron Fabian gives a value of L_{abs} = 19 cm (FAB80).
2) In every hadron shower an electromagnetic cascade also develops. since the collisions with the nuclei also produce neutral pions which decay into two photons. The electromagnetic component develops far more rapidly than the hadronic one since the radiation length X_o is smaller than the absorption length L_{abs} (IWA79).
3) The shape of the hadron shower has been determined experimentally and parameterized. (HOL78, FLO78, BOC80) The energy deposited as function of the penetration depth X is given by

$$dE = X^{\alpha} \cdot \exp\{X\beta/L_{abs}\}$$

where α, β, and L_{abs} are all energy-dependent. Grant has determined the energy dependence of the absorption length. For π^--induced showers in iron it varies between 15 and 30 cm (GRA75).
4) The length of the shower is proportional to ln(E).
5) The lateral extent of the shower is about one absorption length L_{abs}.

Typical shower curves will be found in Fig. 3. Because of its very small absorption length, iron is particularly good for absorbing hadrons.

3) The Major Components of the UA1 Detector

The UA1 experiment marked the first time that events from $p\bar{p}$ collisions with a center-of-mass energy of 2 x 270 GeV were investigated. Since no experiments of this kind had ever been done before in this completely new energy domain, it was necessary initially to design the UA1 detector to be as versatile as possible. For this reason it was given the following properties:

1) Complete detection of the events over the total solid angle,
2) exact momentum measurement of all charged particles,
3) precise energy measurement of the electromagnetic and hadronic particles in calorimeters, and
4) good muon identification.

Since it is not possible to combine all these properties in a single device, the UA1 detector is modularly constructed out of various individual detectors; these will now be briefly described. A detailed description of the experiment is to be found in (UA1). Figs. 4 and 5 show the detector.

The central detector is a self-supporting cylinder 6 m long and 2.2 m in diameter, which is subdivided into 6 modules. The individual modules are large drift chambers with several wire planes and 18 cm drift separation distances. The spatial resolution in the drift direction, in other words perpendicular to the anode wires is about 0.25 mm. Along the anode wires the track coordinate is determined by comparing the pulse heights at the two ends of the wire; in this direction the attainable resolution is about 2 cm. By means of this two-dimensional read-out the points on a particle track

can be measured at intervals of 1 cm. Along the direction of drift the smallest distance separating two just separable points is about 3 cm. The central detector is placed in a horizontal homogeneous magnetic field of 0.7 T. From the path curvature of charged particles in the magnetic field it is possible to determine the momentum. From the pulse height measurement along the particle track one determines the specific energy loss dE/dx in the gas. If the momentum is known the particle mass can be determined from the measurement of the energy loss.

The central detector is surrounded by the electromagnetic calorimeters. Here the energies of the electrons and photons that have been created are measured. Of particular interest is the most precise possible determination of the energies of highly relativistic electrons from the decay of the intermediate bosons. The above-named particles produce an electromagnetic shower in the calorimeter, which is totally absorbed in the 26 radiation lengths of the calorimeter. On the basis of the cylindrical geometry one distinguishes between the lateral surfaces which cover a production angle of $25^{\circ} < \Theta < 90^{\circ}$, and the end caps for the range up to 5°. The lateral surfaces consist of 48 half-moon-shaped segments, the so-called "gondolas," with a width of 22.5 cm each and a thickness of 36 cm. The are made in the form of a lead/scintillator sandwich made of 120 times 1.2 mm lead and 1.5 mm polystyrene. The energy resolution amounts to $\Delta E/E = 16\% /\sqrt{E}$. Since the gondolas are read out at both ends, it is possible to measure the azimuth angle from a pulse-height comparison.

The inner detector and the electromagnetic calorimeter are located inside a rectangular spool which produces a

dipole field perpendicular to the beam tube of strength 0.7 T over a volume of 80 m^3.

Outside the magnet coil the flux of the magnetic field is returned through a large iron yoke which completely encloses the inner components of the detector. The lateral domain, that is to say $30^o < \Theta < 90^o$ is covered by 16 C-shaped elements. These have a width of 90 cm and a thickness of 96 cm. The yoke is interrupted in its thickness dimension 16 times to accommodate scintillator plates. Thus a calorimeter is formed of a total of about 5 nuclear absorption lengths. The end areas for $5^o < \Theta < 30^o$ also consist of an iron-scintillator sandwich, which, however, has a thickness of 7 absorption lengths. The energy resolution amounts to $\Delta E/E = 80\% / \sqrt{E}$. The hadron calorimeters are subdivided into blocks of about 90 x 90 cm^2; each block consists of a forward and a rear section which are read out separately.

4) The Muon Detector

With the described arrangement of the detector components of the UA1 experiment one would, in the ideal case, expect only muons to be left outside the calorimeters, which can then be detected in the muon detector. The coordinates of such a muon track are measured independently of each other with the aid of drift tubes in two projections oriented perpendicular to one another. The anode wire placed in the center of the drift tube sees two drift spaces of 7 cm length each, one on its left and one on its right. This creates a left-right ambiguity if one wants to use the drift time to determine the location. This ambiguity is resolved by using a second layer of drift tubes which are cemented onto the first layer displaced by half a tube width. This also serves, at the same time, to compensate for the inefficiency caused by mechanically necessitated dead space between the tubes. In order to measure the other coordinate of the track, a second double plane of drift tubes is added at 90° to the first. In order to achieve good angular resolution of a few milli-radians a second chamber is located at a separation distance of 585 mm. This angular resolution corresponds to the multiple scattering angle of muons from the decay of the intermediate bosons. Fig. 6 shows the spatial arrangement. The large lever arm is also necessary in order to make it possible to be able to decide, only a few microseconds after the interaction, whether the muon comes from the interaction zone.

Such modules, consisting of two chambers placed one behind the other, are used to cover the forward direction, the lateral direction, upward direction of the slab-shaped

UA1 experiment (Fig. 4). In order to simplify the construction it was considered desirable that there be only two different types of chambers for covering the regions mentioned above. The large chambers have the following dimensions: length 5.55 m, width 3.75 m. The small chambers have the same length, but a width of 3.15 m. (See Table 1.)

As the arrangement of the chambers shown in Fig. 4 makes clear, the modules are overlapped at the edges in order to achieve the best possible acceptance. Fig. 8 shows the distribution of the modules, the overlapping of two regions is shown in Fig. 7. The uncovered areas in the region around $\phi = 90^{\circ}$ are necessary in order to be able to bring the cables and other connections from the inner detectors to the outside. In the forward direction an area of 2 x 2 m^2 around the beam tube was left open. In this region the identification of muons is extremely difficult due to the high background caused by beam-gas interactions and punch-through, as well as decay muons.

In the floor region below the UA1 experiment the supports for the magnets as well as the tracks for the detectors prevent large areas from being covered with muon chambers. For this reason two additional chamber types were therefore developed, the large and small floor chambers, which exactly fit into the supports. They consist of four layers of 5.55-meter long drift tubes which are oriented in only one direction, but are read out at booth ends. The missing second coordinate is determined from the transit time difference of the pulses along the tubes.

All the chambers taken together cover an area of 670 m^2, the covered solid angle amounts to 95% of 4π. With the

desired spatial resolution of 1 mm it is possible to achieve an angular resolution of 4 milli-radians. This is sufficient for measuring the coulomb scattering angle of the muons in the calorimeters, and thus determine their momenta. If one does not take the drift-time into account but only the on-off information from the tubes, then with 15-cm-wide tubes one still achieves an angular resolution of 150 milli-radians, if one demands that at least three of the four layers in one projection must have fired. These values are for those regions where the muons impinge upon the chambers at incidence angles less than 0^{o}.

4.1) Construction

To begin with, a layer of drift tubes is spread out on a 4 x 6 m^2 flat and very precise steel table, and each tube in turn is straightened out. Since the aluminum tubes are continuous extrusions, the exhibit small bends of several mm over a length of 5 m. For this reason they are fastened to the table along their length by numerous small wedges which fasten onto the outer slots in the profile. The ends of the tubes are positioned by means of bolts that fit into the collimator. Thus it is made certain that later the position of the anode wires, which is determined by the ends of the tubes, is exactly known to within 0.25 mm. The second layer is then placed upon the first and also positioned exactly. The two layers are then cemented together with epoxy resin into a double plane. A second double plane is then cemented to the first one in the orthogonal orientation. The chambers are covered at top and bottom with a metal cover sheet which has a cellular structure. This cellular structure gives the chamber high stability. The ends of the tubes open into a

gas shaft with a cover to which all connections to the gas supply are attached. Next to the gas shafts on the upper side of the chambers are cable channels in which all the electrical supply is placed. At one end is the high voltage supply, at the other end are the preamplifiers and the signal cable connectors. Each tube is individually connected to the high voltage supply and to the preamplifier by way of gas-tight feed-throughs. Thus it is possible at any time to perform repairs on the electric components of a tube. Fig. 9 shows one end of a chamber.

This type of construction has several advantages:

- Due to their cell structure the chambers are stable enough to be able to withstand being evacuated. It thus becomes possible to outgas the PVC components in the 3 tubes. When there is a gas change after evacuation, it is not necessary to spend a long time sparging with fresh gas.
- The tubes with a wall thickness of 3 mm are well shielded electrically from each other. Spill-over of the signals from one tube to an adjacent one was only very rarely observed.
- Since altogether only four types of chambers are made, the chambers may be interchanged with one another so as to be able to carry out repairs.
- The chambers are so robust that the positions of the wires relative to each other and relative to reference points attached to the exterior do not change.

4.2 The Drift Tube

4.2.1 Mode of Operation

The drift tube is a detector device with high spatial resolution for ionizing particles. When charged particles pass through a gas they ionize the gas molecules along their path. The ions and electrons thus created can be separated from each other by an electric field. They move along the gradient of the electric potential towards the anode and cathode. Because of their smaller mass the electrons arrive at the anode considerably faster than the ions to the cathode. If the anode is given the form of a thin wire, then in its vicinity the field strength becomes very large, and increases in inverse proportion to the distance r from the anode. As they fall into the potential of the anode the electrons gain more and more energy. They can give off this energy to the gas molecules by collisions. They may either excite the atoms or ionize them. if the field strength is high enough the result is an avalanche-like multiplication of the ion-electron pairs, which may attain a multiplication of as much as 10^7. Thus a charge pulse is created on the anode, which can then be further processed by a sensitive amplifier.

Aside from the field strength, the drift speed of the primary electrons is also dependent on the gas mixture used in the chamber. If one integrates the known drift velocity $v_D(E, \text{Gas})$ from the time t_o of the particle passage through the chamber up to the measured drift time t_D, then one obtains the location of the particle passage x in the drift tube.

The amplification factor of the drift tube is adjusted by means of the anode voltage. We operate our tubes in the so-called proportional region in which the anode signal is proportional to the number of primary electrons produced. The charge avalanche remains sharply localized along the wire. If the anode voltage is increased, one leaves the proportional region and moves into the Geiger-Müller region. Here the signal pulses are very large, but no longer proportional to the primary ionization. Furthermore, because of the photons released in the course of the very high gas amplification the charge avalanche also spreads along the wire, and the tube becomes insensitive for several microseconds, since the secondary electrons cannot be moved away from the anode fast enough, and thus shield the anode. More detailed descriptions of the complicated relationships in gas amplification are to be found in SAU77 and SAD80 as well as in EHL.

4.2.2 Design

The drift tubes are optimized in such a way that, on the one hand, they are made up of the fewest possible low-cost components, but, on the other hand, have high spatial resolution, even at large angles. The geometric dimensions resulted from the requirements that the number of tubes be kept small, in order to minimize costs for the electronics, and to keep the maximum drift time so small that enough time is available until the next $p\bar{p}$ beam intersection, in order to be able to undertake a rapid analysis of the drift tubes that register a particle. Only thus is it possible to build a muon trigger which is based solely on the data from the muon detectors. The optimization of the tube shape was treated in

the diploma-thesis by T. Ehlert (EHL). The construction of a fast muon trigger, as well as the first experience obtained from its operation are described in the diploma work by H. Lehmann (LEH).

The muon detector is operated, just as is the central detector of the UA1, with a gas mixture of 40% argon and 60% ethane. For this gas, above a field strength of 500 V/cm, one expects a drift velocity of 50 μm/ns, almost independent of the field strength (MAR79, see Fig. 10). At such field strengths the location-time relation is almost linear.

The anode wire is held in tension by a force of 3 N over a length of 6 m. It sags only 0.1 mm at its center, and therefore requires no other support in the tube.

Fig. 11 shows a cross section through the tube. The 7-cm-long drift spaces are located left and right of the central anode, which consists of a stainless steel wire 0.05 mm thick. A typical anode voltage is 3000 V. In order to guarantee the desired field strength of 500 V/cm everywhere, it is necessary to use cathode voltages of -7000 V. Two additional auxiliary cathodes with - 5000 V shape the field so that as few field lines as possible that come from the cathodes end on the body of the tube, which is kept at zero potential. A collimator placed 13 mm in front of the anode cuts off all the field lines that have too large a distance from the center of the sensitive volume. These field lines are not wanted because the electrons that drift along them arrive at the anode later than those that drift in the center. These outer electrons merely spread out the pulse, but do not contribute to the time definition.

Fig. 12 shows the field shape for one half of the tube. By means of the collimator the tube is divided into two regions that are simple to treat. Within the collimator a radial field exists; outside the dominant field is a largely parallel and homogeneous field in the sensitive volume

4.2.3 Properties

The properties of the tube were determined experimentally in a 10 GeV π^- beam at the 28 GeV proton synchrotron at CERN (EHL). Fig. 13 shows the geometric arrangement of the experiment. The tube was fastened to a solid aluminum frame in such a manner that it could be rotated and laterally displaced. Ahead of and behind the frame were drift chambers with a drift space of 2.5 cm and a spatial resolution of 0.1 mm were placed, in which the pion beam was defined. In addition the beam had to encounter a beam telescope made of scintillation counters, which were placed further forward. With this apparatus the following results were achieved:

1) At a working voltage of 3100 V on the anode the drift tube is efficient over the entire length of the drift space (Fig. 14).
2) In the voltage range of interest to us the pulse height doubles when the anode voltage is increased by 150 V (Fig. 15).
3) Along the drift space the pulse height is proportional to the thickness of the sensitive volume, and thus to the number of primary electron produced (Fig. 16, compare this to Fig. 12).
4) Fig. 17 shows the location-time relationship for various angles of incidence. For 0^o it is linear; at larger angles irregularities appear, but these may be explained

by the shape of the sensitive volume (see EHL, EGG80, BEC75). The deviation from linearity, even at 60^{o} is not more than 5 mm.

5) At angles up to 20^{o} the spatial resolution is between 0.25 mm and 0.4 mm. At larger angles it becomes worse; at the locations where there are irregularities in the location-time relationship it rises to as much as 2 mm (Fig. 18)

6) One can infer the location where the particle passes through the tube from the differences in the transit time of the pulse to the two ends of the tube, admittedly with considerably poorer precision (Fig. 19). The achievable spatial resolution σx amounts to about 60 mm in the region around the center of the tube and to about 130 mm at the ends of the tube.

5) Sources of Background in Muon Identification

The target luminosity of the UA1 experiment amounts to $L = 10^{30}\ cm^{-2}\ s^{-1}$. For a total cross section of 55 mbarn one would thus expect 50,000 $\bar{p}p$ interactions per second. The mean particle multiplicity had already been measured by the UA1 collaboration, and amounts to $\bar{n} = 3.6 \pm 0.3$ charged particles per unit interval of rapidity in the range $-1.3 < y < 1.3$, where y is the rapidity. The primary production consists mainly of pions and other hadrons (ARN81). Compared to this enormous hadron rate, the number of muons produced by the decays of the intermediate bosons:

$$\bar{p}p \rightarrow W^+ + X \quad , \quad \bar{p}p \rightarrow W^- + X \quad , \quad \bar{p}p \rightarrow Z^0 + X$$
$$\qquad\quad \hookrightarrow \mu^+ + \qquad\qquad \hookrightarrow \mu^- + \qquad\qquad \hookrightarrow \mu^+ + \mu^-$$

is extremely small. At an integrated luminosity of

$$\int L\, dt = 10^{33}\ cm{-}2$$

one muon is expected from the W decay (for $-2 < y < 2$) while at the same time typically 10^9 other particles were produced (EGG80a). In order to be able to find such rare events with certainty it is necessary to know all the other processes which would cause particles to be seen in the muon detector, which do not stem from W or Z decays. Such background events have various sources; the background may be divided into muonic and hadronic components:

1) They may be muons produced promptly in the $\bar{p}p$ collision via the Drell-Yan mechanism, which have enough energy to pass through all the absorbers.
2) Background muons may, however, also result from the decay of mesons, for example pion decay or kaon decay.
3) Other heavy particles can also disintegrate into muons.

Finally, particles other than muons may also reach the muon chambers and there leave a track that mimics a muon.

4) They may be pions which have made no inelastic interaction in the entire absorber, or, on the other hand,
5) they may be hadrons that have come from a hadron shower in the hadron calorimeter and have reached the muon chambers.

The most important muonic background comes from the decays of pions and kaons. For the side regions and the top region of the muon detector one can estimate the rate of disintegrations in the central detector with a radius of 1.3 m. After the disintegration the muons must also have a transverse momentum of about 1.4 GeV/c in order to be able to penetrate the calorimeters at the lateral region; for the top and floor regions the transverse momentum must be 1.5 GeV/c. The transverse momentum of the decaying pion is then on the average 20% larger (the rest of the momentum is carried off by the neutrino which has also been produced by the decay). Alper has measured how often pions with transverse momenta P_t greater than a threshold momentum P_t^{cut} are produced (ALP75). Fig. 20 shows this spectrum. If one multiplies the number of primary charged pions with the probability of production in one P_t interval, and with the mean decay probability in this interval, then one obtains the rate for the background of decay muons. The side region covers, like the top and bottom regions together, an azimuth angle of $\Delta \phi = \pi$, and a rapidity interval of $-1 < y < 1$. Table 2 lists the rate of this background for individual P_t intervals. The result is a rate of 13.2 muons per second in the lateral region, and 8.4 muons per second in the top and bottom regions at a luminosity of $L = 10^{30}\ cm^{-2}\ s^{-1}$.

Directly produced muons and those from the decay of heavy mesons will not be treated here.

They constitute an additional uncertainty in the background estimation. The determination of the hadronic background forms the subject of the next chapter.

6) Measurement of the Background Due to Hadrons that are Mistaken for Muons in Muon Identification

6.1) Logic and Design of the Experiment

By hadronic background we mean all particles that leave the calorimeter after the incomplete absorption of a hadron, which may look like a muon. These may be hadrons that have not undergone an inelastic collision in the absorber, or they may be particles that were produced by the hadron cascade, leave the calorimeter, and have a direction similar to that of the entering pion. This background is called "punch-through". It is very difficult to calculate the punch-through for so complicated an absorber shape as is given in the UA1 experiment. Furthermore, the punch-through is affected by a very large number of parameters, which in turn are energy- and material-dependent. Especially in the end part of a shower, which is important for these considerations, the statistical fluctuations in such quantities as range, type of particles last produced, average momentum, etc. are large, which makes the theoretical calculations considerably more difficult.

We therefore reached the decision to determine the punch-through rate experimentally. For this purpose an experiment was constructed using prototypes and original parts of the UA1 detector. With this apparatus it was possible to measure not only the absolute punch-through rate, but also the signatures of the different types of events in the individual components of the detector. Particular emphasis was put on a good description of the event topology in the muon detector. A more detailed examination was made of

the possibility of detecting individual events as background without losing too many muon candidates in the process. A π^- beam was selected for simulating the UA1 conditions and for measuring the punch-through. Such a beam has the disadvantage that it is contaminated with muons from pion decay. Although it is possible to recognize muons on the basis of their range, this identification does pose difficulties, especialy at low energies. We therefore chose a momentum range from 2 GeV/c to 10 GeV/c, in order to be able to extrapolate from the conditions at high momenta, where the muon is easy to identify, to the rates at low pion momenta. The experiments were carried out at experimental position D31A of the 28 GeV proton synchrotron at the European Nuclear Research Center CERN. During a slow ejection of 0.3 s protons are projected against a metal target. The secondary particles produced there are momentum-selected by a strong magnetic field and a beam collimator, and are guided to the area of the experiment by a transport system consisting of deflection and focussing magnets. By a suitable selection of the magnet current amplitudes and of the collimator apertures it is possible to produce pion beams of known momenta between 2 GeV/c and 10 GeV/c.

The hadrons produced by $p\bar{p}$ interactions have a mean transverse momentum of 400 MeV/c. As may be seen from Fig. 20, the momentum spectrum decreases very rapidly as the transverse momentum increases. For this reason the largest background due to mis-identified particles in the UA1 experiment is expected to be between 2 GeV/c and 3 GeV/c, barely above the minimum momentum that a particle needs to be able to pass through the calorimeters completely (p_{min} = 1.5 to 2 GeV/c).

6.2) The Experimental Set-Up

Figs. 21 and 22 show two views of the experimental set-up.

The incident particle is defined in a beam telescope that consists of the scintillation counters S0 - S3 and B. S0 - S3 are 110 x 110 m^2 in size, S4 is 40 x 40 mm^2 in size, and B is a ring-shaped counter with 300 mm outer diameter and 70 mm inner diameter. The S counters are connected in coincidence logic, while the B counter is in anti-coincidence with them. This suppresses events that are accompanied by associated particles. Since the beam is focused by quadrupole magnets it has a spatial divergence that increases with decreading momentum. The B counter makes sure that only the inner part of the beam, the part that is parallel to the beam axis, is used for the trigger.

A so-called "gondola" from the UA1 experiment was used as electromagnetic calorimeter; the structure of this "gondola" has already been described above (Chapter 3). The incoming particle is incident on it near one end, so that the signals in the light pipes are attenuated as little as possible before they reach the photomultipliers. The hadron calorimeter consists of a prototype with the same structure as a UA1-C module with a front surface of 99 x 92 cm^2. 45 cm behind this iron calorimeter there stood a 2 x 2 m^2 prototype of the muon chambers which had exactly the same structure as the final chambers. 22 cm further back stood a 20-cm-thick iron wall and 14 cm further behind that another 40 cm of iron. Together with the calorimeters placed in front of it, this iron is used for muon identification. For simulating

still greater absorber thicknesses, such as those that occur in the forward direction of the UA1 experiment, it is possible to insert additional hadron calorimeters into the beam. Since we had no additional electromagnetic calorimeters available, we placed a 2.5 cm-thick lead plate in front of the gondola to bring the system even with each additional hadron calorimeter. The most important data concerning the detectors used are to be found in Table 3.

Muons that stem from pion decay in the last part of the beam are identified in scintillation detectors M1 and M2, which have areas of 1.1 x 1.1 m^2, and which are placed behind the last iron walls. Using trigger counters T1 and T2 it is possible to trigger on all events in which at least one particle has left the calorimeters towards the back direction. T1 consists of a coincidence of two counters with an area of 47 x 47 cm^2. T2 consists of three horizontal and three vertical counters which are read out individually and are switched in coincidence. T2 covers an area of 1 x 1 m^2. T1 is located 5 cm behind the iron calorimeter and thus includes larger exit angles than does T2, which is placed 10 cm behind the muon chamber.

6.3) The Trigger

The simplest trigger triggers the detector read-out whenever an incident particle is observed in the beam telescope. This minimal trigger will be designated as S in what follows:

$$S = S0 \times S1 \times S2 \times S3 \times S4 \times \overline{B}$$

(B suppresses halo particles that fly along with the beam particle.) Muons are triggered for if one additionally

requires a coincidence from M1 and M2, since, in contrast to the hadrons, the muons are capable of penetrating clear through the additional 60 cm of iron behind the calorimeters. For mean momenta less than 4 GeV/c M2 is taken out of the coincidence circuit since not all the muons will have enough energy to get as far as M2.

The muon trigger is designated as M:

$M = S \times (M1 \times M2)$ for $P \geq 4$ GeV/c

$M = S \times M1$ for $P < 4$ GeV/c

The decay length for pions amounts to 22 m from the last deflection magnet to the calorimeter. Fig. 23 shows the expected and measured muon rates from pion decay. The difference between the measured and expected rates has a number of causes:

First of all, not all muons are detected by the beam telescope. In pion decay the muons are emitted into an angle θ_μ relative to the flight path of the pion. Different angles will occur for different muon momenta. Muons that are emitted in the forward direction in the center-of-mass system carry approximately the momentum of the decaying pion. Muons emitted in the backward direction carry about half the pion momentum. The correlation between the muon momentum and the angle of emission θ_μ is shown for three pion momenta in Fig. 24. For a given acceptance angle of the telescope the fraction of detected muons is dependent on the muon momentum. Whereas for large pion momenta nearly all the muons are seen, the situation for small momenta is such that only those muons coming from pions emitted forward or backwards fall within the acceptance cone of the telescope. Additional muons are lost because at small pion momenta the muons emitted backwards no longer have enough energy to get as far as M2. In

addition, the muons are deflected on their path through the iron due to Coulomb scattering. The amount of deflection increases as the momentum becomes smaller, so that for beam momenta more and more muons fall outside the spatial acceptance of the muon counters M1 ans M2, and thus are lost to the trigger. [Translator's note: The sentence above is translated as given in the manuscript. It appears however that a word is probably missing. It would seem that the sentence should read ... so that for (decreasing) beam momenta...]

In addition the muon trigger becomes contaminated at high energy due to punch-through events in which shower particles have gone as far as the counter M2. The points on Fig. 23 have been corrected for these perturbations using the values from Chapter 7.

For us the most important trigger is the anti-muon trigger AM for which at least one particle has left the calorimeter in the rearward direction, but where the muon counters have not registered. This means that one of the trigger counters T1 or T2 has registered, without at the same time both muon counters having seen a particle. Below 4 GeV/c M2 has again been taken out of the trigger here:

$$AM = S \times (T1 + T2) \times \overline{(M1 \times M2)} \qquad \text{for } P \geq 4 \text{ GeV/c}$$

$$AM = S \times (T1 + T2) \times \overline{M1} \qquad \text{for } P < E \text{ GeV/c}$$

This trigger is used to determine the rate of hadronic punch-through. Unfortunately at low momenta the AM trigger is contaminated by muons which were, indeed, accepted by the beam telescope, but which do not have enough energy to get as far as to M2. If one assumes that these muons, which were emitted backwards in the pion decay, carry about 60% of the

pion momentum, then one would expect a muon contamination of the anti-muon trigger for the various absorber thicknesses at beam momenta which are smaller than the following momenta:

D1 (Gondola, C module) : 2.9 GeV/c
D2 (Gondola, C module, 1 addl. calorim.) : 4.5 GeV/c
D3 (Gondola, C module, 2 addl. Calorims.) : 5.1 GeV/c

These numbers were calculated using range tables (JOS69) and Table 4. For thicknesses D2 and D3 the range to counter M2 was used to determine the limiting momentum. For thickness D1 the calculation was extended only to counter M1, since the start of contamination lies below 3 GeV/c. For these momenta M2 had been taken out of the trigger.

6.4 Data Acquisition

The electromagnetic calorimeter is subdivided into four compartments with different thicknesses. These compartments are 3.25, 6.5, 9.75, and again 6.5 radiation lengths thick, and are observed at each end of the gondola by photo-multipliers, which are each connected to two different amplifiers. The hadron calorimeter consists of a front and a rear part, which are both of the same thickness, and each of which is read out by two photo-multipliers. The additional calorimeters are also connected to two phototubes each. All calorimeter signals are individually passed onto 8-bit analog-to-digital converters.

A total of 26 different individual count rates or combined rates are collected in a dead-time-free manner. In addition it is determined for each event which of the scintillators has registered. The muon chambers are recorded using drift-time recorders (DTR) with a time resolution of

4 ns. This system has the advantage, as compared to simple time-digital converters (TDC), that more pulses can be recorded in the individual channels. For each channel (each drift tube) a push register (FIFO) is available, into which hits are read in continuously. If an event is to be recorded, then after the maximum drift time of 1.5 μs a stop pulse is given and the state of the push registers is frozen. After being read out by the computer the inputs to the push registers are reopened.

A block circuit diagram of the electronics of the experiment is shown in Fig. 25. During the ejection the proton synchrotron delivers a signal which is 0.5 s long, the so-called spill gate. Only during the spill are events with the triggers described above accepted. Since the master signal thus created consists of an overlap coincidence with many inputs, the event time T_o is defined afterwards by means of the signal from a beam telescope counter (retiming). This signal sets a flip-flop which in turn controls the input buffer for the ADCs and counters and generates the stop signal for the DTRs. After a 100 μs delay, which is required for digitalization, the computer read-out of the event is initialized. Once the HP 2100 computer has processed the event the flip-flop is reset, and the detector is ready for the next event. In order to check the zero-points of the ADCs it is possible to produce additional master signals, outside the spill (pedestal measurement).

The DTRs, ADCs, and counters are read out via a data bus and a standard CAMAC interface by an HP2100 computer, and written out onto magnetic tape (Fig. 26). It is possible to produce simple histograms and graphic representations of events on-line (Fig. 27). A branching unit (Spy) is built

into the data bus, which is controlled by a CAVIAR computer. With this device it is possible to copy out results from the data stream asynchronously to the HP computer. This makes it possible to make random-sample error searches in the electronics and the read-outs. Fig. 28 shows an image from this control monitor. Measurements for the following beam momenta were carried out for three different absorber thicknesses each: 2, 3, 4, 5, 8, and 10 GeV/c. For each momentum three sets of data were obtained with the minimal trigger, with 30,000 events in each, one data set with muon trigger with 10,000 events, and one data set with anti-muon trigger with as many events as possible, nut a maximum of 20,000 events. With the minimal trigger as many as 300 events per second could be recorded. The rate of incident particles (S) amounted to 300/spill at small momenta, and as much as 15,000/spill at a beam momentum of 10 GeV/c.

7) Results of the Measurements in the Test Beam

7.1) The Measured Exit Probability for Hadrons

The hadronic punch-through is measured by determining the exit probability for hadrons from the calorimeters. For this purpose the rate of anti-muon triggers AM is divided by the number of incident particles, defined as S. The probability W_h, per incident particle, then becomes:

$$W_h = AM / S$$

This W_h, that is to say, the acceptance of the anti-muon trigger, is plotted as function of the beam momentum in Fig. 29. For momenta smaller than 4 GeV/c M2 is removed from the trigger. Since in the AM trigger it is required that at least one of the trigger counters T1 or T2 has registered, it is possible to subdivide W_h further, by using the AM trigger only with counter T1 ahead of the muon chamber for one case, and for the other cases uses only trigger T2 behind the chamber. Thus one obtains two probabilities W_hT1 and W_hT2, which give the probabilities for punch-through directly behind the calorimeters, and for punch-through as far as behind the muon chambers.

$$W_hT1 = S \times T1 \times \overline{(M1 \times M2)}, \qquad W_hT2 = S \times T2 \times \overline{(M1 \times M2)}$$

These are plotted as function of beam momentum in Fig. 30. On the average W_hT1 is 1.5 times as large as W_hT2, since T1 is located directly behind the calorimeters, and thus sees a considerably larger solid angle, as seen from the calorimeter, than does T2. In Fig. 30 initially only those beam energies were used for which the data are not contaminated by muons (for D1, 3 to 10 GeV, for D2, 5 to 10 GeV, for D3, 8 to 10 GeV).

For small momenta the rate is in error; in Fig. 29 one finds that there the rates lie systematically too high. There the AM trigger also includes muons that did not get as far as M2. However, in determining $W_h T1$ and $W_h T2$ it is possible to gain two additional points (for D2 at 4 Gev/c and for D3 at 5 GeV/c) if one includes the measured rates of muon counter M1.

With a pure anti-muon trigger not contaminated by muons it is possible to determine how strongly a hadron shower is damped by the 20 cm of iron that lie between the counters T2 and M1. To this end one divides the partial number of AM events for which the M1 counter has registered, by the total number of all events. Of course one may only take into consideration those events in which T2 has registered. T1 is no longer taken into consideration, since the solid angles covered by T1 and T2 are too different, whereas T2 and M1 cover similar angles. For a measure of the shower damping, d, that is, the decrease of the particle density in the end of the shower, one may define:

$$d = [S \times T2 \times M1 \times \overline{M2}]/[S \times T2 \times \overline{(M1 \times M2)}]$$
$$= \exp\{(-20\ \text{cm})/L_d\}$$

Here L_d is the damping length for a hadron shower in iron. The damping of the shower at the end may also be determined in another way: By inserting the additional calorimeters it is possible to increase the absorber thickness. By dividing the anti-muon trigger rates by the various absorber thicknesses one again obtains d, although, in thais case, for an equivalent iron thickness of 24.3 cm:

$$d = \{[S \times T2 \times \overline{(M1 \times M2)}] \quad \text{for D2 (or D3)}\}/$$
$$\{[S \times T2 \times \overline{(M1 \times M2)}] \quad \text{for D1 (or D2)}\}$$
$$= \exp\{-(24\ \text{cm})/L_d\}$$

Both methods result in approximately the same damping lengths. They are plotted in Fig. 31.

To correct the points at 4 GeV/c and 5 GeV/c, all the numbers which follow refer to the shower damping in the 20 cm of iron between T2 and M1. A correction can be carried out by making the following assumptions:

1) The damping length for hadron showers amounts to 22.5 cm (d_h = 0.41 in 20 cm of iron).
2) The measured rate S x T2 x $\overline{(M1 \times M2)}$ is composed of a mixture of particles containing both hadrons and muons which enter into the rate with respective weights of R_h and R_μ ($R_h + R_\mu = 1$).
3) All muons succeed in reaching at least counter M1, in other words, are not lost ($d_\mu = 1$).

With these assumptions it is possible to calculate the true hadron rate at both points. If d is determined there from the rates, the results are d = 0.74 and 0.79, respectively, which are much higher values than would be expected for pure hadron events. This increase is caused by muons which, although they manage to just reach M1, do not make it to M2, and thus contaminate the trigger. A pure muon beam that reaches M1 but not M2 would produce a value of D = 1, while a decaying hadron shower produces d = 0.41. In other words, at both the points in Fig. 30 at which corrections are to be made, d is composed of $d_\mu = 1$ and $d_h = 0.41$. If one weights d_μ with the relative muon fraction, the muon contamination, and weights d_h with the hadron component in the data sample and adds these weighted components, the measured value of d must result.

$$d = d_\mu R_\mu + d_h R_h$$

where $R_\mu + R_h = 1$, $d_\mu = 1$, and $d_h = 0.41$. From these values one may then determine the hadron fraction in the total data sample for these points:

$$R_h = (1 - d)/(1 - d_h)$$

By multiplying R_h by the measured anti-muon rate

$$S \times T2 \times \overline{(M1 \times M2)}$$

one finds the true hadronic punch-through rate for the points in question. It is plotted in Fig. 30 with larger symbols. W_hT2, the punch-through probability to a location behind the muon chambers is parameterized to be:

$$W_hT2 = \alpha\ (1.07 \pm 0.12) \times 10^{-3} \times P_\pi^{(1.62 \pm 0.04)}$$

(P_π is in GeV/c, $\alpha(D1) = 1$, $\alpha(D2) = 1/3$, $\alpha(d3) = 1/9$)

where α is a measure of the damping achieved by the insertion of additional calorimeters equivalent to 24.3 cm of iron, a factor of 1/3 per added calorimeter.

The same adjustment may also be used for W_hT1, if W_hT2 is multiplied by 1.5. At the measured points the relative errors are about 1% and are of statistical nature. The punch-through correction up to M2 changes the points by at most an amount that lies within the size of the plotted symbols.

From this measurement it is possible to calculate the expected background rate for punch-through in the UA1 experiment. The values will be found for the individual P_t intervals in Table 5.

7.2) The Energy Deposited in the Calorimeters in Punch-Through Events

Muons and hadrons differ in the amounts of energy they deposit in the calorimeters. We are interested in this deposited energy for two reasons: First, with this information it is possible to calculate the free energy behind the calorimeters, which enters the muon chamber in the case of punch-through events. Secondly, with this information it is possible to state at what energies punch-through events may be suppressed by an energy cut. This would be possible only if the energy spectrum of the punch-through is distinctly different from the muon spectrum.

For the energy measurement each of the calorimeter sections were first calibrated using muons. Since it is known how much energy a high-energy muon deposits in one section, one obtains an unambiguous energy scale by comparing the measured signals from the ADC channels with the expected amount of energy. For each event all the calorimeter signals are then weighted by their energy scale and added together to make E_{tot}, the total energy. Since all the calorimeter signals are added together, E_{tot} will be larger for greater absorber thicknesses than for small thicknesses. Figs. 32, 33, and 34 show the energy spectra for muons and punch-through events. Fig. 32 shows the muon spectrum and the reference spectrum used for calibration. Fig. 33 shows the punch-through spectrum for the same beam momentum. It is distinctly different from the muon signal. In the left part of the spectrum one sees a peak which is due to pions that have not undergone a strong interaction in any of the calorimeter sections, in other words, which have deposited only the

energy from a minimally-ionizing particle. The number of non-interacting particles may be estimated from the distribution, it depends on the cut-value in the distribution. This, in turn, allows the calculation of the interaction length in iron, since the absorber thickness is known. the interaction length determined from the punch-through spectra turns out to be between 18.5 and 21 cm, depending on the energy cut. This length is consistent with values given in the literature.

In Fig. 35 E_{tot} is plotted for the three absorber thicknesses. If the entire beam energy were deposited these points would lie on a straight line. They deviate from a straight line, since a part of the energy leaves the calorimeters towards the rear (it was, to be sure, just such events for which we triggered). The dashed lines show the energy which a particle at minimum ionization would leave behind. At the large momenta only about 50% of the beam energy was deposited, the rest of the energy reaches the muon chambers. At low energies the amount of energy deposited is practically no longer distinguishable from that deposited by a particle at minimum ionization (see also Fig. 34). For us this means that exactly at those energies of interest for us we can not reduce the background due to punch-through by means of a cut in E_{tot}; in other words, we must search for ways of reducing the background within the muon chamber itself.

7.3) Appearance of the Events in the Muon Chamber

In the muon chamber we expect different signatures for muon and punch-through events. In the case of 100-percent detection probability muons yield exactly one track in both

projections. Aside from the hits produced by muons, however, one also expects hits from δ-electrons along the muon track. In contrast, hadronic punch-through yields a totally different signature. Depending on the trigger, one sees here the end of a hadron shower in the chamber. The principal result is a larger number of particles. These particles have lower energies than the incident pion, since a part of the shower energy has already been used up in the calorimeters, and the remaining energy is distributed over a number of particles. The particles that still remain may stop in the chamber, undergo an interaction in the chamber, or be scattered out of the chamber. In the latter case they have a large Coulomb scattering angle because of their low momenta. In order to understand the different signatures better we set up a track-identification and track-reconstruction program (MUO81).

This program recognizes tracks in the two orthogonal projections of the muon chamber. A track is considered to be identified when at least three points from the four individual planes of a given projection can be combined to a single straight line. This limitation to three hits is necessary since between the drift tubes of a given plane there are dead-spaces of 1 cm width, which are due to the method of construction, and the tubes themselves are not 100 percent efficient. Finding the track points is achieved as follows:

First the raw drift times are transformed into space coordinates using the linear relationship

$$X = V_D \, T_{Drift} \quad \text{with } V_D = 52 \ \mu m/ns.$$

Within one double plane all the points from the one plane are combined with all the points of the next plane, and straight lines calculated from these. All straight lines that form an angle of more than 60^o with the main incidence direction are

discarded, along with the coordinate points that generated them. The remaining two-hit straight lines are then corrected. Since the place-vs-time relationship of our drift tubes is not linear at large angles, angle corrections are carried out using the straight-line slopes that were found. and the raw drift times are corrected as to the angle of incidence.[1)] The slope of the straight line is then recalculated from the new coordinates. This procedure is repeated for the other double plane.

Then a check is made as to whether there are two straight-line segments in the two double planes whose slopes are similar, and that point to each other. Four such points are then combined into one four-hit track. The remaining straight-line candidates are tested to determine whether in the other double plane for each instance a hit is found within a band 1 cm wide about the extrapolated position. If that is the case, then these hits are fitted together to form a three-hit track. The same procedure is repeated in the other projection. Only when in both projections exactly one track is found is it possible to continue with making a reconstruction in space.

The efficiency of the program can be measured with a muon trigger at a beam momentum of 3 GeV/c and absorber thickness D1, since for this case it is still possible to make a muon identification, and the punch-through to the muon counters is minimal. In 0.9% of all triggers the program finds no track in either projection, in 97% of all triggers it finds a track in at least one projection, and in 82% it

---

1) Fig. 36 shows the drift tube calibration that was used.

finds exactly one track in each of the two projections. 2% of all events have more than one track in one of the projections. At 10 GeV/c 2.2% of all muon triggers show no track. Since the angle of incidence into the chamber is 90^{o}, and the Coulomb scattering angle becomes small at high momenta, more tracks now pass through the two dead spaces. This causes two-hit tracks, which are discarded by the program.

After the events have passed the track program they can be displayed graphically. Figures 37 through 40 show some event types.

Fig. 37 shows the signature of a muon at a beam momentum of 10 GeV/c. In each drift tube that has registered a pulse one initially sees two points, since the right-left ambiguity has not yet been resolved. The track calculated from this is also plotted. In each projection all four planes have registered. In Fig. 38 one sees a punch-through event at 10 GeV/c beam momentum. One particle has left the calorimeter rearward, and passes through the muon chambers with low momentum, and therefore large scattering angle. Fig. 39 shows a punch-through event with high track multiplicity and many hits, as well as large scattering angles (P_{π} = 10 GeV/c). The event in Fig. 40 also has high hit multiplicity; however only one track is found, which in addition exhibits a large angle. One sees very well how the hit multiplicity decreases towards the rear in the chamber. Evidently a very large number of low-energy particles are produced that remain stuck in the chamber, or are scattered out of it. Here also the momentum of the incident pion was 10 GeV/c.

7.4) The Behavior of the Chamber

Using the track program it is immediately possible to determine the efficiency of the muon chamber. For this purpose one extrapolates a track via three hits in three planes into the fourth plane, the one to be tested, and there checks to see whether the track has caused a hit or not. The efficiency may then be defined

η = (Number of tracks with a hit in the test plane)/
(Total number of test tracks)

Fig. 41 shows η for the third plane of the Z projection as function of the spatial location in the plane. The muon trigger at 3 GeV/c was chosen to be the event trigger. With this trigger the chamber is illuminated best. The measured points reproduce the arrangement of the drift tubes. Every 15 cm the degree of efficiency drops when the test track points to a dead space or in its vicinity, otherwise η lies al close to 100%. The errors shown are of statistical nature. The other planes exhibit the same behavior.

The smallest distance between two points that can just be resolved by the electronics used amounts to 2.5 mm; this corresponds to 50 ns as the smallest drift time difference. After this amount of time has elapsed the electronics is ready again to record additional pulses. It is now possible to use the track program to investigate whether the tube post-pulses electronically, or whether additional pulses are caused by additional particles such as δ-electrons. The time differences Δ t between a hit at time t_o, which is associated with a track, and all other hits measured in the same tube are measured and plotted. If the tube post-pulses, then the distribution of time differences on the positive side would be distinctly different from that on the negative

side. However the measured distribution (Fig. 42) exhibits good symmetry; this means that the tube does not post-pulse, and the additional hits may be taken to be real. The hole in the center of the distribution stems from the electronically caused dead-time of 50 ns.

From the time difference distribution it is also possible to conclude that the probability of producing an additional pulse is the same everywhere in the tube. In this connection, consider, for example, the right side of the distribution (see Fig. 43 here, with larger statistics). After a hit has occurred the differential probability dW_{2P}, of finding an additional pulse after time t in the time interval dt, decreases proportionately with the probability $W_{2P}(t)$:

$$dW_{2p}(t) = -c\, W_{2p}(t) \quad \text{(c: proportionality factor)}$$

where $W_{2P}(t)$ is the probability that another pulse has already been found up to time t. (It should be noted that t is always measured only from one hit to its nearest neighbor.) If $dW_{2P}(t)$ is integrated with respect to dt one finds

$$W_{2P}(t) = \exp\{-ct\}$$

If one plots the count rates for double pulses in the time interval Δt instead of the probability $W_{2P}(t)$, then one expects the same exponential fall-off. It will be seen from Fig. 43 that to first approximation the count-rate does decrease exponentially towards larger Δ t; hence the probability of finding additional pulses in the tube is nearly constant over the entire drift time.

We shall now describe how the chamber reacts to the various types of events. To begin with, we shall present the mean hit multiplicity <nHit> for the four double planes. For

a 10 GeV/c muon trigger, with an absorber thickness D3, in other words,. at the lowest possible hadron contamination, one finds an average multiplicity of 2.8 hits per double plane; however, in the last plane it amounts to only 2.3, since one drift tube was defective in this plane. With an anti-muon trigger or a hadron trigger the values lie higher. They are plotted in Fig. 44 for the absorber thicknesses against the beam momentum. The figure also shows up to which multiplicity 90% of all events are represented (this limit is shown by the ends of the "flags" that extend from the mean multiplicities). Whereas the mean hit multiplicities increase only slowly with the beam momentum, the 90% limit increases more steeply. The muon contamination for small momenta is clearly to be seen. Here the values lie close to those expected for muons. For the large thickness D3 one also sees that for very low momenta not all the particles reach the end of the chamber any more, because they have been stopped or scattered before then. For clear hadron events, in other words, large momenta, both the mean multiplicity and also the 90% limit decrease by a factor of 0.5 to 0.8 from the first to the last double plane.

The track multiplicities do not exhibit such a clear picture. In Fig. 45 the mean number of tracks found in both the projections is plotted against beam momentum. The Y-projection (o), which is the first to be impacted by the beam, sees just a few more tracks than does the Z-projection (□). The steep fall-off at thickness D3 and towards smaller momenta is clearly visible.

8) Reduction of Punch-Through Background in Muon Identification

In this chapter we shall examine how well the annoying background due to punch-through can be reduced. The calorimeters are of help here only at high momenta where the punch-through energy spectrum is distinctly different from the muon energy spectrum. At low energies, typically less that 5 GeV it is not possible to reduce the background by means of a cut in the energy spectrum, because just in these events a large part of the energy of the incident pions is not released until after passage through the calorimeter. For this reason they also record only small amounts of deposited energy. Exactly at those low pion energies that are so interesting for us, the calorimeters fail completely as an aid to background reduction. The energy spectrum can then no longer be distinguished from that of a minimum-ionization spectrum. Thus it is only in the muon chamber itself that we can hope to find possibilities for reducing the background.

In principle only those events get in the way for which exactly one track is seen in the chamber; specifically, a track which can be mistaken for a muon track. As the multiplicity distributions show, it is precisely at small energies that there preferably occur slow particles which stop in the chamber or leave through its sides. While we expect the largest punch-through background in the UA1 experiment at small energies, nevertheless, these events should be the ones easiest to suppress. It is more difficult to reduce the hadron background with one or more tracks in the chamber. Nevertheless, such a reduction is also possible.

While a 40 GeV/c muon stemming from the decay of a Z-boson is deflected by about 3 milli-radians as it makes its way through the calorimeters, a muon or a non-interacting pion with a momentum of 1.5 GeV undergoes a Coulomb scattering of 90 milli-radians. The slower reaction products that are created in a hadron shower are scattered even more strongly. One must therefore divide the angular distributions of the tracks reconstructed in the muon chamber in order to separate the interfering, slow particles from the fast ones. However, one must not lose too many high-energy particles at the same time. Most effective is a cut in the straight line slope G, which is defined as follows:

Let G_{yi} and G_{zj} be the slopes of the reconstructed straight lines in the two projections, respectively, then we shall seek out the smallest slope in each projection. G is then set equal to the larger one of these two slopes:

$$G = \text{Max } (\text{Min}(G_{yi}), \text{Min}(G_{zj})).$$

Thus this definition demands that exactly one track has been found in each of the two projections. A suitable cut in G does not reject many of the high-energy muons, since for these events exactly one track is practically always produced in each projection, which additionally also remains within the angle cut-off. On the other hand, hadrons with large scattering angles are strongly suppressed. If a high-energy muon is accompanied by slow hadrons, the event will pass despite the cut, since the muon will then exhibit the smallest angle in both of the projections.

Fig. 46 shows the reduction factor F_{red} by which the punch-through events produced with the anti-muon trigger can be suppressed by a cut in G. The largest beam momentum we had available was 10 GeV/c. The value of the cut was then

selected in such a way that 90% of the muons at 10 GeV/c fall within the angle cut. For D1 the cut angle is 45 milli-radians, for D2 it is 50 milli-radians, and for D3 it is 55 milli-radians. One sees that the angle cut reduces the punch-through by a factor of 20 at the large beam momenta, and a factor of 50 for the small momenta. The relative errors in the measured data are statistical and lie at about 10 to 20%. It should also be noted that F_{red} was determined from the data set obtained with the anti-muon trigger. For small momenta the trigger is strongly contaminated by muons, so that in practical terms, what was measured here was the reduction of low-energy muons. Thus the reduction factor F_{red} here at best yields an upper limit. For a data set not contaminated with muons, at small momenta, F_{red} would surely be expected to be smaller; thus pure hadron events are more strongly suppressed by the angle cut in G at small momenta.

9) Summary

A 2 x 2 m^2-sized prototype of the muon detector for the UA1 experiment at the pp storage ring of the European Nuclear Research Center CERN was tested in a negative pion beam with 10 GeV/c momentum. The muon detector consists of drift tubes with an optimized, simple electric field configuration. The spatial resolution of the drift tubes lies between 0.2 and 0.3 mm for perpendicular particle incidence, and decreases up to 1 mm for an incidence angle of 60°. Non-linearities in the location-time relation are explainable from the shape of the electric field.

The hadronic punch-through was studied in connection with the calorimeters of the UA1 experiment. This punch-through forms a strong source of background in muon identification. In the momentum range from 2 GeV/c to 10 GeV/c and an equivalent calorimeter thickness of 102 cm of iron the probability for hadronic punch-through W_h is described by

$$W_h = (1.62 \pm 0.012) \times 10^{-3} \times P_{\pi}^{(1.62 \pm 0.04)}$$

with P_{π} in units of GeV/c. W_h is taken with respect to an incident pion. By inserting additional calorimeters, each equivalent to 24.3 cm of iron, the punch-through is reduced by a factor of 1/3. Only at high particle momenta above 5 GeV/c does the information from the calorimeters make punch-through suppression possible. At lower momenta in the range of 2 to 3 GeV/c an angle cut for the tracks in the muon detector as reconstructed in two projections is very effective. This suppresses the punch-through by a factor of 20 to

50, without losing more than 5% of the muons with a momentum greater than 10 GeV/c.

Acknowledgments

I thank Prof. Dr. H. Faissner for the opportunity of preparing this work at his institute. He also made possible my interesting stay at CERN.

I thank Privatdozent Dr. K. Eggert for his guidance in constructing the experiments and discussions on their analysis.

I sincerely thank Mrs. (Dr.) T. Hansl-Kozanecki and Dr. R. Haidan for their fruitful cooperation with me, for their constant helpfulness, and many suggestions.

Dr. H. Reithler guided me at the beginning of this work. Many thanks for this.

For help in data gathering I thank P. Erhard, K. L. Giboni, D.J. Holthuizen, E. Radermacher, and E. Tscheslog.

I owe great thanks to the entire UA1 collaboration under the leadership of Prof. C. Rubbia for support in doing the experiments.

The mechanical and electrical shops built the prototype. I thank them very much, and especially H. Frohn, J. Grooten, K. Hermens, and W. Reuter.

Last but not least I thank T. Ehlert and H. Lehmann for the discussions in the course of the written work.

Index of References

ALP75 B. Alper et al., Nucl. Phys. B100 (1975) 237

ARN81 G. Arnison et al., Phys.Lett. 107B (1981) 320

BAT70 G. Bathow et al., Nucl. Phys. B20 (1970) 592

BEC75 U. Becker et al., Nucl. Instr.Meth. 128 (1975) 593

BOC80 R.K. Bock et el., Nucl. Instr.Meth. 186 (1980) 533

EGG80 K. Eggert et al., Nucl. Instr.Meth. 176 (1980) 217

EGG80a K. Eggert, T.Hansl, CERN $p\bar{p}$ UA1 TN 80/69

EHL T. Ehlert, Diploma Thesis, Aachen (In progress)

FAB80 C.W. Fabian, H.G. Fischer, CERN-EP-80-27

FLO78 T. Flottmann, Diploma Thesis, Heidelberg 1978

GRA75 A. Grant, Nucl. Instr. Meth. 131 (1975) 167

GSW a) F.J. Hasert et al., Phys.Letters 46B (1973) 121

b) H. Faissner, Internal Report, PITHA 79-16 (1979)

c) J. Ellis, Proc. of Neutrino 79, Bergen 1979, Hrsg. A. Haatuft, C. Jarlskog, S. 451

d) J. Sakurai, Proc. Top. Conference on Neutrino Physics and Accelerators, Oxford 1978, Hrsg. A. G. Michette und P.B. Renton (Rutherford, Chilton, Didcot 1978)S. 338

e) L.M. Sehgal, Conf. Proc. Neutrino 78, Purdue, Hrsg. E.C. Fowler, (West Lafayette) S. 253

HOL78 M. Holder, Nucl. Instr. Meth. 151 (1978) 569

IWA79 S. Iwata, Nagoya Univers. Report, DPNU-3-79

JOS69 P.M. Joseph, Nucl. Instr. Meth. 75 (1969) 13

KIM81 J.E. Kim et al., Rev. of Mod. Phys. 53 (1981) No2,211

LEH H. Lehmann, Diploma Thesis, Aachen, in progress

MAR79 B. Jean Marie, Nucl. Instr. Meth. 159 (1979) 213

MU081 Public File, CERN IBM, VZ.PUB.PAM.MU0600

ROS41 B. Rossi, K. Greisen, Rev. Mod. Phys 13 (1941) 240

ROS52 B. Rossi, "High Energy Particles", Prentice Hall, 1952

RUB76 C. Rubbia et al., Proc. Int. Neutrino Conference, Aachen, 1976, Hrsg. H. Faissner, H. Reithler, P. Zerwas, Vieweg, Braunschweig 1977 S.683

SAD80 B. Sadoulet, CERN-EP/80-138

SAU77 F. Sauli, CERN 77-09

UA1 a) Aachen-Annecy(LAPP)-Birmingham-CERN-London(Queen Mary College)-Paris(Collège de France)-Riverside-Rutherford-Saclay(CEN)-Wien Kollaboration, Proposal CERN/SPSC/78-06/P92 (1978)
b) M. Baranco Luque et al., Nucl. Inst. Meth. 176(1980)175
c) M. Calvetti et al., Nucl. Instr. Meth. 176(1980)255
d) A. Astbury, Phys. Scripta 23 (1981) 397
e) P.I.P. Kalmus CERN EP/82-58

WEI67 S. Weinberg, Phys. Rev. Lett. 19 (1967) 1264
Phys. Rev. Lett. 27 (1971) 1688
Phys. Rev. D5 (1972) 1412, 1962

Chamber Type	Length (m)	Width (m)	Number of Short Tubes	Number of Long Tubes	Number of Tubes in the Individual Layers	Total Number of Chambers
A	5.55	3.75	73	49	25, 24, 36, 37	28
B	5.55	3.15	73	41	21, 20, 36, 37	12
Bottom, Large	5.55	3.60	0	74	24, 23, 23, 24	2
Bottom, Small	5.55	1.05	0	26	7, 6, 6, 7	8

Table 1

σ_{tot} = 50 mb, L = 10^{30} cm^{-2} s^{-1}, Multiplicity = 3.5

-> 175,000 particles/s

Table 2

[In the columns of numbers, commas should be read as decimal points]

Transverse Momentum Interval ΔP_t (GeV/c)	Decay Probability (%)	Pion Rate per P_t interval (s^{-1})	Muon Rate per P_t interval (s^{-1})
1,62 - 1,74	1,36	700	4,76
1,74 - 2,00	1,23	700	4,31 (Additional Intervalval for Side Region)
2,00 - 2,33	1,06	420	2,22
2,33 - 2,66	0,92	246	1,13
2,66 - 3,00	0,81	98	0,40
3,00 - 3,33	0,73	42	0,15
3,33 - 3,66	0,66	32	0,10
3,66 - 4,00	0,60	16	0,05
4,00 - 4,33	0,55	8	0,02
4,33 - 4,66	0,51	6	0,01
4, - 5,00	0,48	2	0,007

Side region total (p and p directions) 13.2
Top region total (p and p directions) 8.4

\+ Floor region

The Detectors Used

1) Gondola (Electromagnetic Calorimeter):

Sandwich of 120 x (1.2 mm Pb + 1.5 mm Polystyrene)
Total 144 mm Pb + 180 mm Polystyrene
26 Radiation lengths or 1 absorption length

2) C Module (Hadron Calorimeter):

Sandwich of 16 x (50 mm Fe + 10 mm Plexiglas)
Total 800 mm Fe + 150 mm Plexiglas
45 Radiation Lengths or 5 Absorption lengths[2)]

3) Muon Chamber:

8 Planes of 12 and 13 drift tubes each with
2 x 7.5 cm drift space
Total 100 drift tubes

4) Additional Hadron Calorimeters

Sandwich of 5 x (40 mm Fe + 15 mm Plexiglas)
Total 200 mm Fe + 60 mm Plexiglas
11.4 Radiation lengths or 1.3 Absorption lengths[2)]

+ 25 mm Pb = 4.5 Radiation Lengths

Table 3

[2)] L_{abs} of iron taken to be 17.0 cm.

Material depths at various counter positions for the three absorber thicknesses D1, D2, and D3, as well as the lowest kinetic energy of a muon needed to reach these counters.

Counter Position		Absorber Thickness D1	D2	D3	
	T2	102,0	126,2	150,5	cm Fe
		1,35	1,65	1,95	GeV
	M1	124,2	148,5	172,8	cm Fe
		1,60	1,90	2,25	GeV
	M2	164,2	188,5	212,8	cm Fe
		2,13	2,50	2,80	GeV

[commas should be read as decimal points]

The absorber thicknesses of the various materials were transformed into equivalent thicknesses of iron, using the energy loss of a minimum-ionizing particle.

The muon ranges are taken from JOS69.

Table 4

[Commas should be read as decimal points]

Table 5

Transverse Momentum Interval ΔP_t (GeV/c)	Exit Probability for Hadrons (%)			Pion rate per P_t Interval (s^{-1})	Punch-Through Rate (s^{-1})		
					D1	D2	D3
1,62 - 1,74	0,38	0,13	0,04	700	1,330	0,443	0,148
1,74 - 2,00	0,45	0,15	0,05	700	1,575	0,525	0,175
2,00 - 2,33	0,57	0,19	0,06	420	1,197	0,399	0,133
2,33 - 2,66	0,71	0,24	0,08	246	0,873	0,291	0,097
2,66 - 3,00	0,87	0,29	0,10	98	0,426	0,142	0,047
3,00 - 3,33	1,05	0,35	0,12	42	0,221	0,074	0,025
3,33 - 3,66	1,23	0,41	0,14	32	0,197	0,066	0,022
3,66 - 4,00	1,43	0,48	0,16	16	0,114	0,038	0,013
4,00 - 4,33	1,64	0,55	0,18	8	0,066	0,022	0,007
4,33 - 4,66	1,85	0,62	0,21	6	0,056	0,019	0,006
4,66 - 5,00	2,08	0,69	0,13	2	0,021	0,007	0,002

Side region total (p and $\bar{p}$ directions) 6.08

Top region total (p and $\bar{p}$ directions) 4.74

\+ Floor region

Figure Captions

Fig. 1 Energy Loss for Particles heavier than electrons, in air (From ROS52).

Fig. 2 Number of Electrons in a Shower, Caused by Electrons of Energy E for Various E/ϵ Ratios (From ROS41).

Fig. 3 Development of a Hadron Shower in an Iron Absorber (From FLO78).

Fig. 4 View of the UA1 Detector. The magnet is only partially covered with muon chambers.

Fig. 5 Side View of the UA1 Detector.

Fig. 6 Spatial Arrangement of the Drift Tubes in a Module (in Principle).

Fig. 7 Overlapping of the Various Regions of the Muon Detector and the Hadron Calorimeters.

Fig. 8 Coverage of the Regions by the Muon Chambers. The dashed line shows the edge of the small chamber lying under the large chamber.

Fig. 9 Construction Drawing of the End of a Chamber with Gas Shaft.

Fig. 10. Electron Drift Velocity in a Gas Mixture of 40% Argon and 60% Ethane as Function of the Electric Field Strength (From MAR79).

Fig. 11 View of the Drift Tube Profile. The wall thickness is 3 mm, the total width 150 mm, the height 45 mm.

Fig. 12 Dependence of the Electric Field Strength on the Distance from the Anode, at the Center of the Tube as well as at a Distance of 4 mm from the Center (Top). Shape of the sensitive volume at the standard voltages on the electrodes (Bottom) (From EGG80).

Fig. 13 Experimental Arrangement for the Calibration of the Location-Time Relationship. The drift tube may be rotated as well as translated. The particle beam is defined by the three drift chambers.

Fig. 14 Dependence of the Detection Probability of the Drift Tube on the Distance from the Anode.

Fig. 15 Dependence of the Mean Pulse Height (Solid Line) and the Width of the Pulse Height Distribution (Full width at half height, dashed line) on the Anode Voltage. The pulse height is proportional to the thickness of the sensitive volume.

Fig. 16 {Translator's Note: This Fig. Caption is missing in the manuscript}

Fig. 17 Place-Time Relationship of the Drift Tube for Various Angles of Incidence. For clarity the four relations are each displaced upwards by 10 mm.

Fig. 18 Dependence of the Spatial Resolution on the Drift Time for Various Angles of Incidence.

Fig. 19 Longitudinal Transit Time Difference Between Two Pulses. One point in time is defined by a particle passage at the center of the tube; the second point in time by a pulse at a specified distance from the center of the tube. In addition the achievable spatial resolution in the longitudinal direction is shown.

Fig. 20 P_t Spectrum of the Primary Pions Produced by the $p\bar{p}$ Collisions (From ALP75).

Fig. 21 Side View of the Experiment for Determining the Hadronic Background in Muon Identification.

Fig. 22 Top View of the Same Experiment.

Fig. 23 Acceptance of the Muon Trigger as Function of the Pion Momentum. The dashed line shows the expected rate for a decay space 22 m in length and without beam telescope.

Fig. 24 Correlation Between the Muon Momentum and the Angle of Emission relative to the Flight Path of the Pions in the Decay of Pions, for Various Momenta.

Fig. 25 Block Circuit Diagram of the Trigger.

Fig. 26 Block Circuit Diagram of the Measured-Date Acquisition and the Connection to the Monitor.

Fig. 27 Picture of a Hadron Event from the On-Line Display.

Fig. 28 Polaroid Picture of the Monitor Display Screen.

Fig. 29 Acceptance of the Anti-Muon Trigger as Function of Beam Momentum.

Fig. 30 Exit Probability for Hadrons from the Hadron Calorimeter, Measured in Front of and Behind the Muon Chamber, as Function of the Beam Momentum.

Fig. 31 Measured Damping Lengths for Decaying Hadron Showers in Iron.

Fig. 32 The Muon Energy Spectrum. The total energy, the sum of the energies deposited in all the calorimeters is shown.

Fig. 33 Energy Spectrum of a Punch-Through Event for the Same Momentum as in Fig. 32.

Fig. 34 Energy Spectrum of a Punch-Through Event. This time the momentum is 5 GeV/c and the thickness is D3.

Fig. 35 Total Energy Deposited in all the Calorimeters, Collected with the Anti-Muon Trigger, Plus the Energies of the Minimum-Ionization Particles (dashed line). The solid line designates the expected energy for total absorption in the calorimeter.

Fig. 36 The Calibration Used for the Drift Tubes.

Fig. 37 Display of a 10 GeV/c Muon. The particle beam is incident from the bottom in all the display images.

Fig. 38 Punch-Through Event at 10 GeV/c.

Fig. 39 Like 38.

Fig. 40 Like 38

Fig. 41 Efficiency of the Muon Chamber as Function of a Relative Chamber Coordinate.

Fig. 42 Time Difference Spectrum $dN/d(\Delta t)$. The Difference is formed between a point on the track and the next hit in the drift tube.

Fig. 43 One Side of the Time Difference Spectrum with an Exponential Fit.

Fig. 44 Average Hit Multiplicities and the 90% Limit of the Individual Distributions as Function of the Beam Momentum for Three Different Absorber Thicknesses.

Fig. 45 Average Track Multiplicities as Function of the Beam Momentum.

Fig. 46 Reduction Factor F_{red} of the Hadronic Background by an Angle Cut in G.

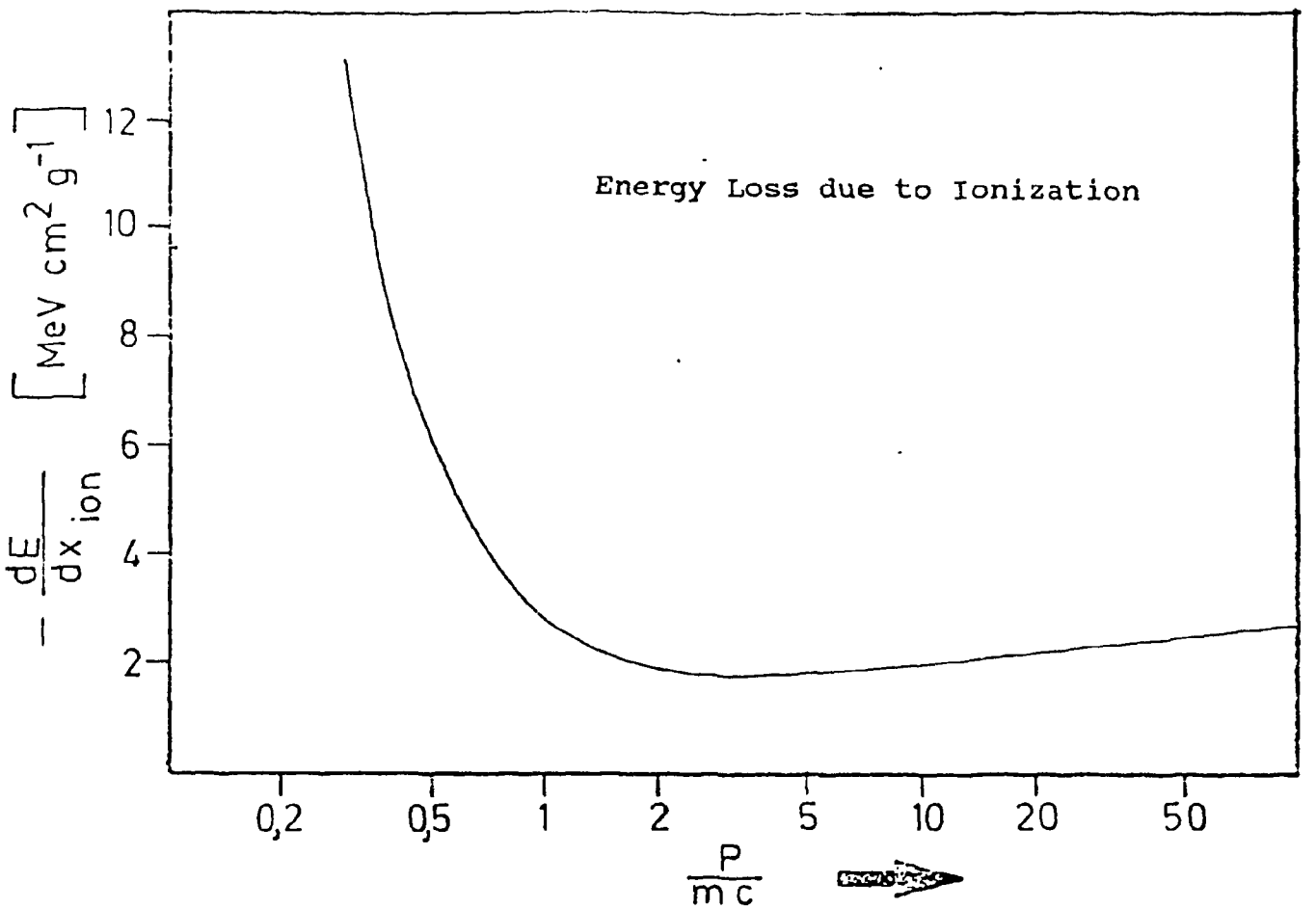

Energy Loss for Particles Heavier than Electrons, in Air (From ROS52).

Fig. 1

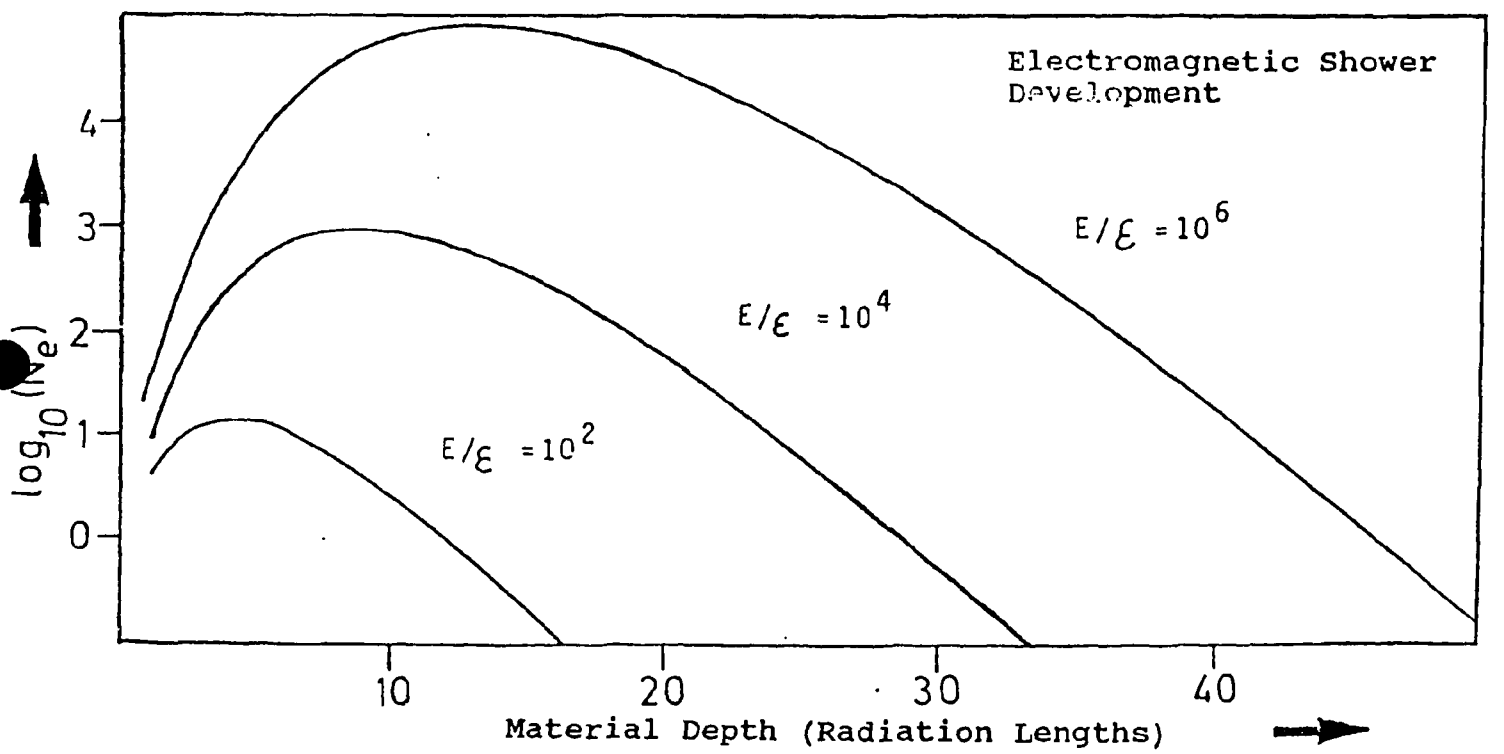

Number of Electrons in a Shower, Caused by Electrons of Energy E for Various E/ϵ Ratios (From ROS41).

Fig. 2

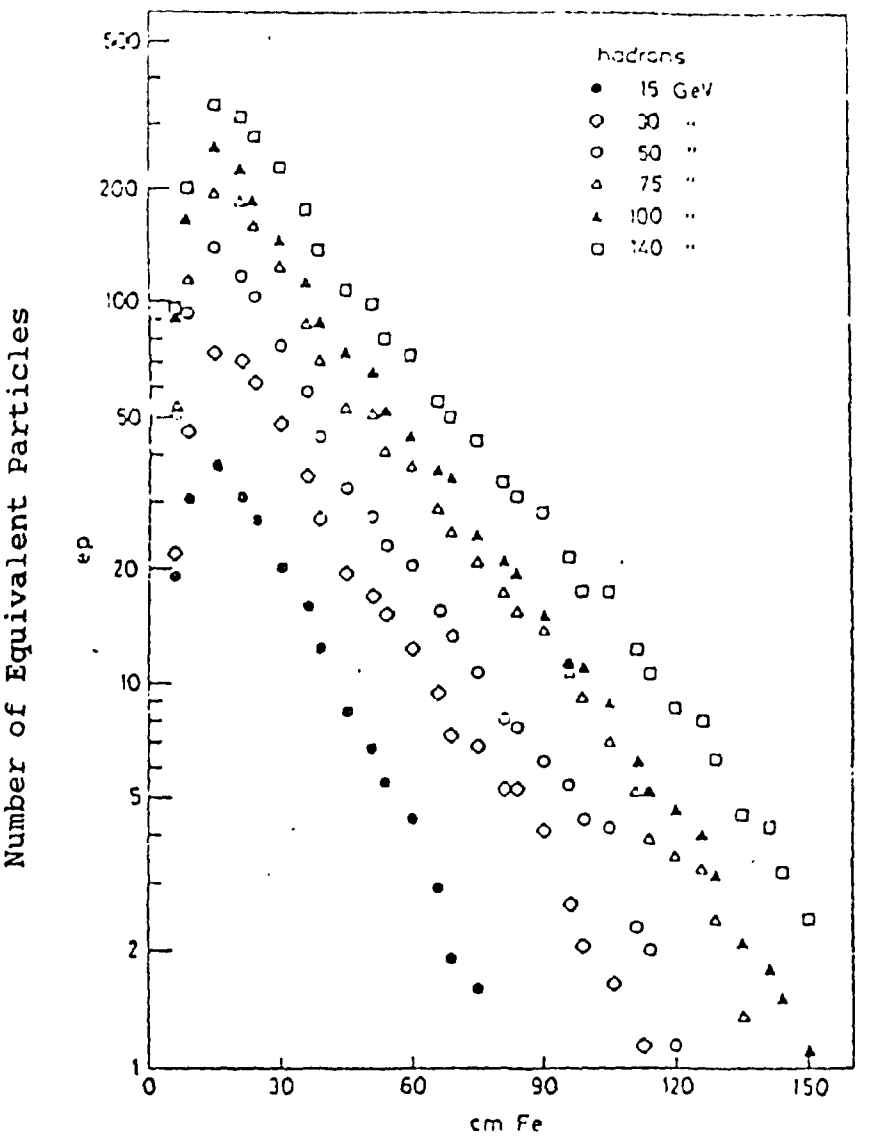

Development of a Hadron Shower in an Iron Absorber (From FLO78).

Fig.3

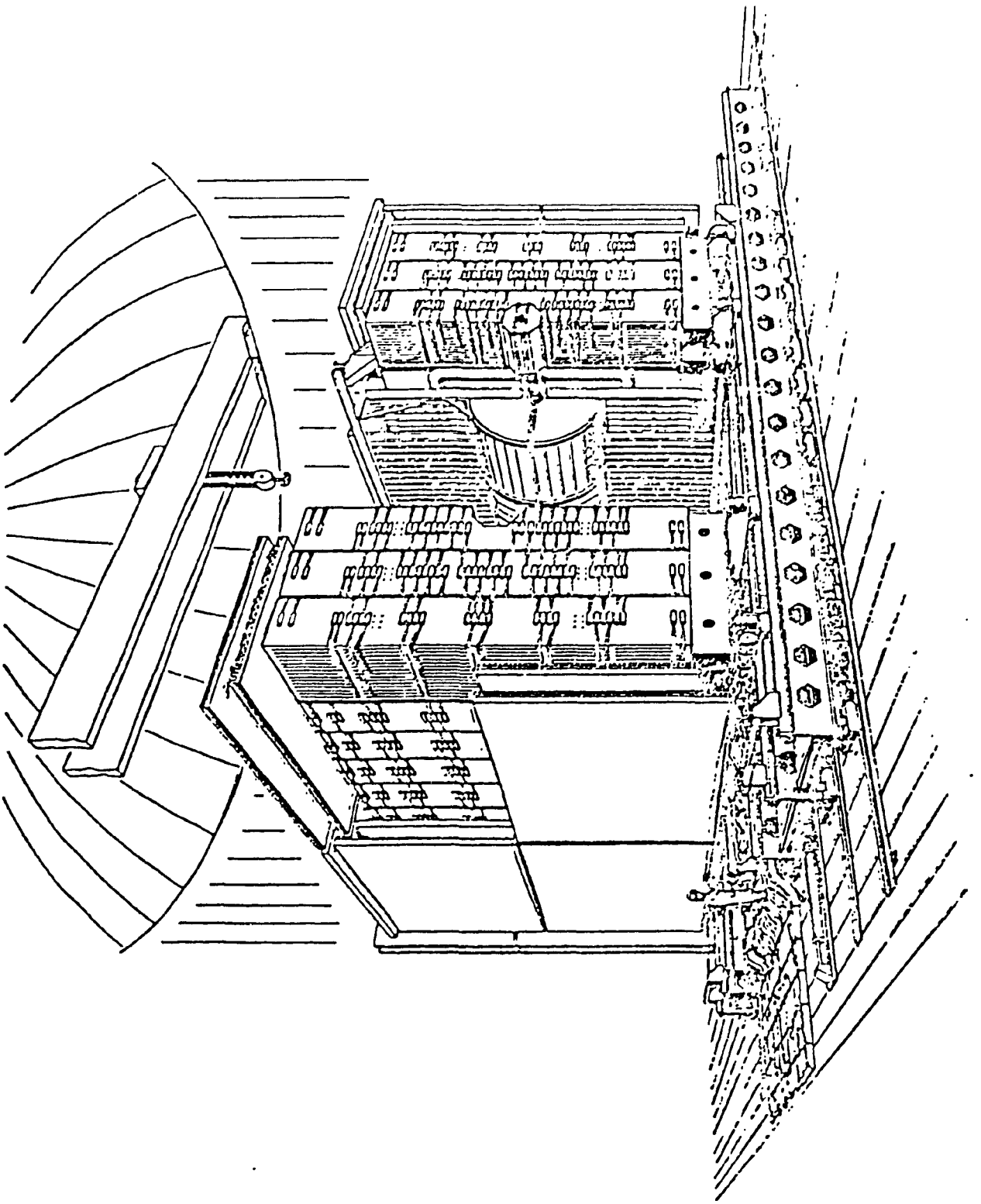

View of the UA1 Detector. The magnet is only partially covered with muon chambers.

Fig. 4

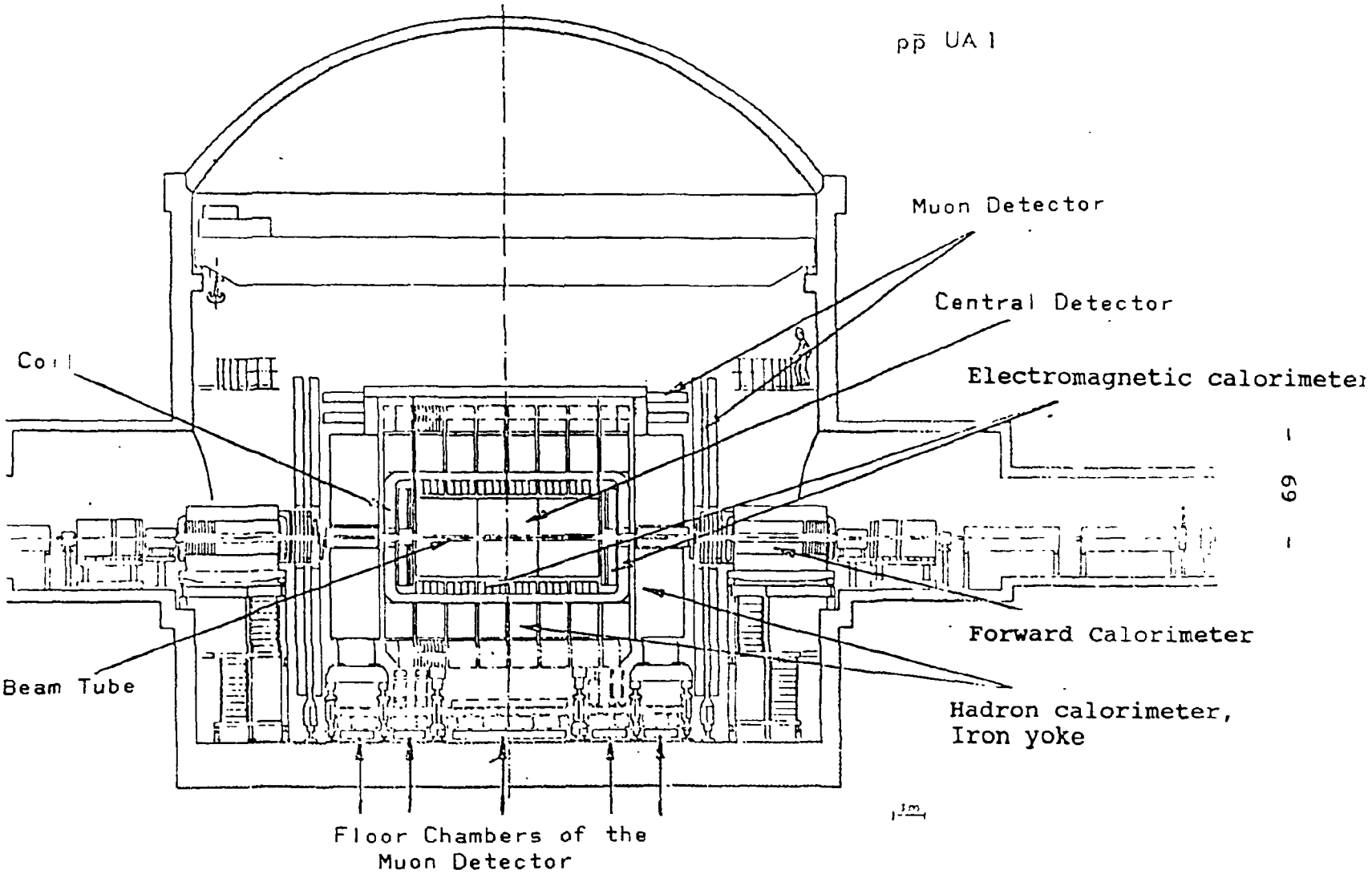

Fig. 5 View of the UA1 Detector.

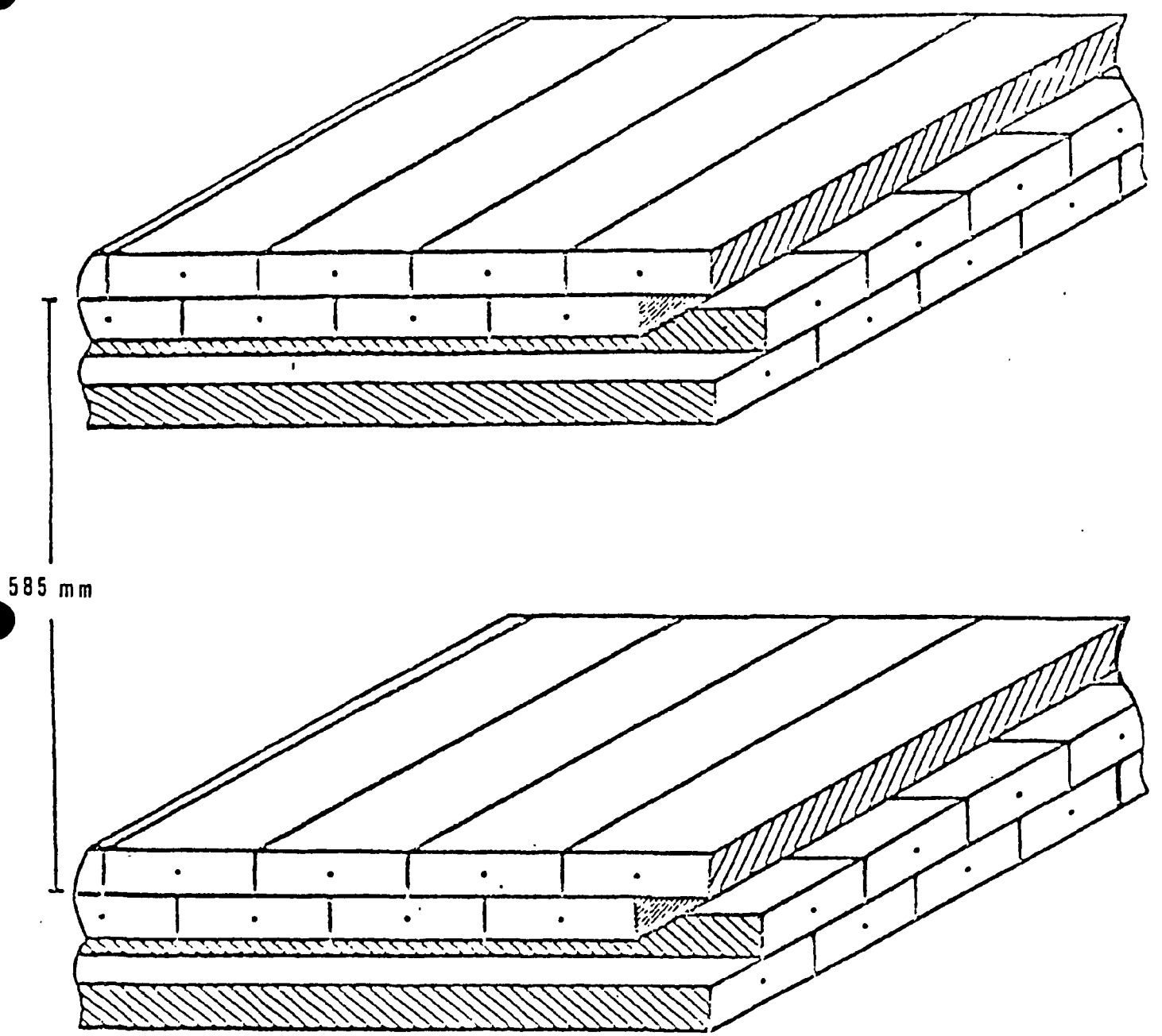

Spatial Arrangement of the Drift Tubes in a Module (in Principle).

Fig. 6

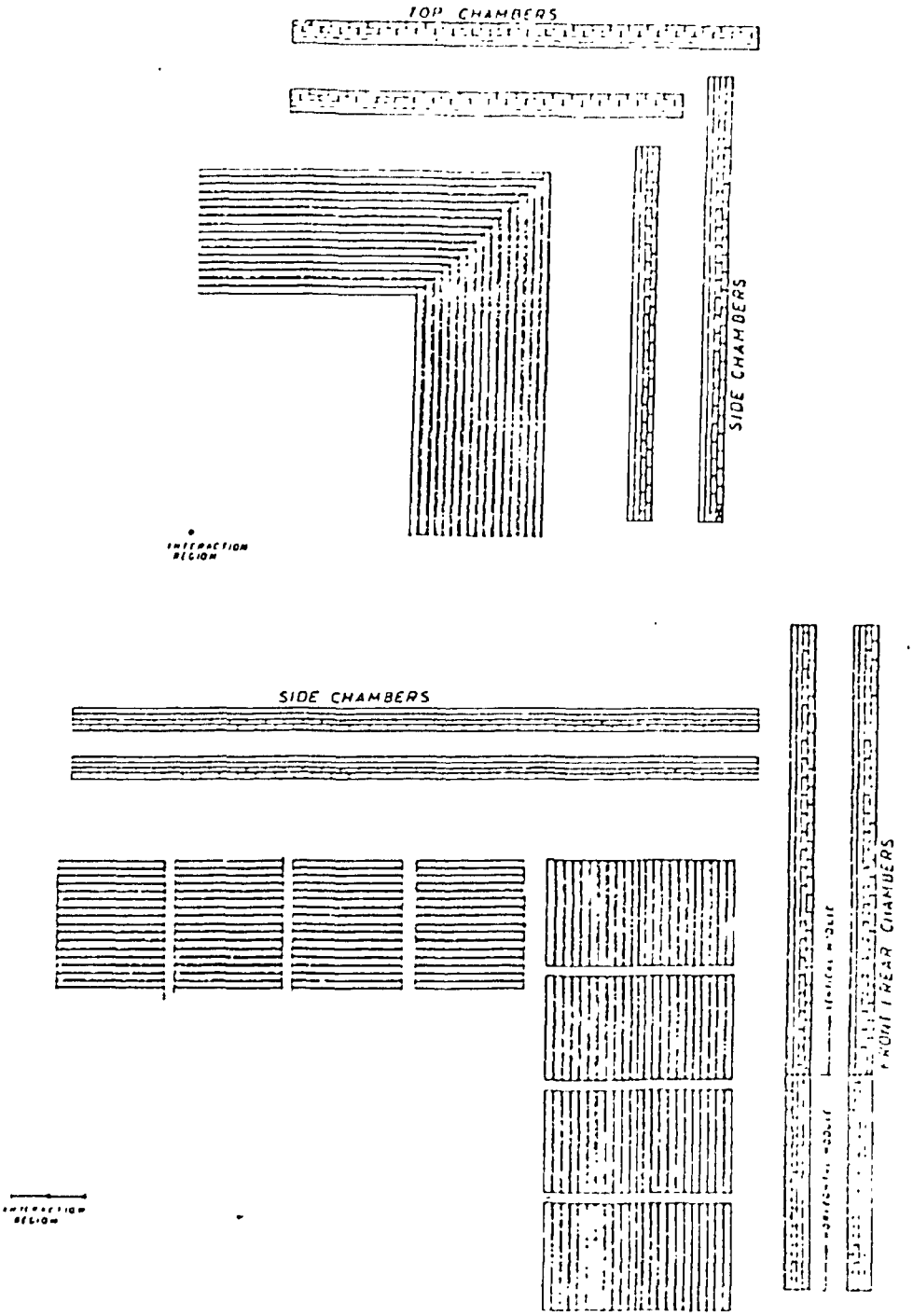

Overlapping of the Various Regions of the Muon Detector and the Hadron Calorimeters.

Fig. 7

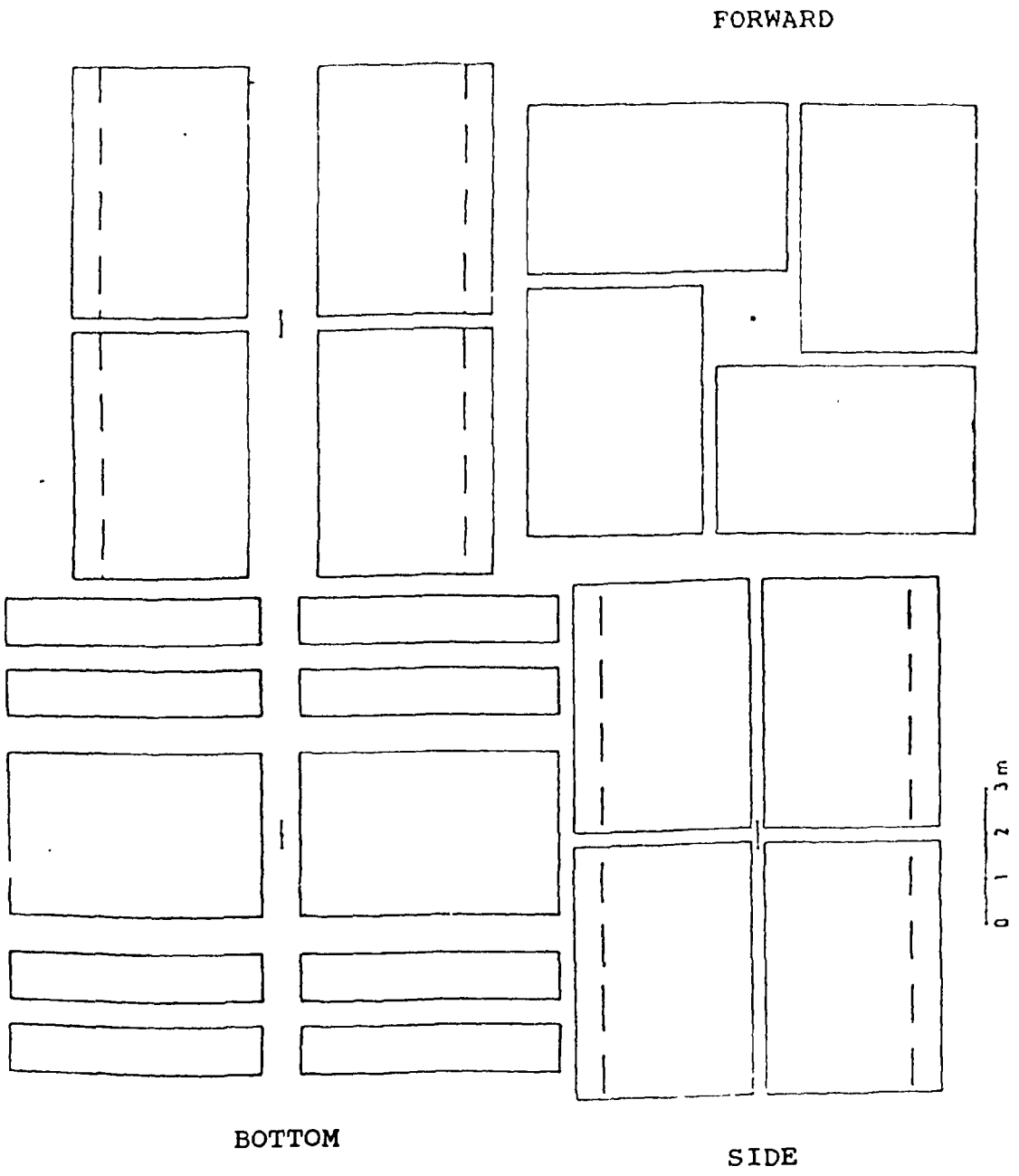

Coverage of the Regions by the Muon Chambers. The dashed line shows the edge of the small chamber lying under the large chamber.

Fig. 8

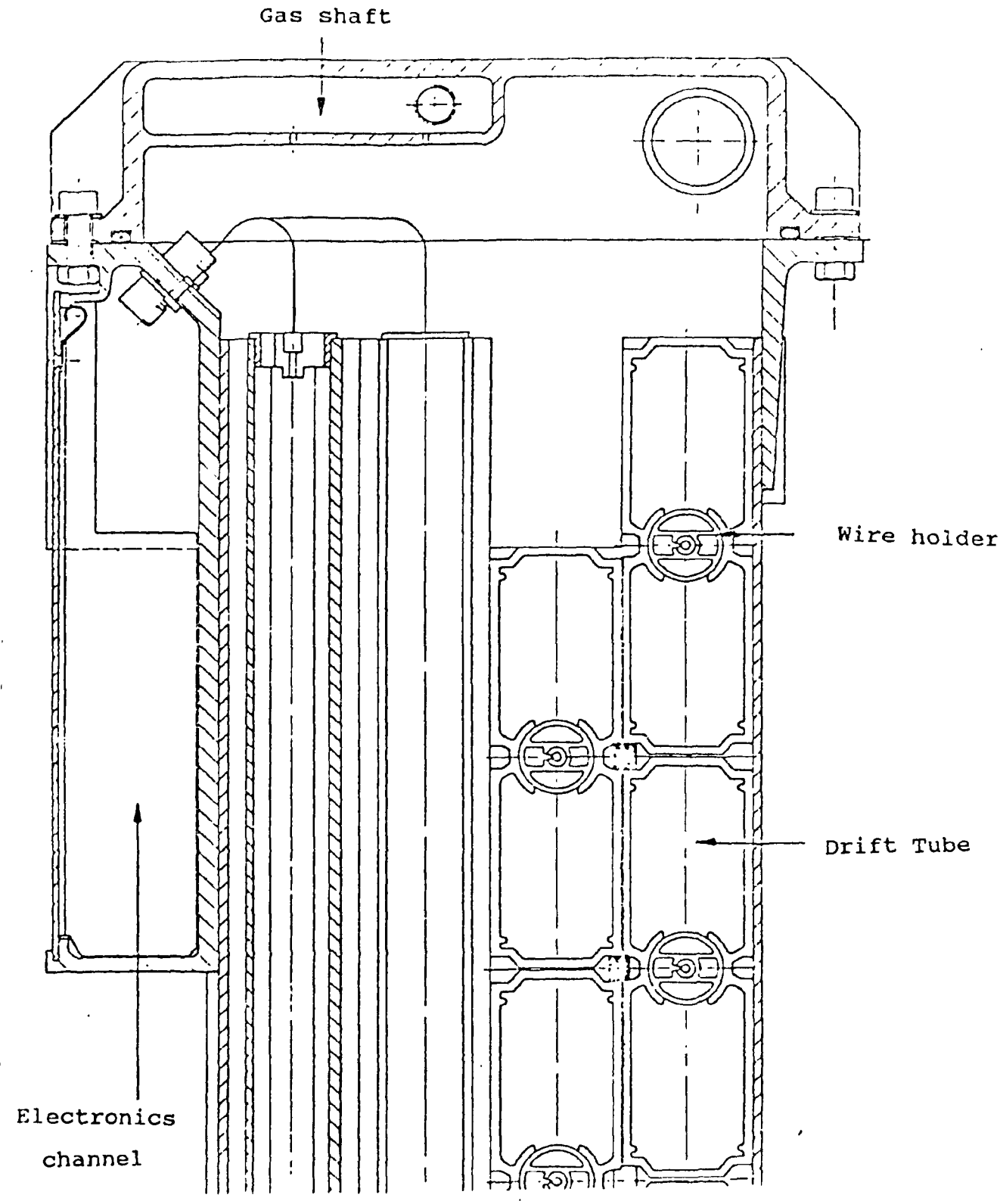

Construction Drawing of the End of a Chamber with Gas Shaft.

Fig. 9

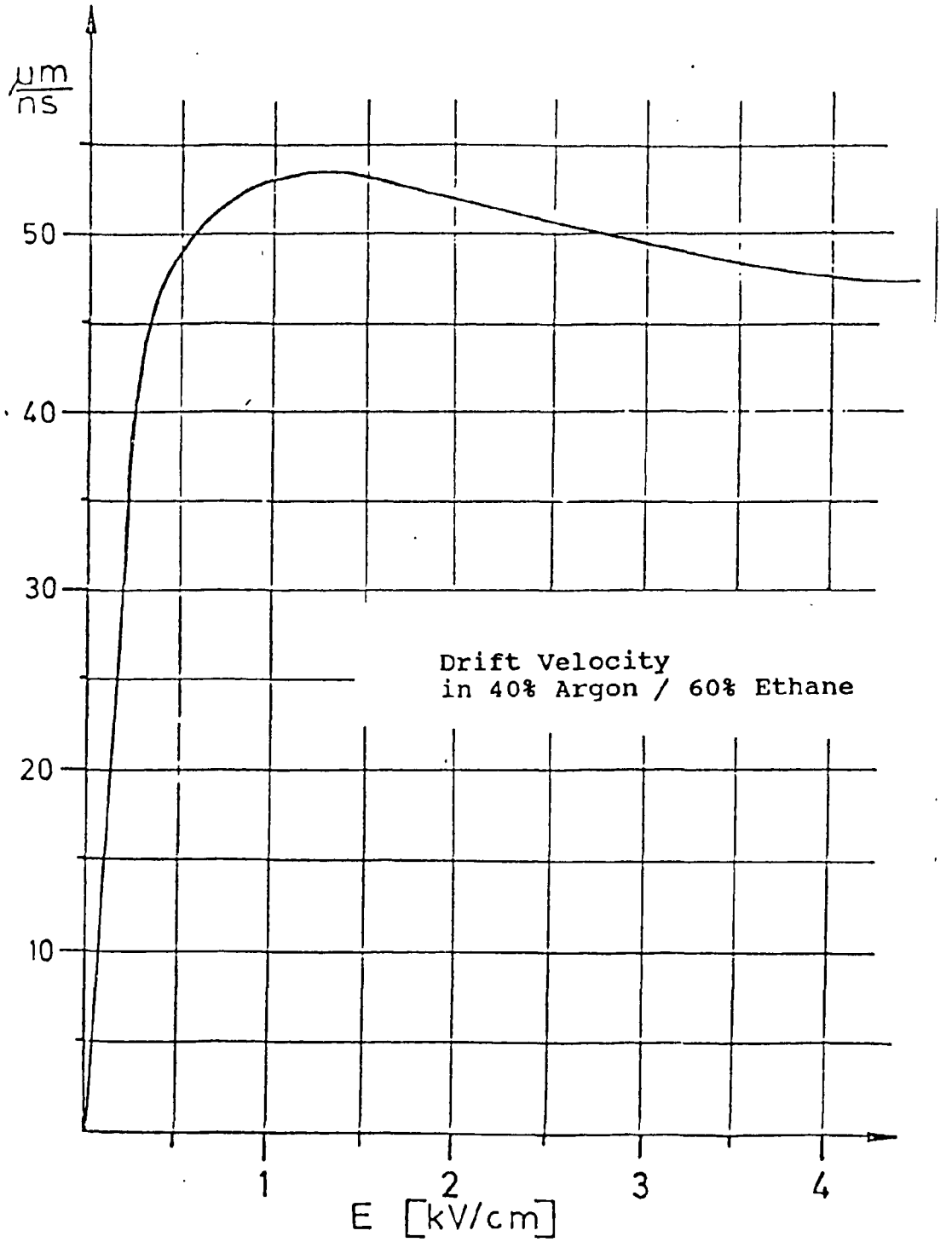

Electron Drift Velocity in a Gas Mixture of 40% Argon and 60% Ethane as Function of the Electric Field Strength (From MAR79).

Fig. 10

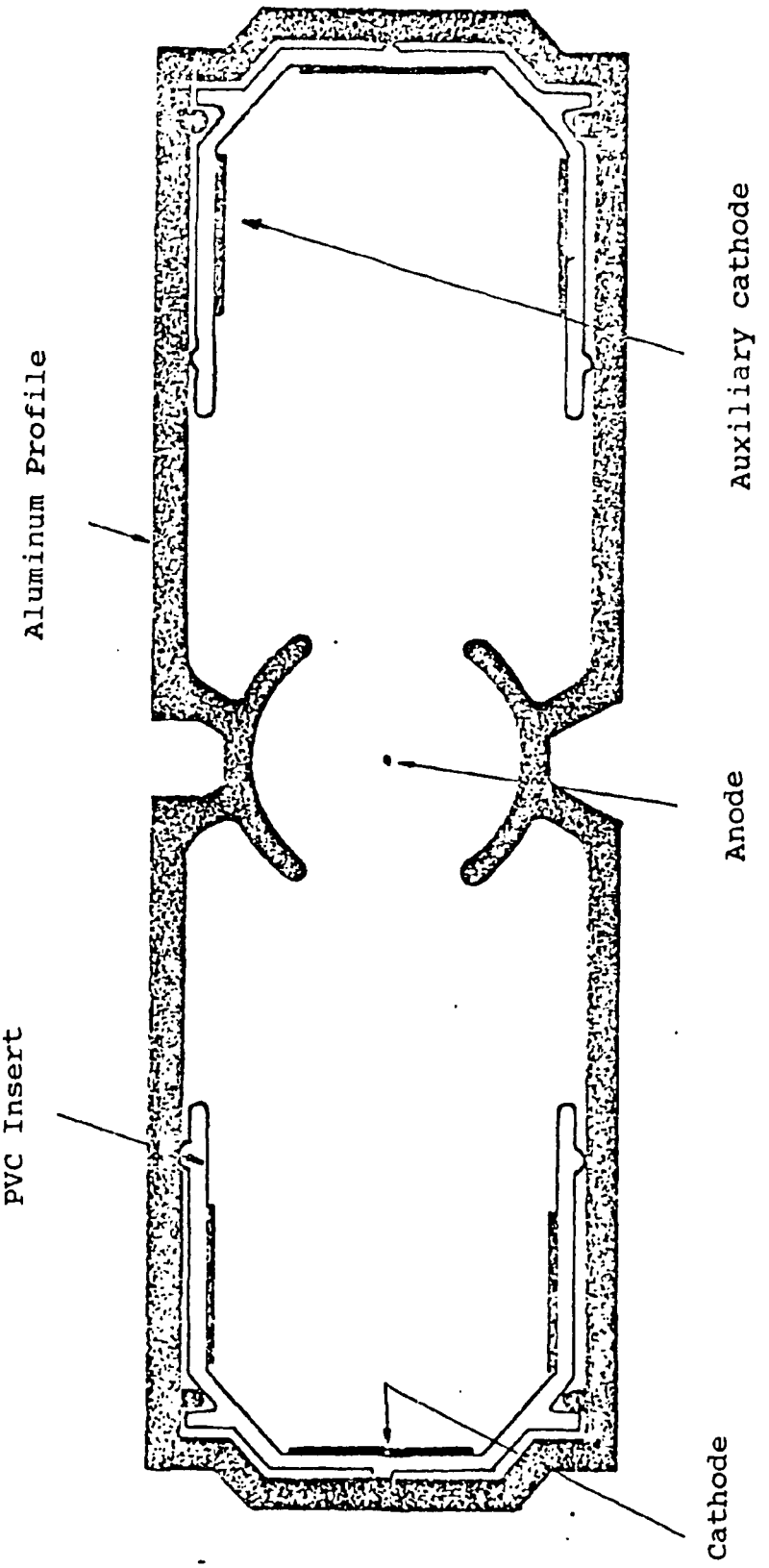

View of the Drift Tube Profile. The wall thickness is 3 mm, the total width 150 mm, the height 45 mm.

Fig. 11

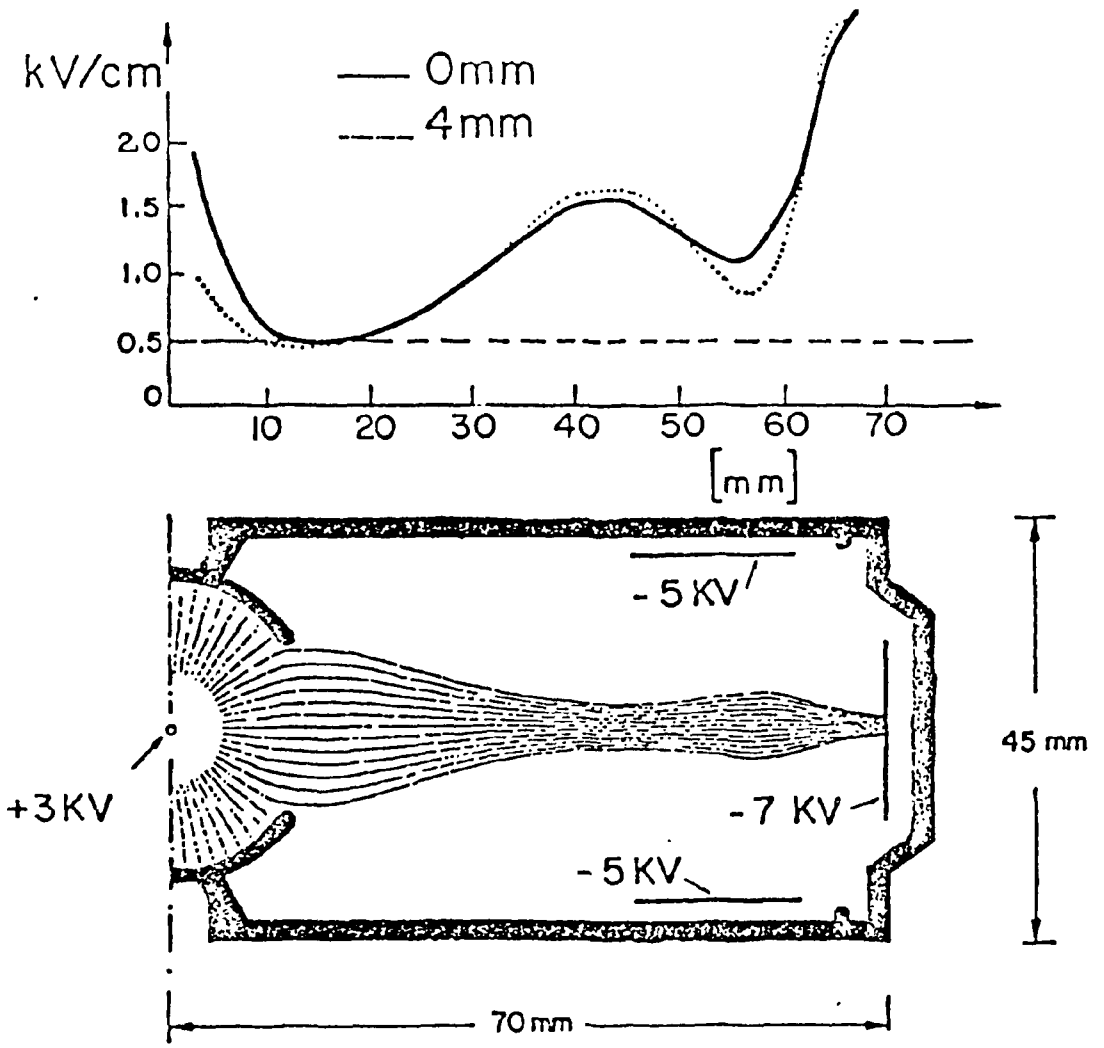

Dependence of the Electric Field Strength on the Distance from the Anode, at the Center of the Tube as well as at a Distance of 4 mm from th Center (Top). Shape of the sensitive volume at the standard voltages on the electrodes (Bottom) (From EGG80).

Fig. 12

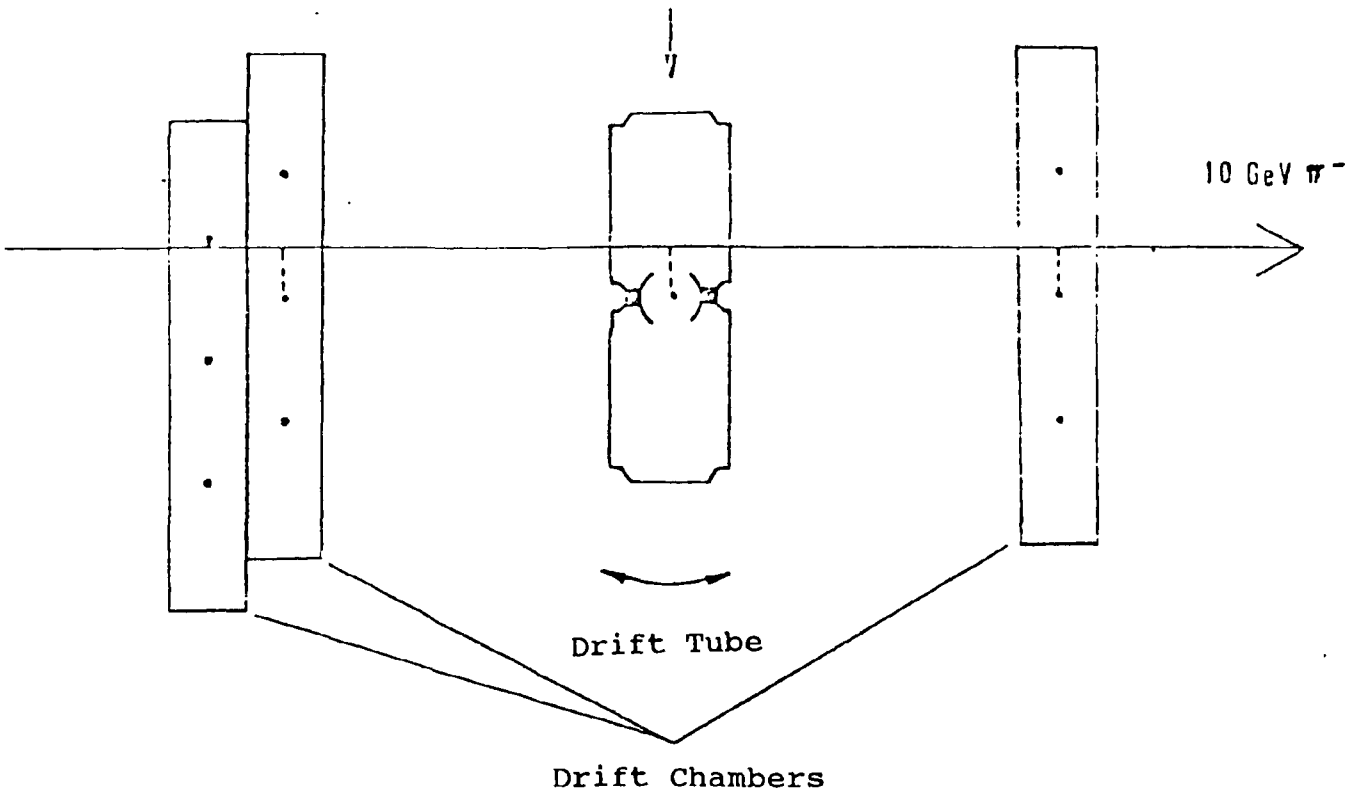

Experimental Arrangement for the Calibration of the Location-Time Relationship. The drift tube may be rotated as well as translated. The particle beam is defined by the three drift chambers.

Fig. 13

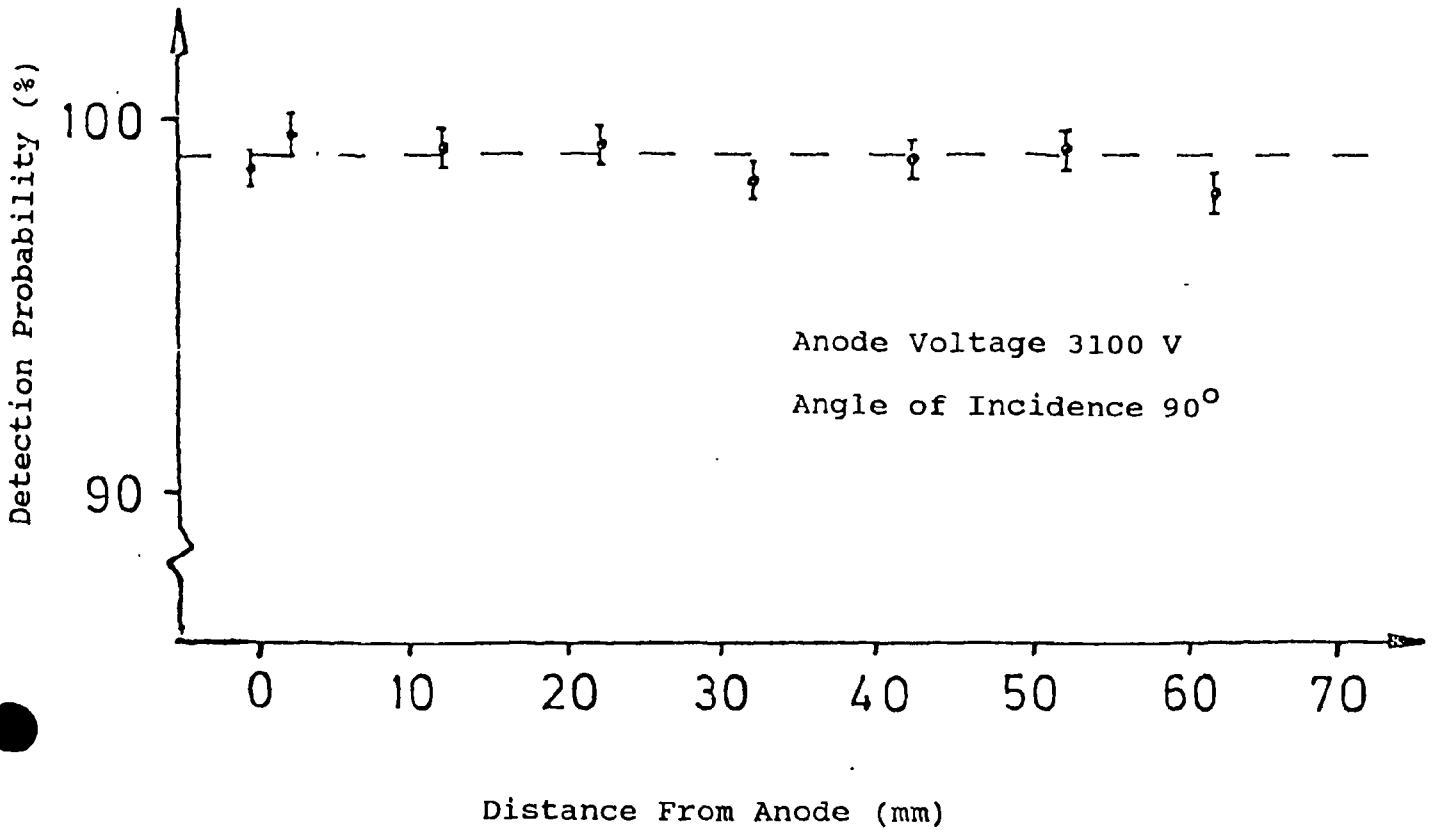

Abb. 14

Dependence of the Detection Probability of the Drift Tube on the Distance from the Anode.

Fig. 14

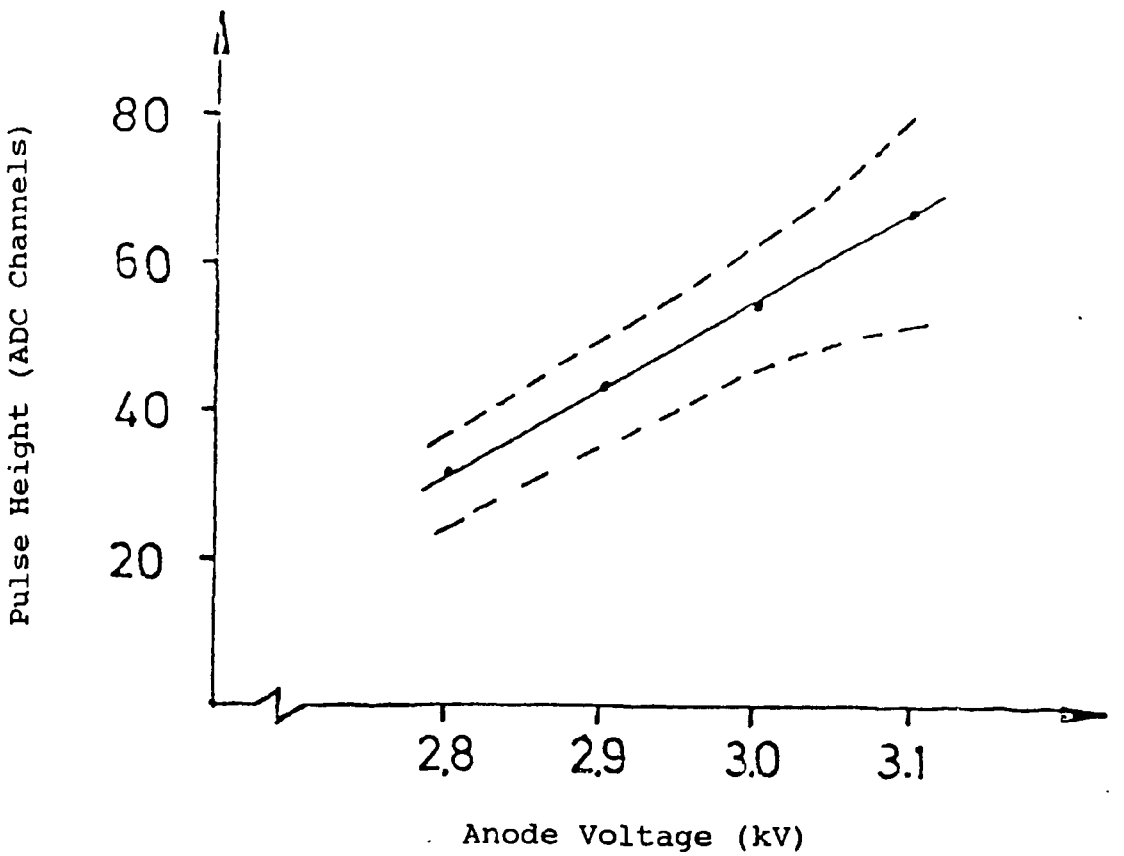

Dependence of the Mean Pulse Height (Solid Line) and the Width of the Pulse Height Distribution (Full width at half height, dashed line) on the Anode Voltage. The pulse height is proportional to the thickness of the sensitive volume.

Fig. 15

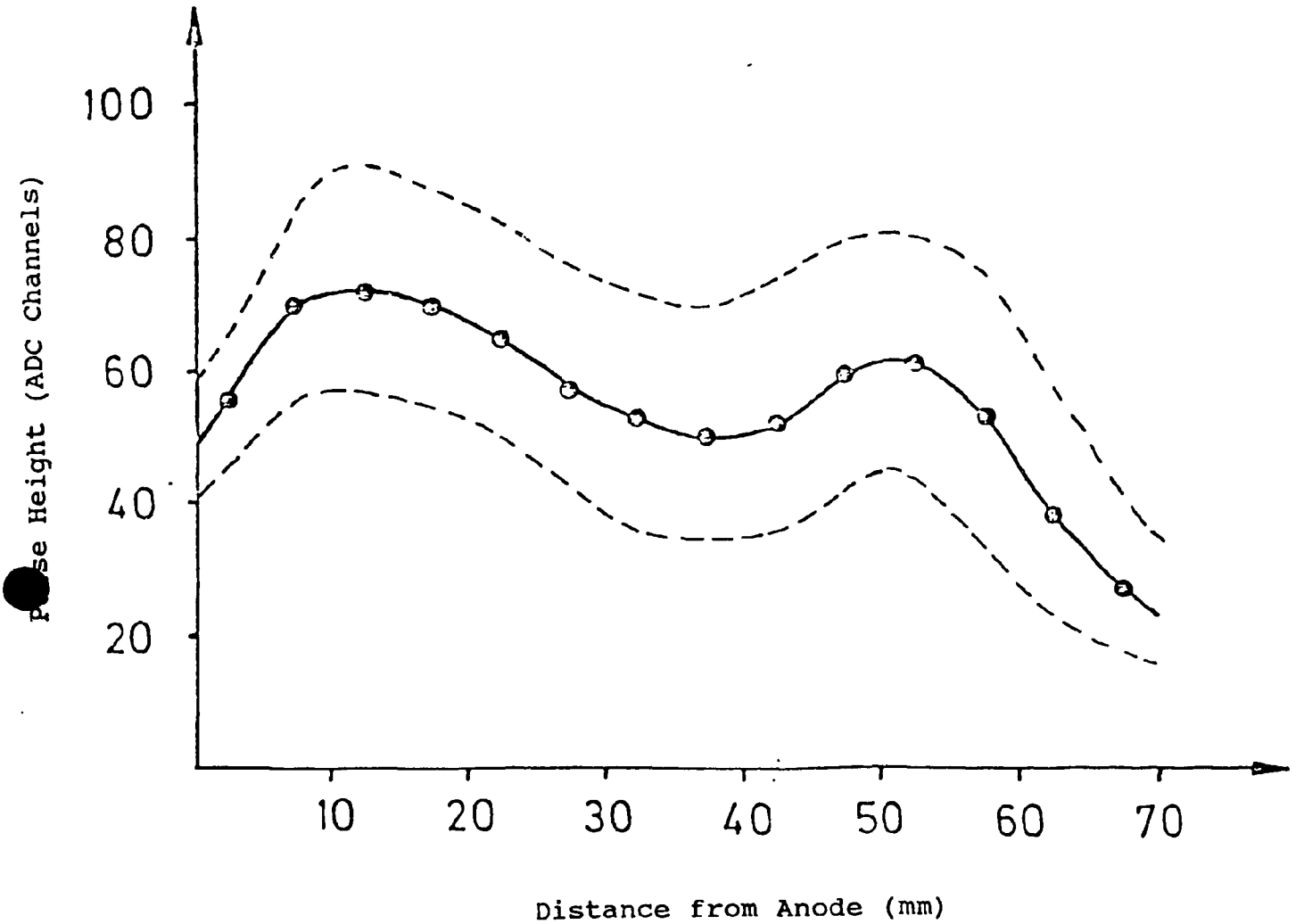

{Translator's Note: This Fig. Caption is missing in the manuscript}

Fig. 16

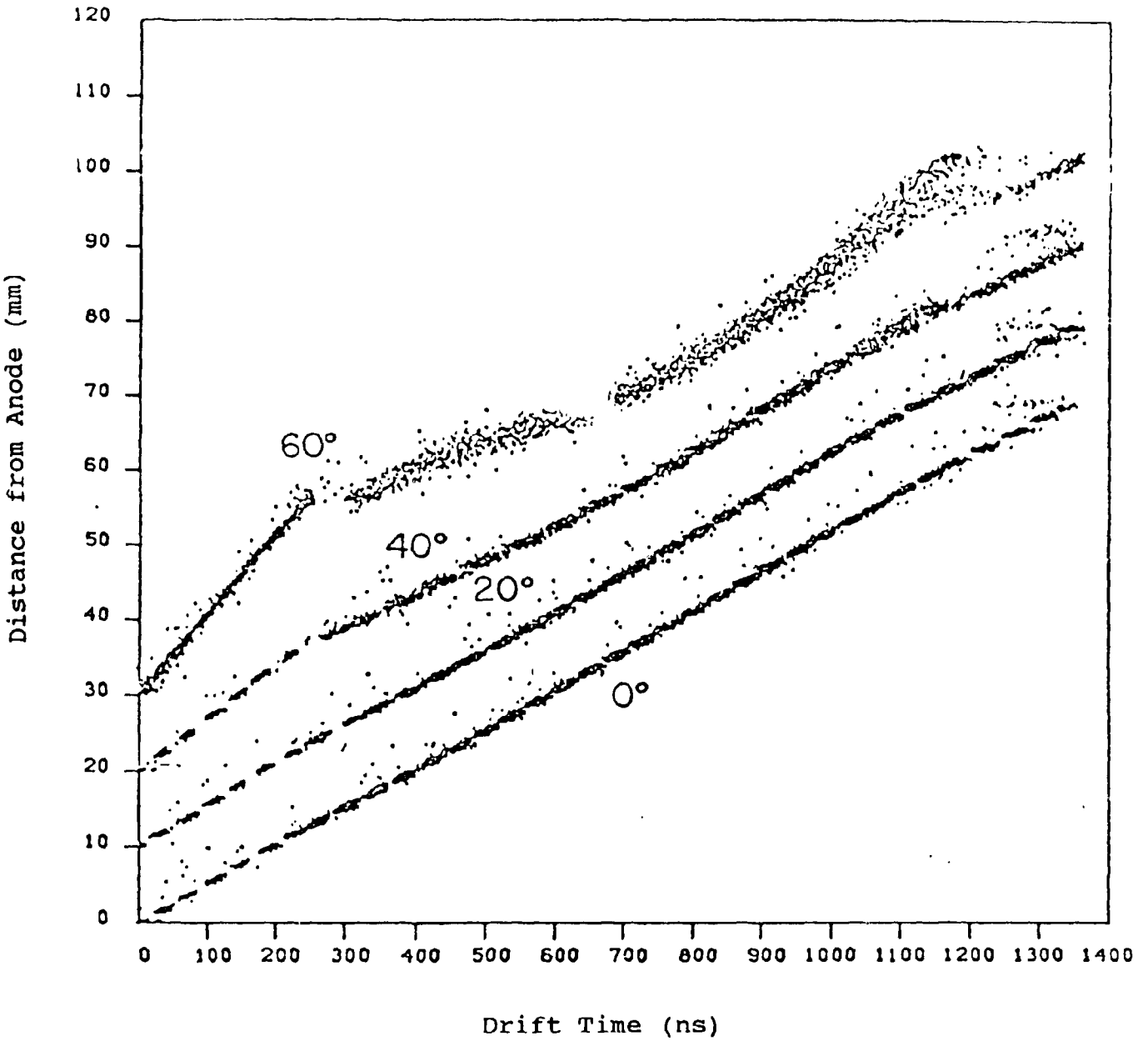

Place-Time Relationship of the Drift Tube for Various Angles of Incidence. For clarity the four relations are each displaced upwards by 10 mm.

Fig. 17

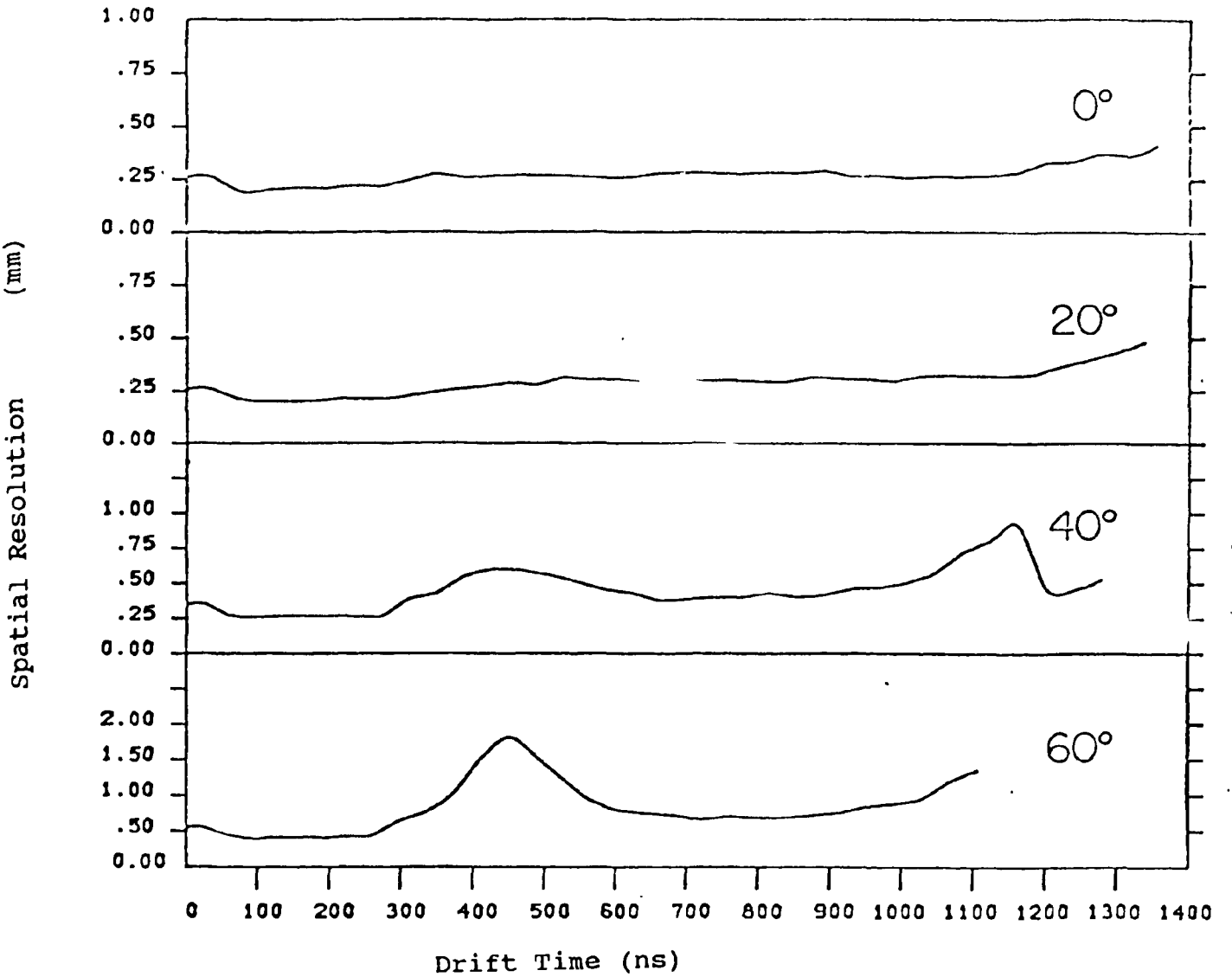

Dependence of the Spatial Resolution on the Drift Time for Various Angles of Incidence.

Fig. 18

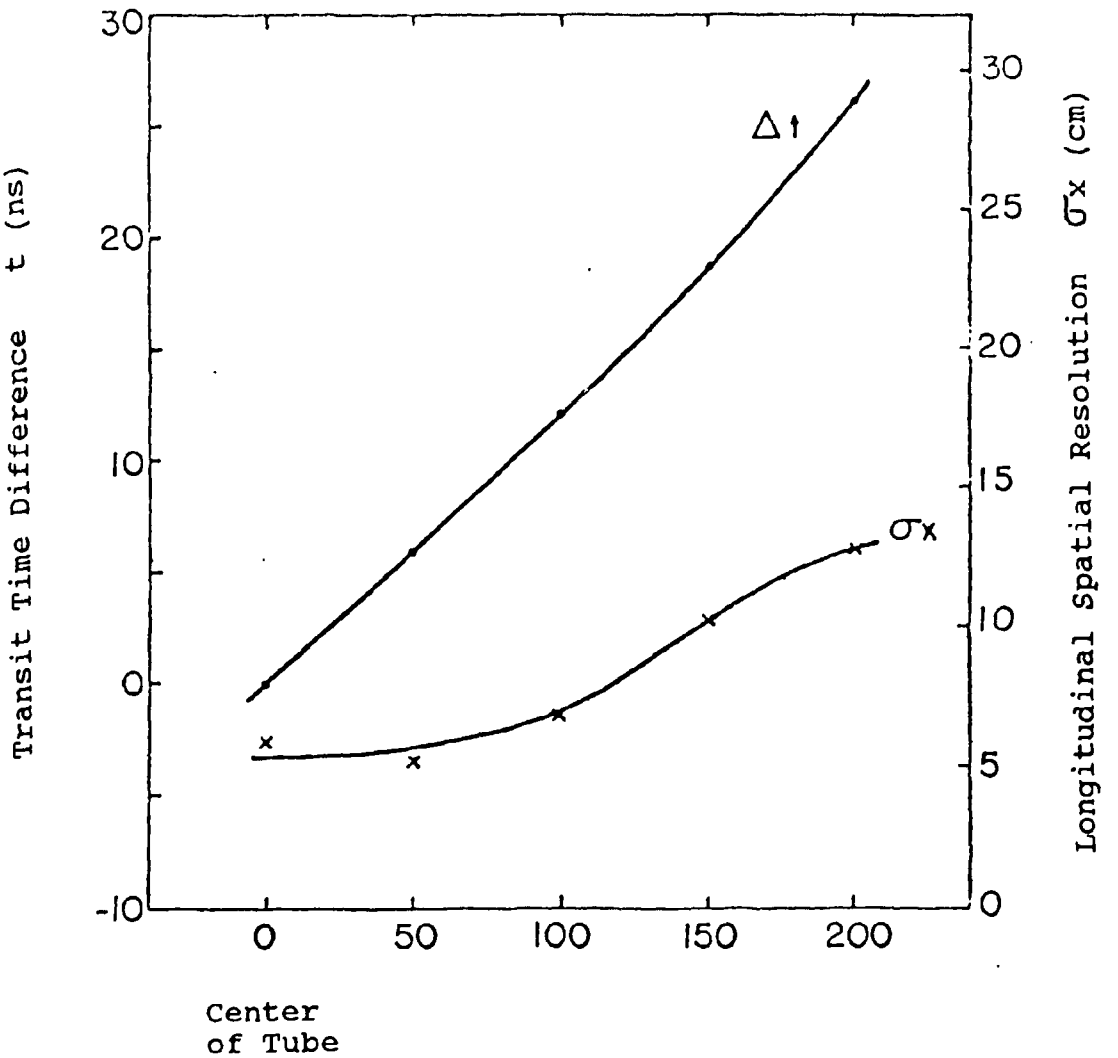

Longitudinal Transit Time Difference Between Two Pulses. One point in time is defined by a particle passage at the center of the tube; the second point in time by a pulse at a specified distance from the center of the tube. In addition the achievable spatial resolution in the longitudinal direction is shown.

Fig. 19

Relative Fraction R of all Pions with a transverse Momentum p_t which is larger than a transverse momentum $p_{t,\,cut}$.

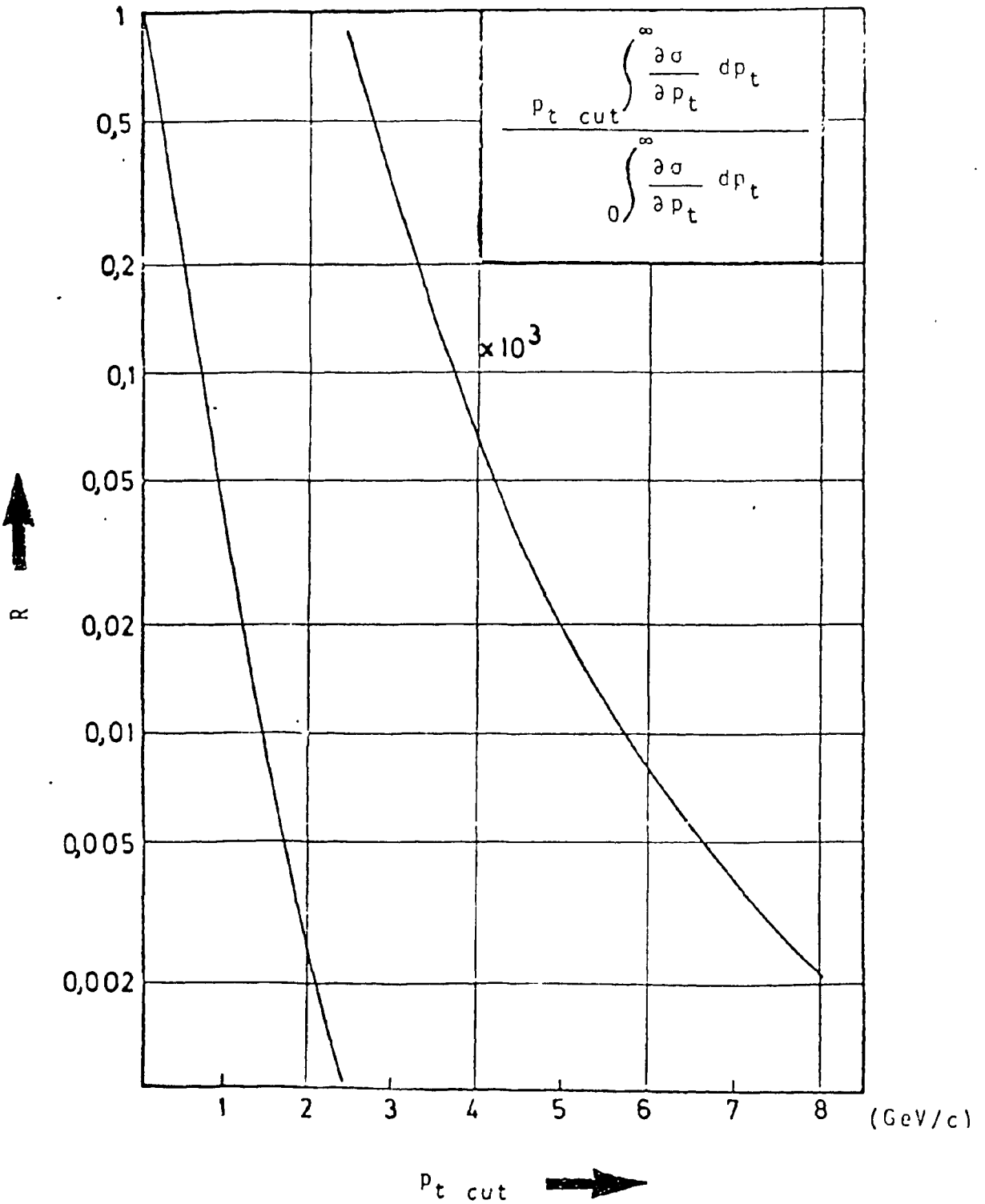

P_t Spectrum of the Primary Pions Produced by the pp Collisions (From ALP75).

Fig. 20

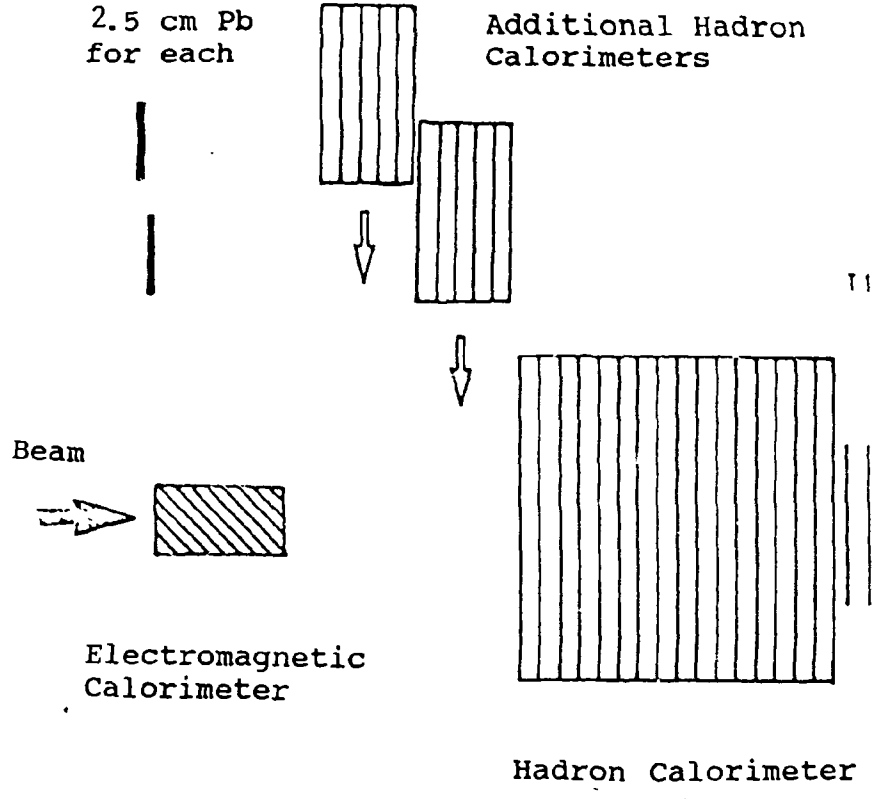
2.5 cm Pb
for each
Additional Hadron
Calorimeters
T1
Beam
Electromagnetic
Calorimeter
Hadron Calorimeter

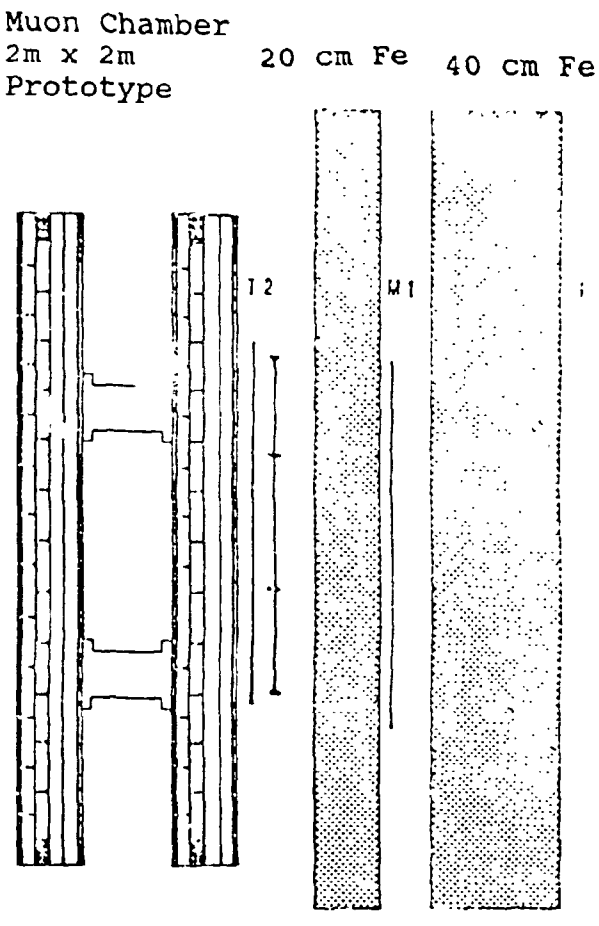
Muon Chamber
2m x 2m
Prototype
20 cm Fe
40 cm Fe
T2
M1

Fig. 21

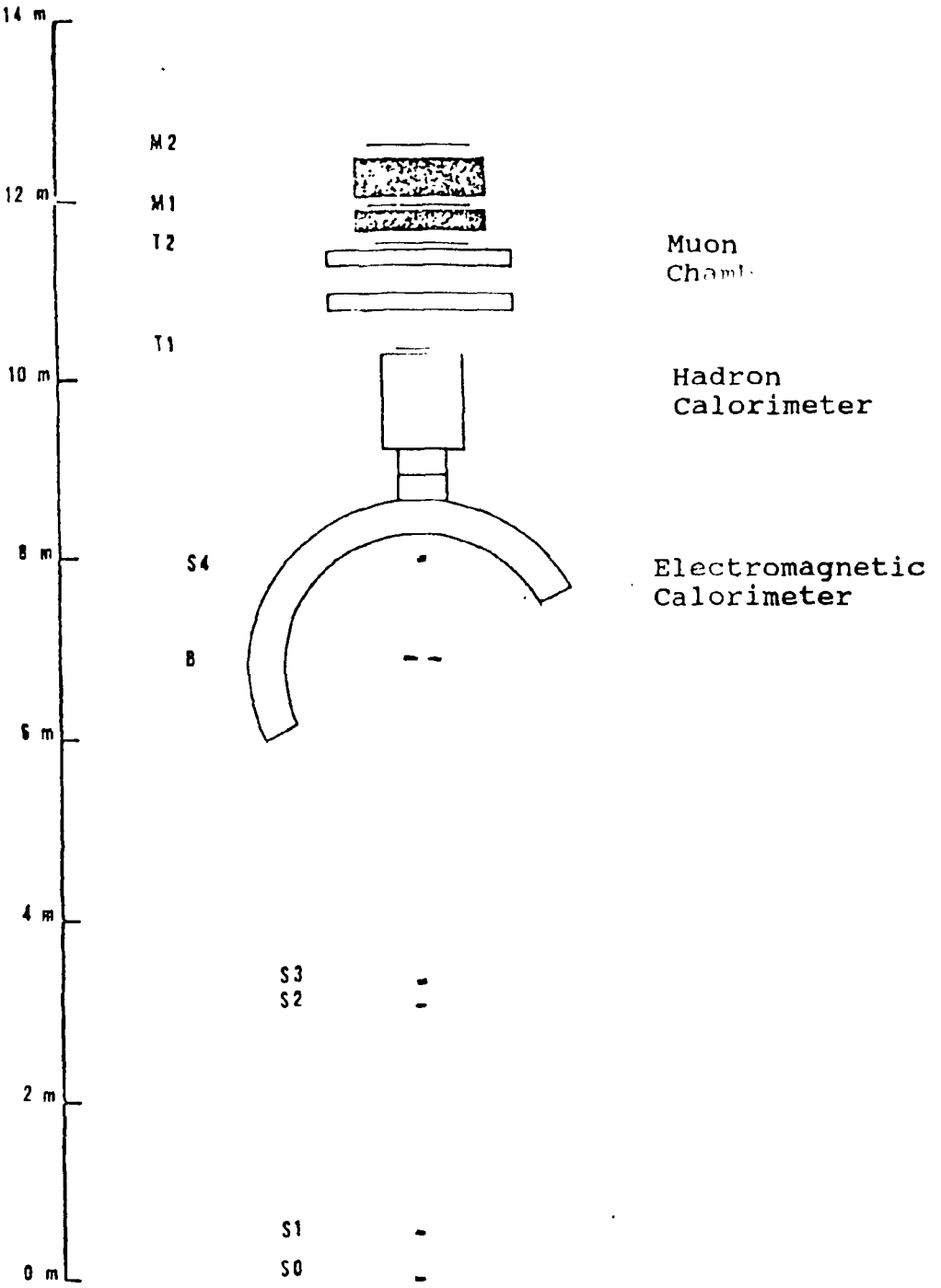

Side View of the Experiment for Determining the Hadronic Background in Muon Identification.

Fig. 22

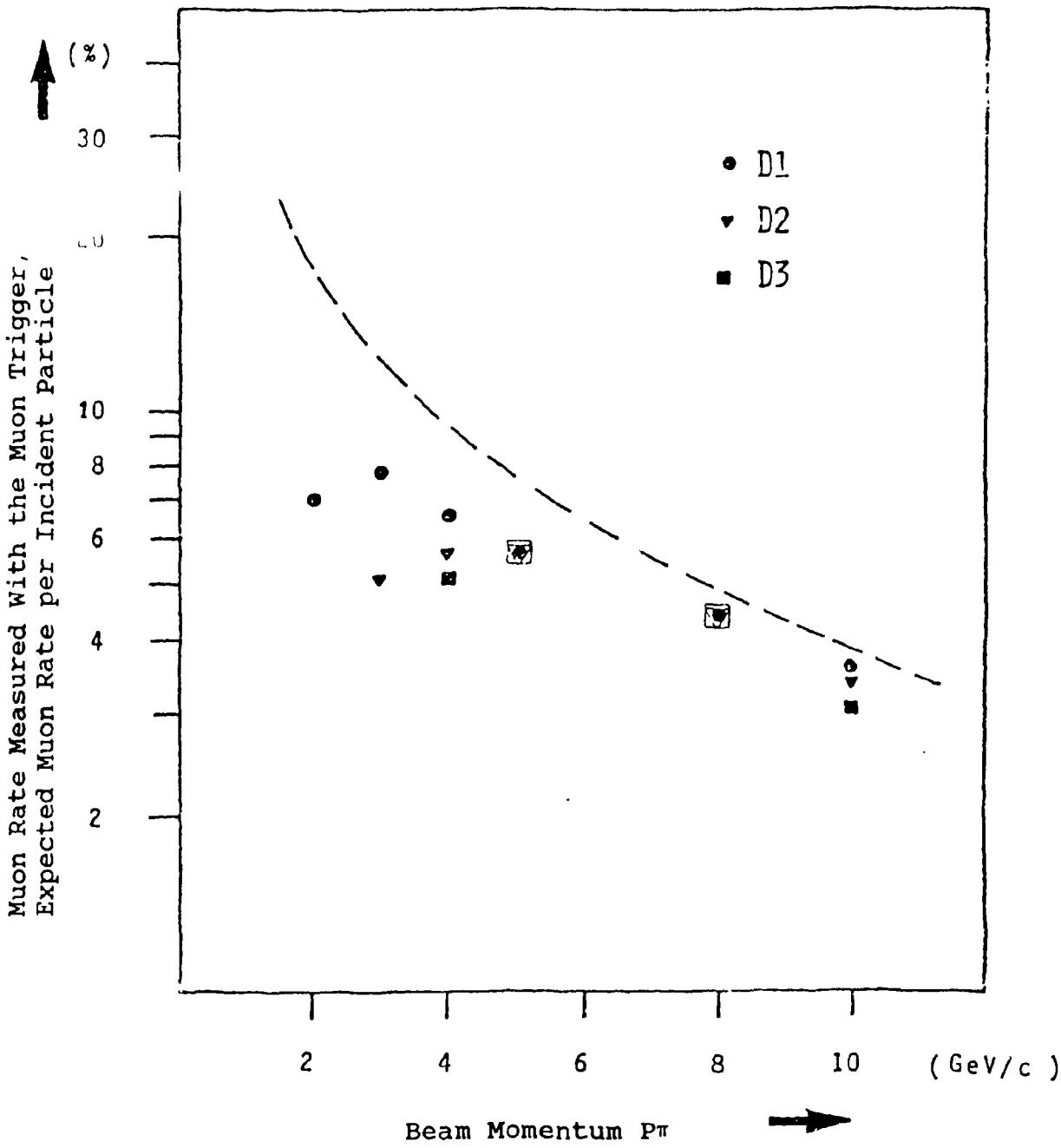
(%)
30
10
8
6
4
2
D1
D2
D3
Muon Rate Measured With the Muon Trigger,
Expected Muon Rate per Incident Particle
2
4
6
8
10
(GeV/c)
Beam Momentum Pπ

Fig. 23

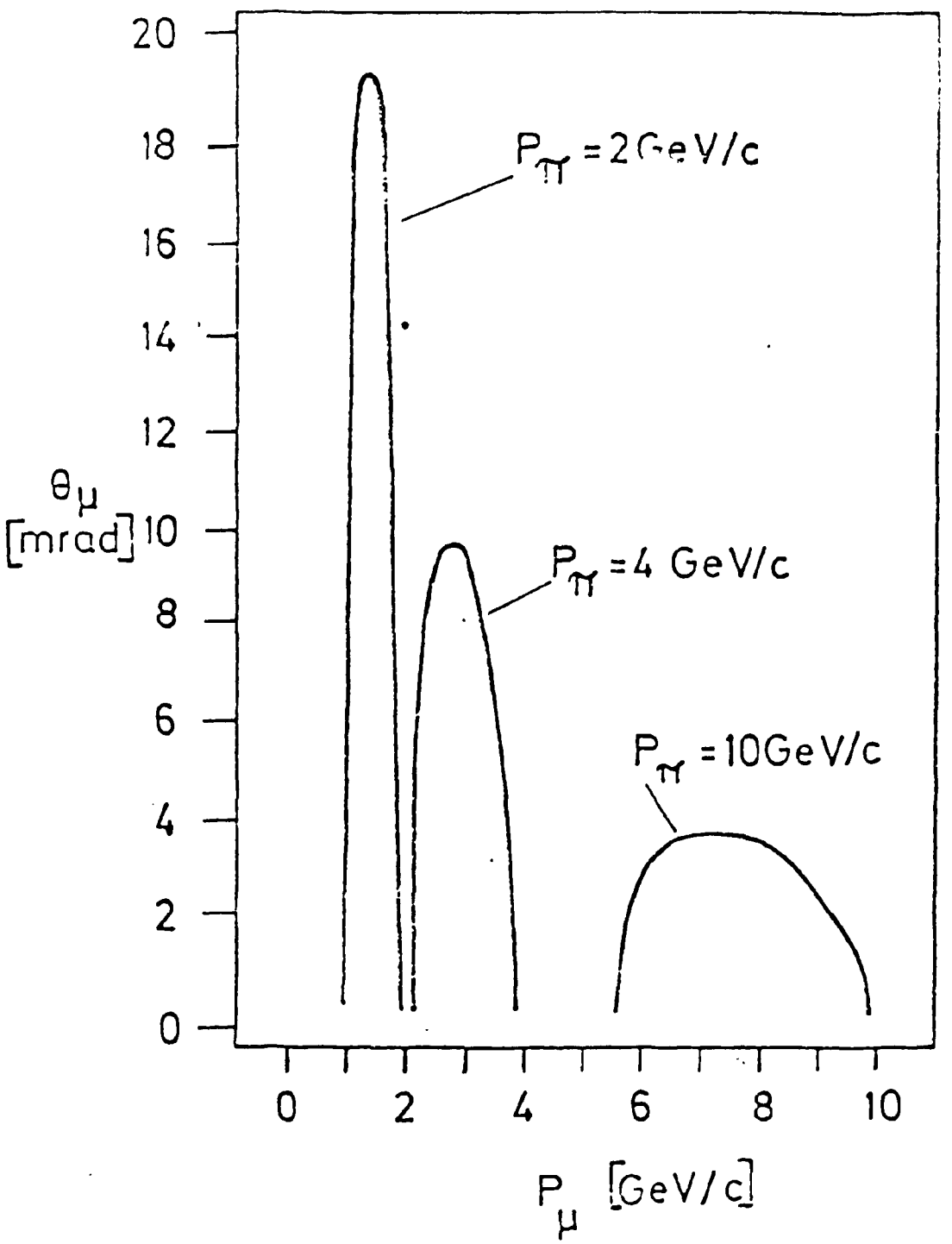

Correlation Between the Muon Momentum and the Angle of Emission relative to the Flight Path of the Pions in the Decay of Pions, for Various Momenta.

Fig. 24

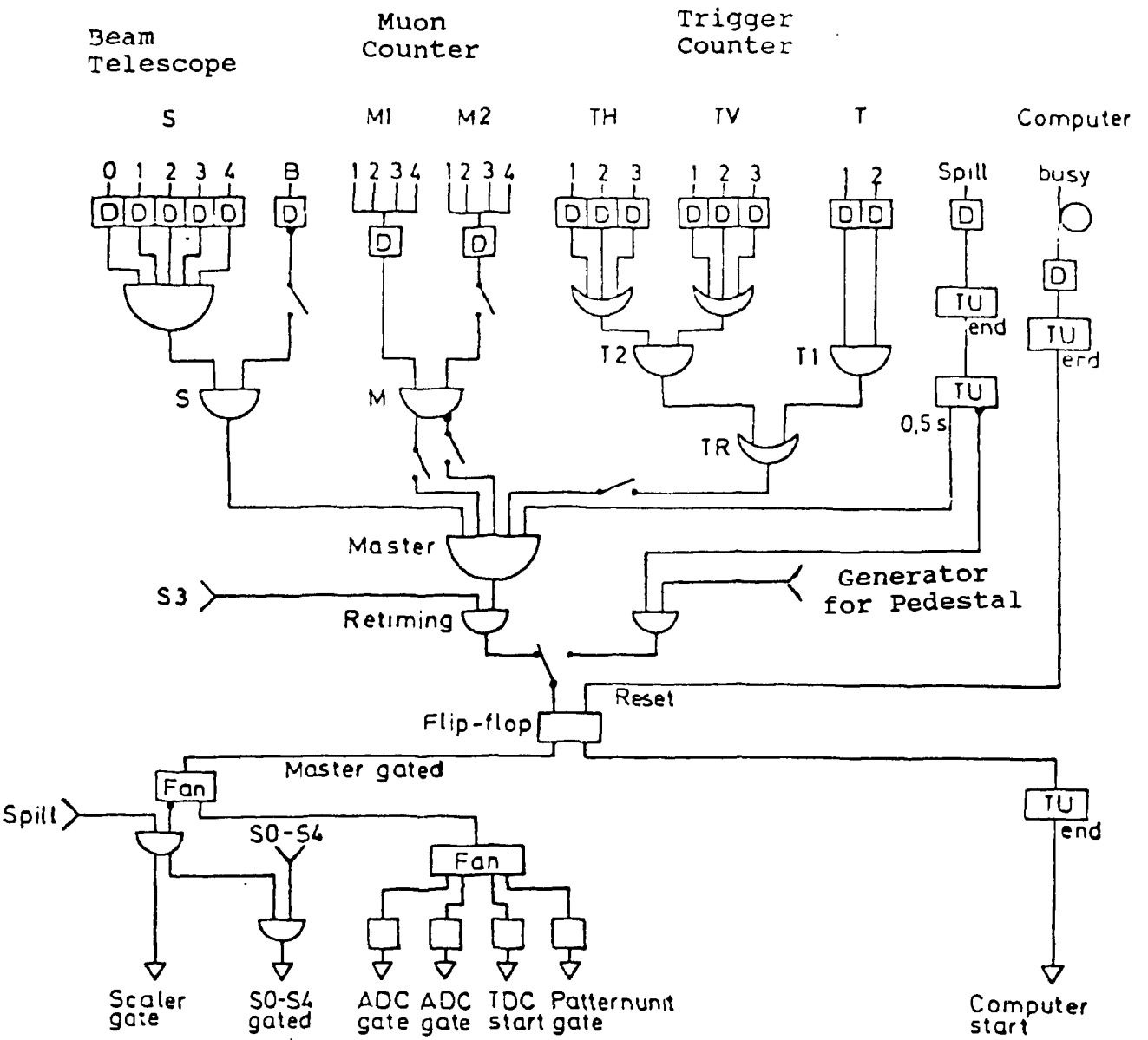

Block Circuit Diagram of the Trigger.

Fig. 25

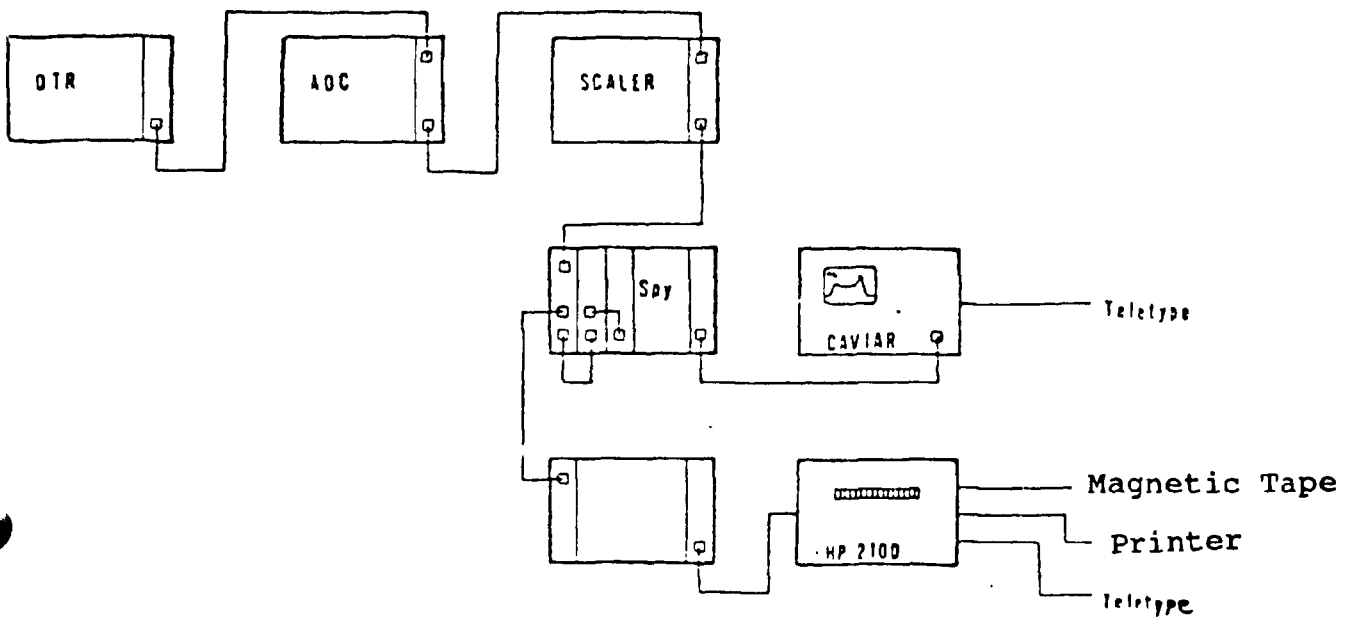

Block Circuit Diagram of the Measured-Date Acquisition and the Connection to the Monitor.

Fig. 26

On-line display of a hadron event
with trigger counters activated

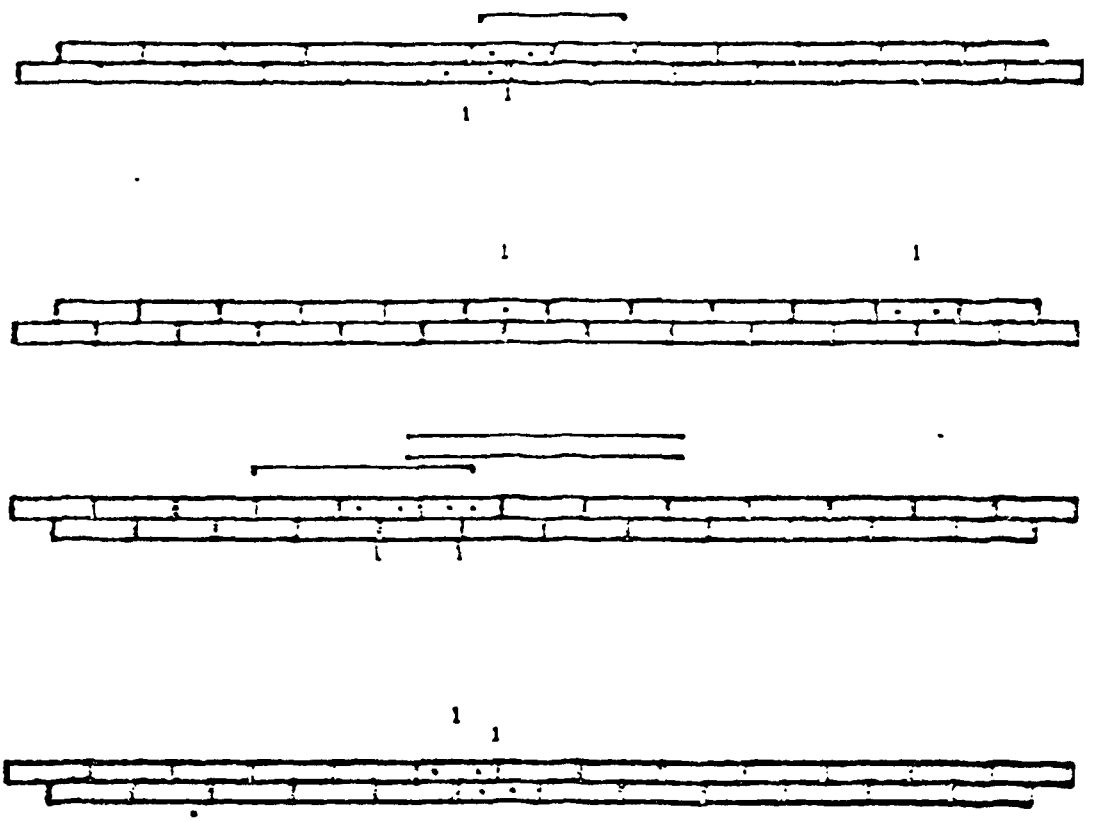

Picture of a Hadron Event from the On-Line Display.

Fig. 27

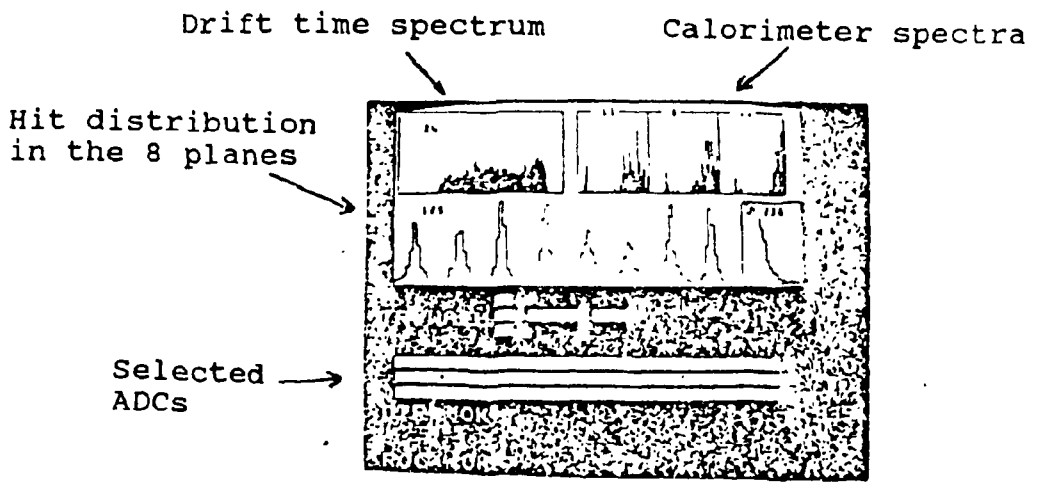

CAVIAR On-line monitor

Polaroid Picture of the Monitor Display Screen.

Fig. 28

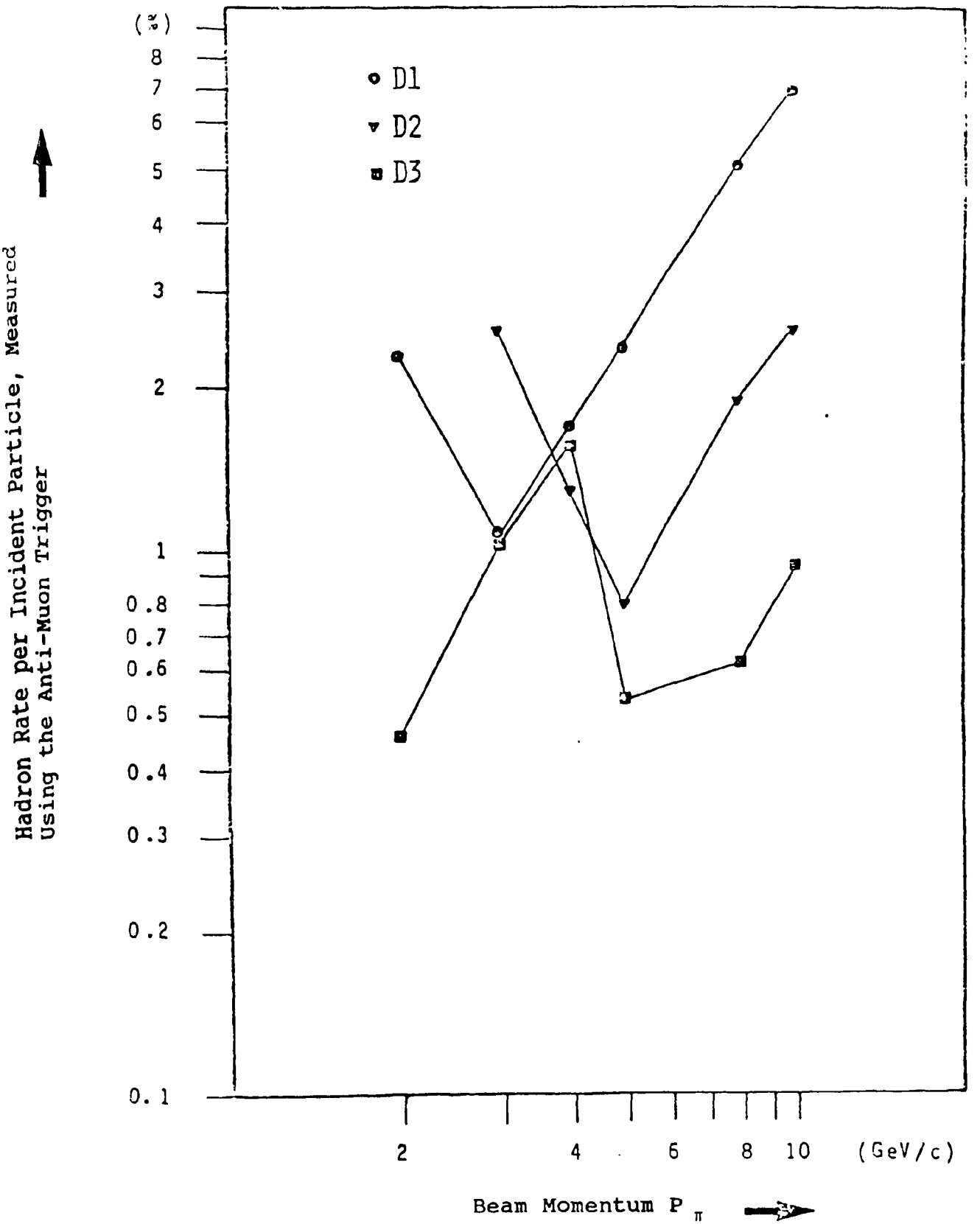

Fig. 29

Acceptance of the Anti-Muon Trigger as Function of Beam Momentum.

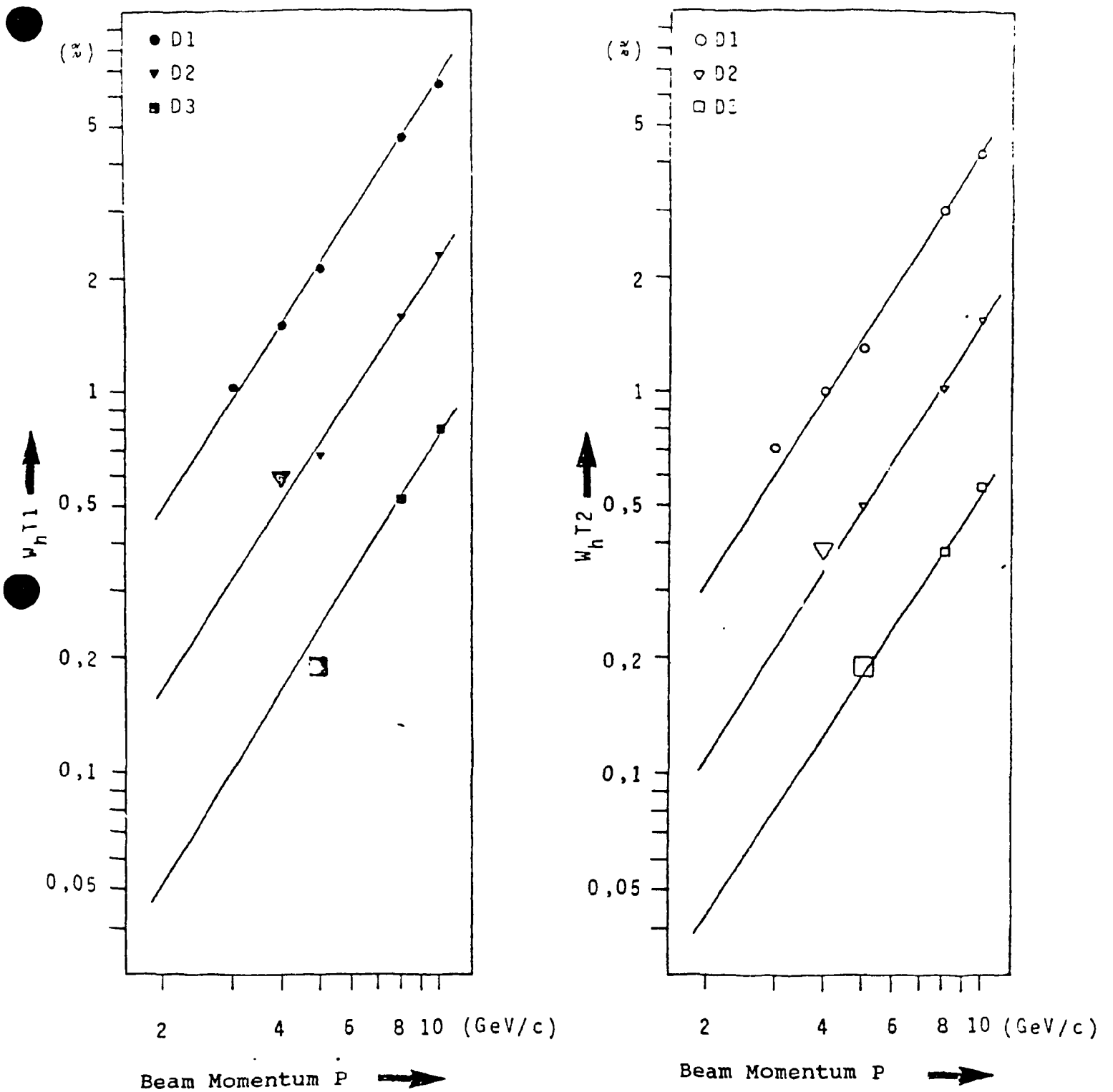

Exit Probability for Hadrons from the Hadron Calorimeter, Measured in Front of and Behind the Muon Chamber, as Function of the Beam Momentum.

Fig. 30

Measurement of the Damping Length for Hadron Showers

Damping by 20 cm of iron between T1 and M1
○ at D1 ▽ at D2 □ at D3

Damping by Inserting Additional Calorimeters
○ from D1 to D2 ▽ from D2 to D3

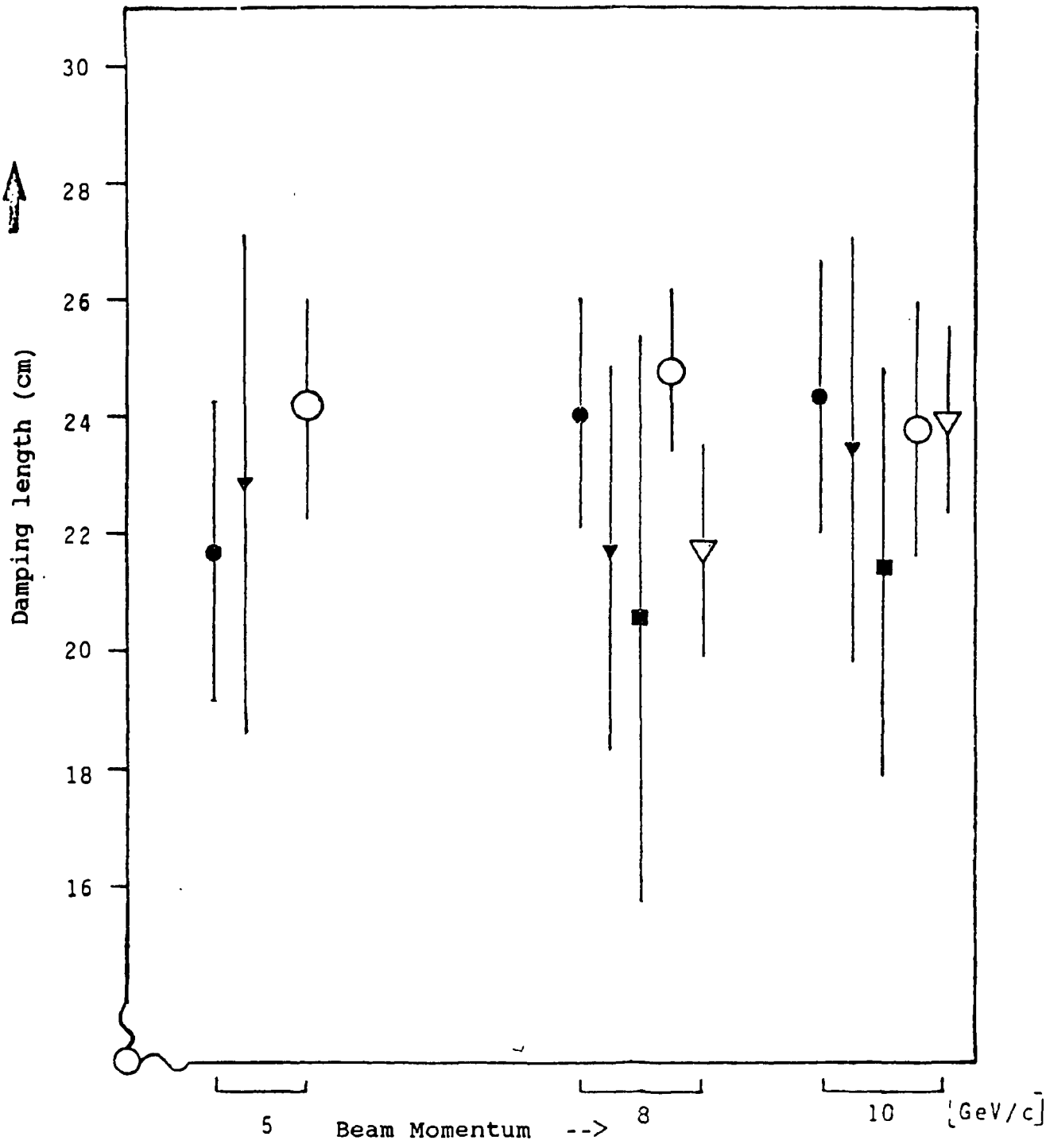

Measured Damping Lengths for Decaying Hadron Showers in Iron.

Fig. 31

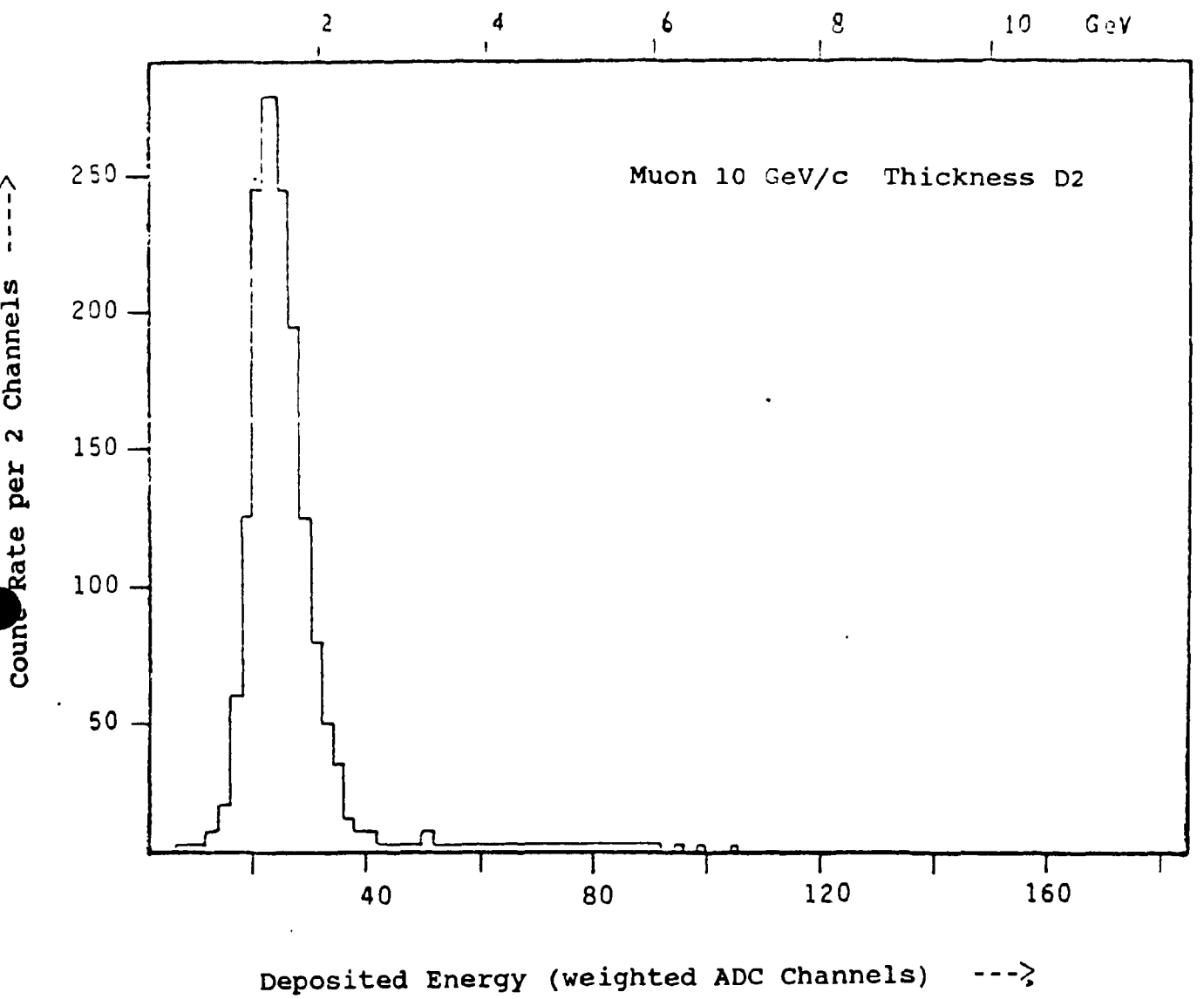

The Muon Energy Spectrum. The total energy, the sum of the energies deposited in all the calorimeters is shown.

Fig. 32

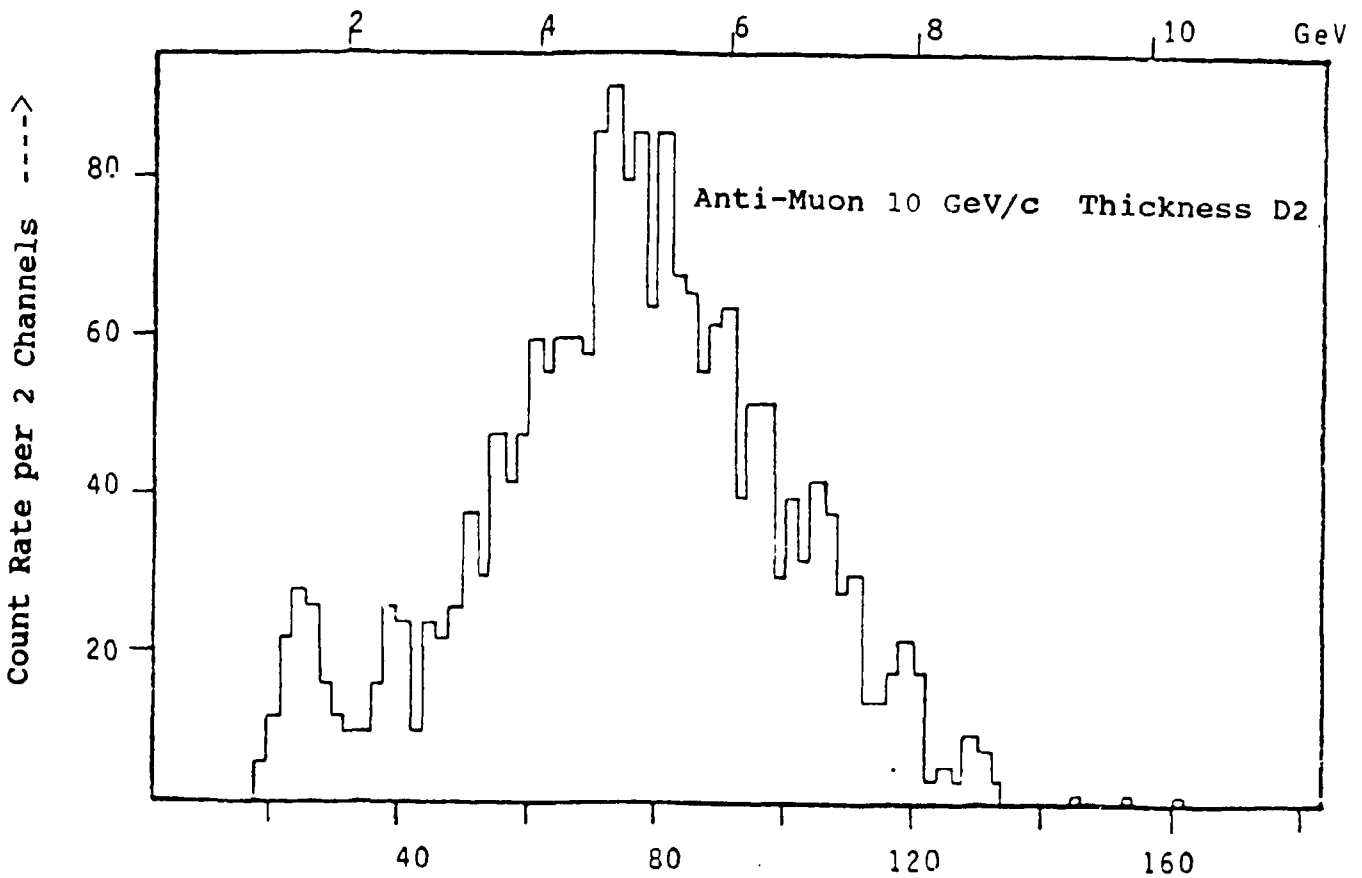

Energy Spectrum of a Punch-Through Event for the Same Momentum as in Fig. 32.

Fig. 33

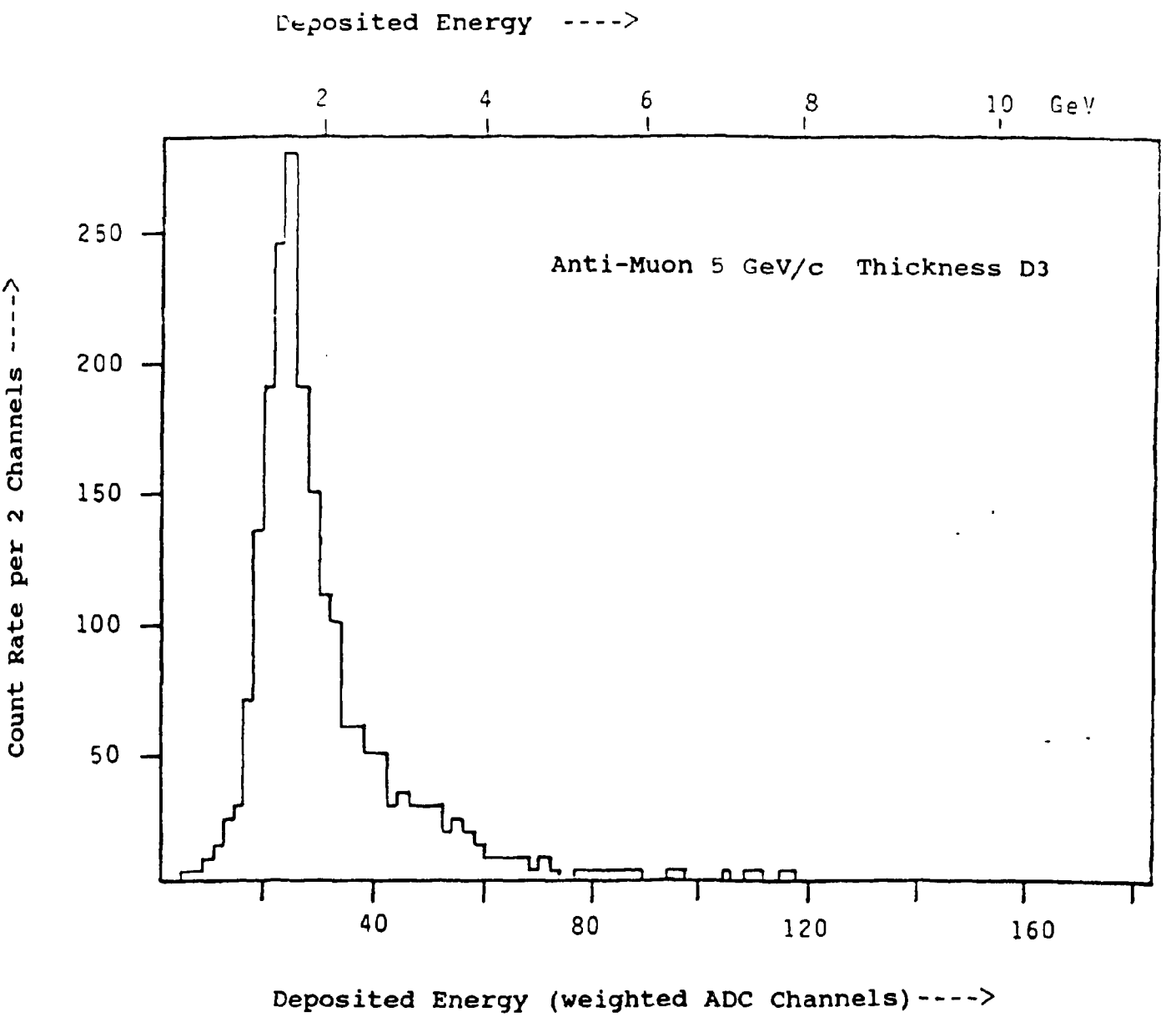

Energy Spectrum of a Punch-Through Event. This time the momentum is 5 GeV/c and the thickness is D3.

Fig. 34

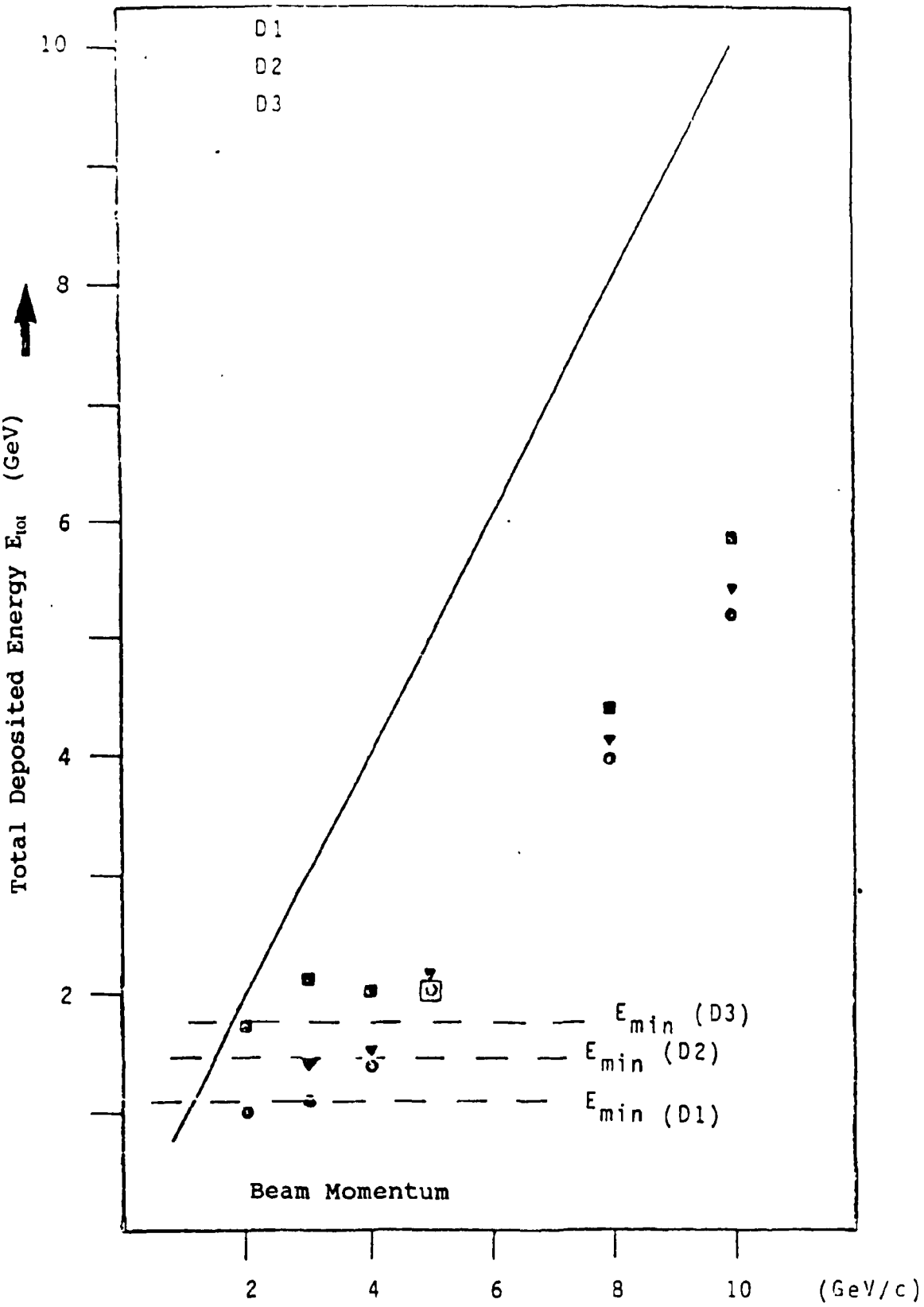

Fig. 35 Total Energy Deposited in all the Calorimeters, Collected with the Anti-Muon Trigger, Plus the Energies of the Minimum-Ionization Particles (dashed line). The solid line designates the expected energy for total absorption in the calorimeter.

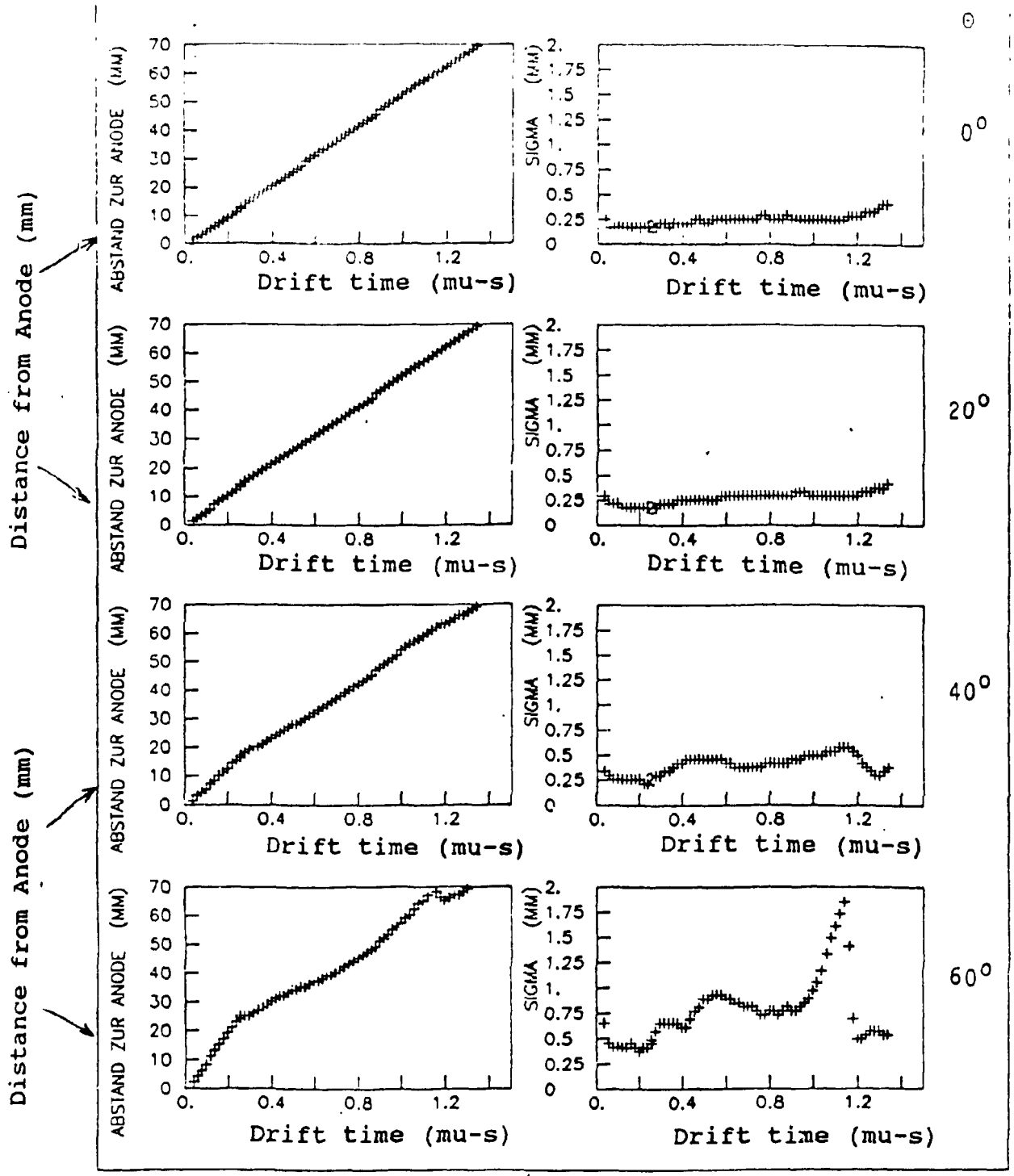

Calibration of the Drift Tube Used for
Incidence Angles of 0°, 20°, 40°, and 60°

The Place-Time relation and Spatial Resolution are shown for each case

The Calibration Used for the Drift Tubes.

Fig. 36

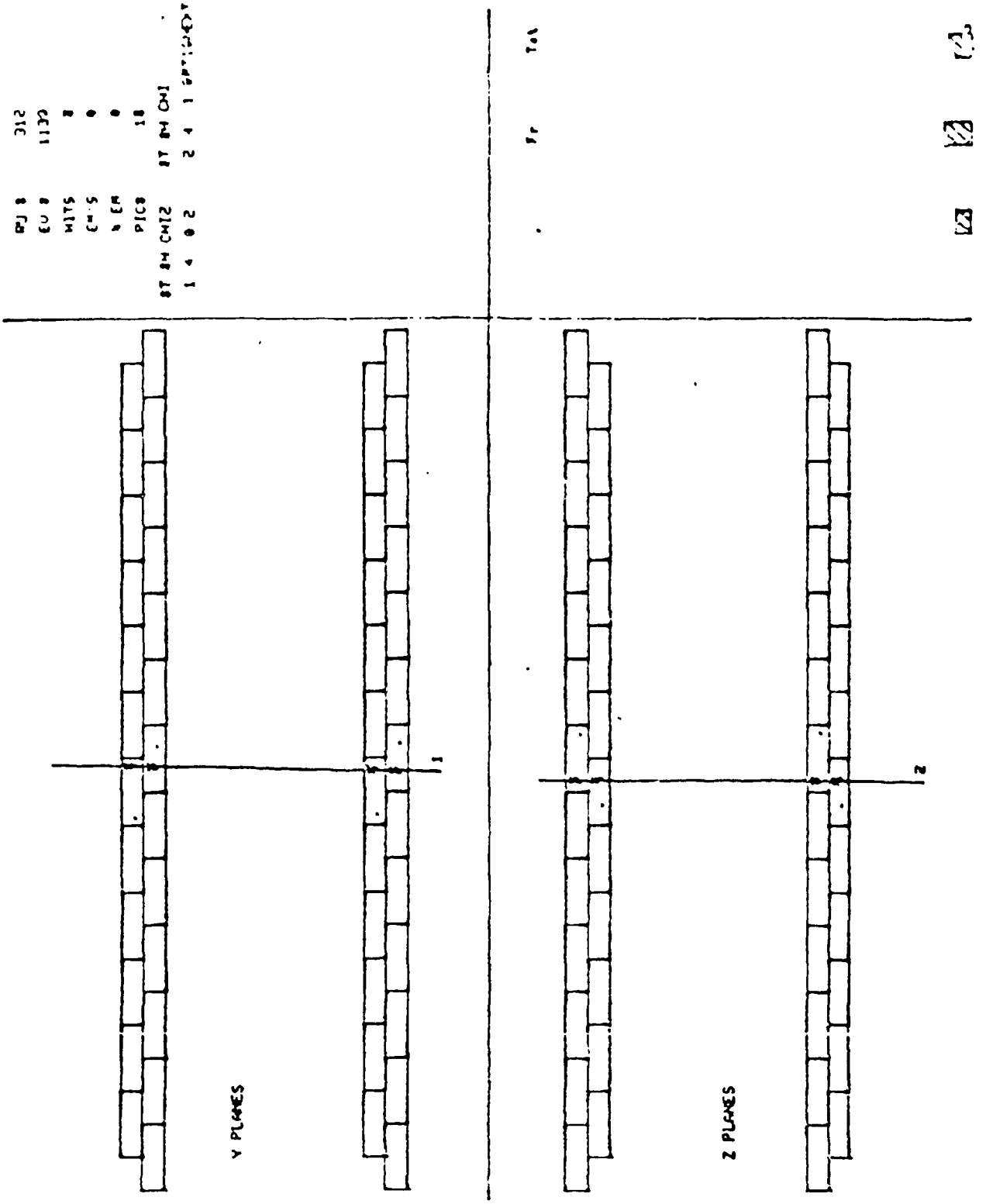

Display of a 10 GeV/c Muon. The particle beam is incident from the bottom in all the display images.

Fig. 37

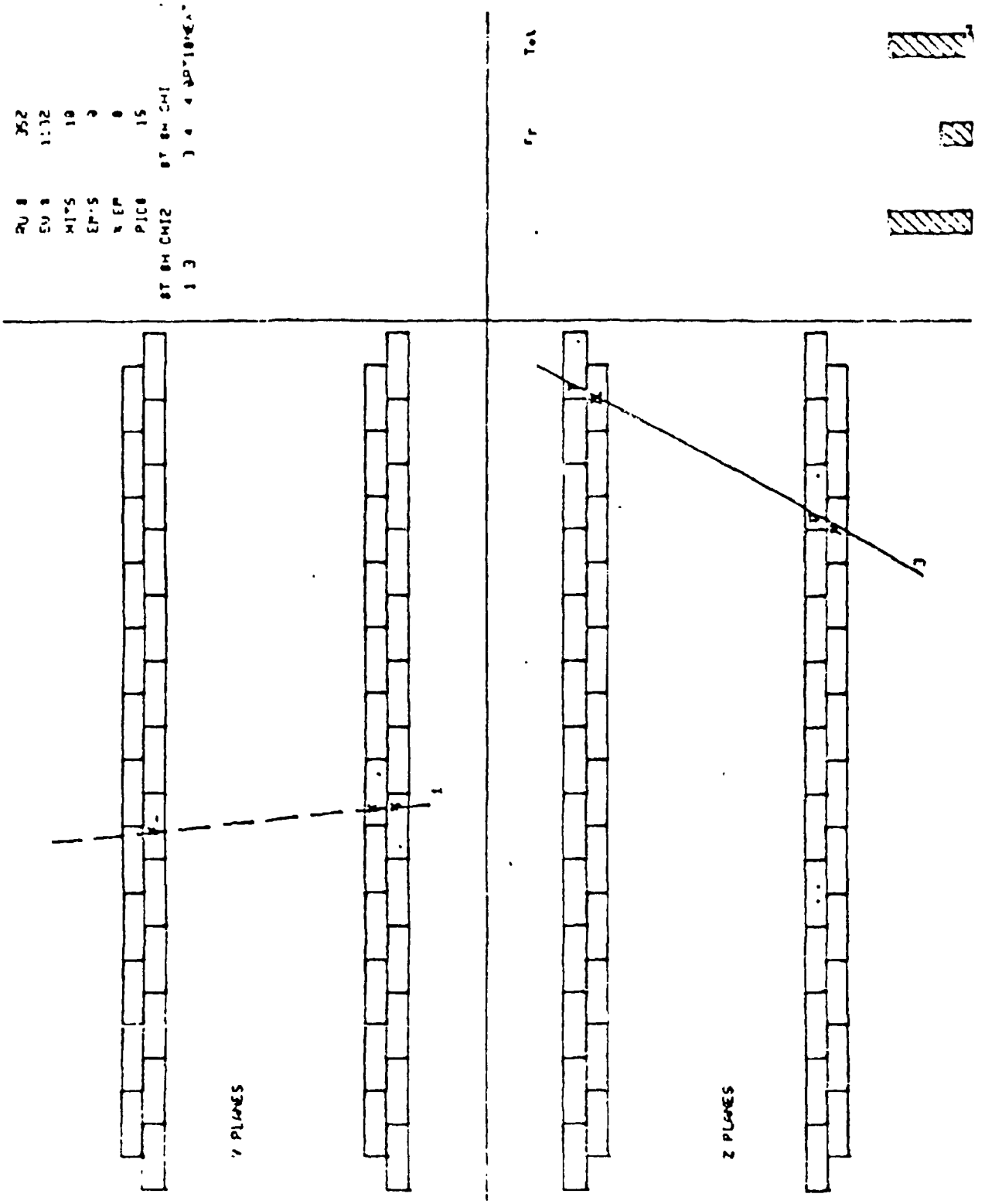

Punch-Through Event at 10 GeV/c.

Fig. 38

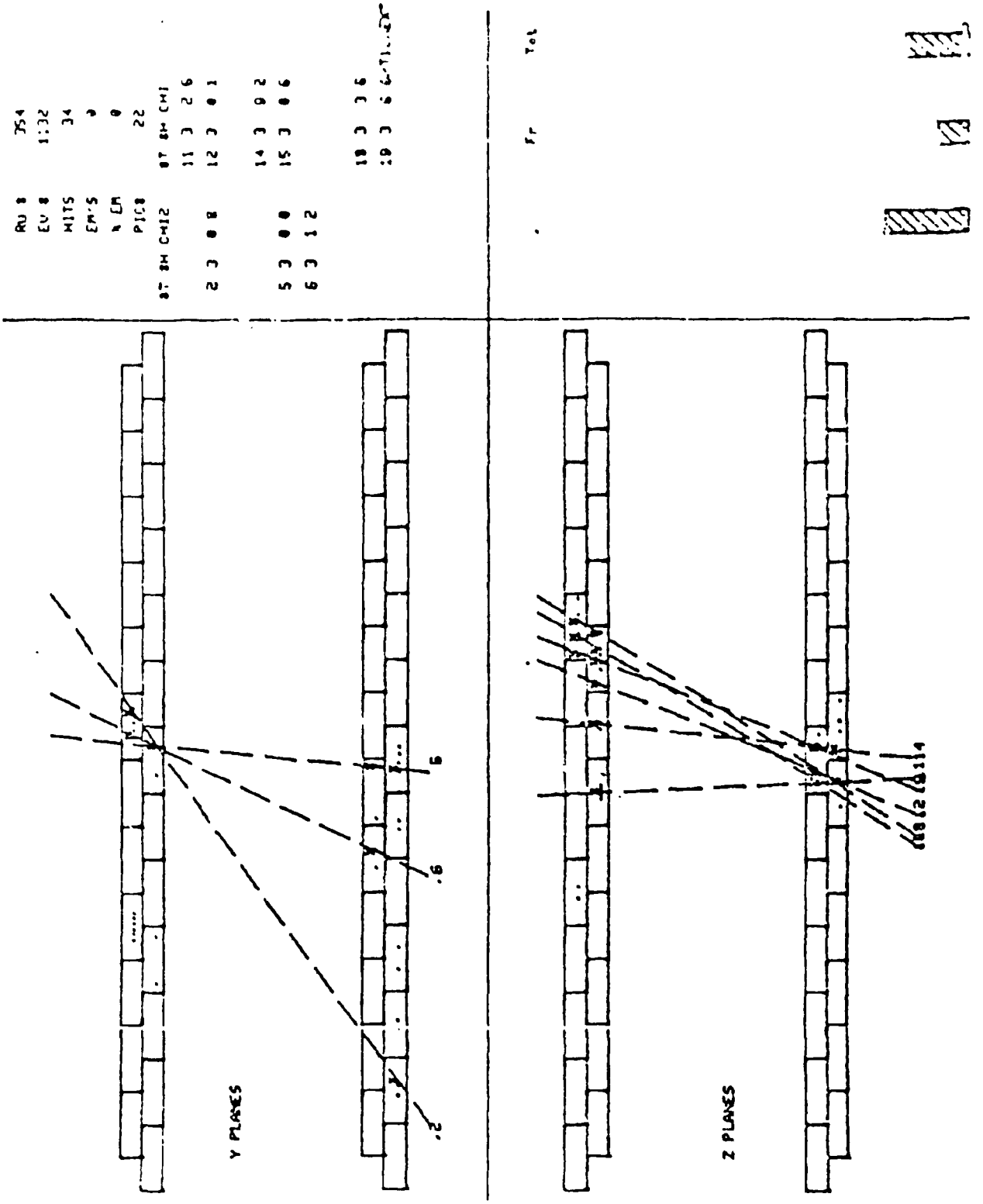

Like 38.

Fig. 39

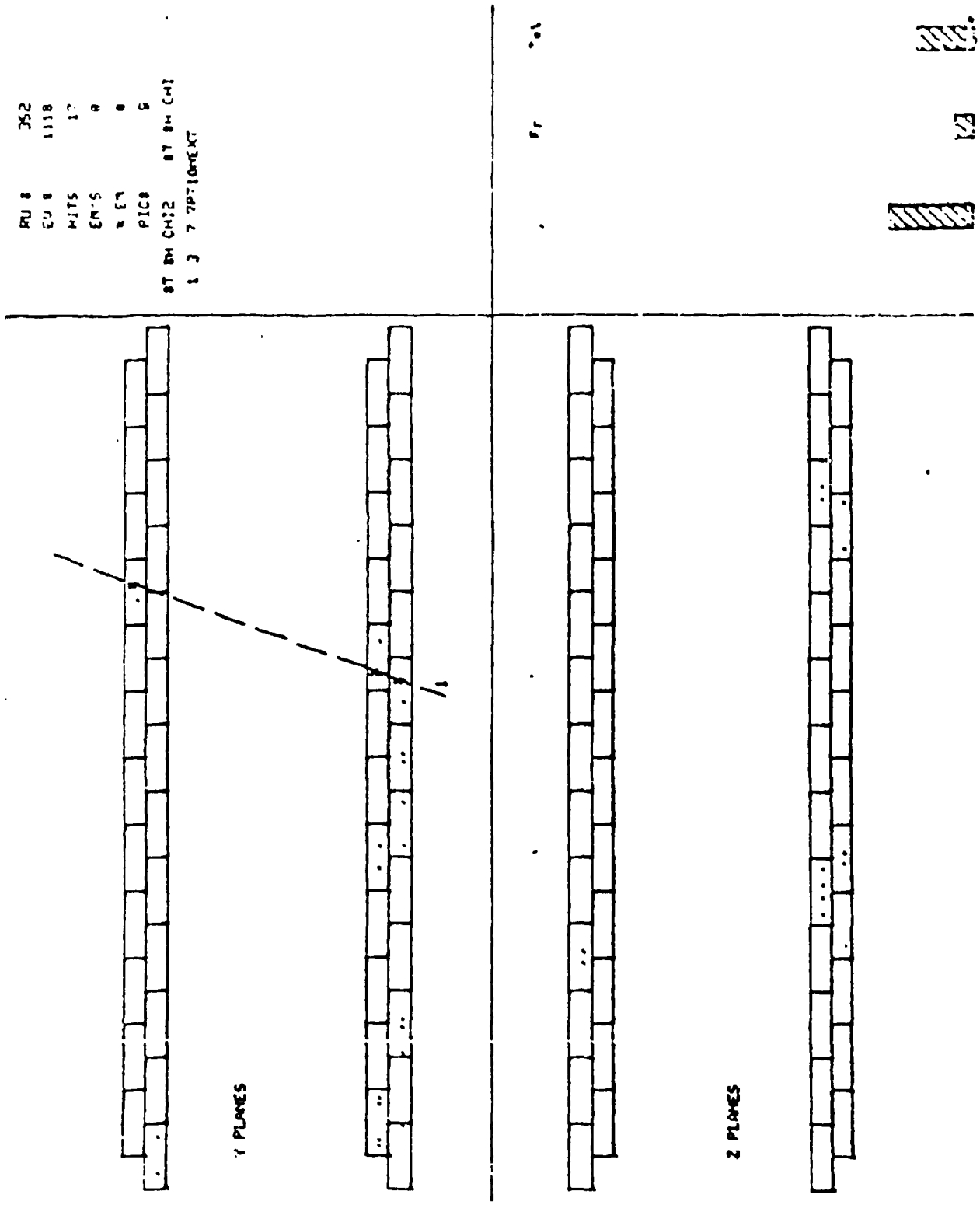

Like 38

Fig. 40

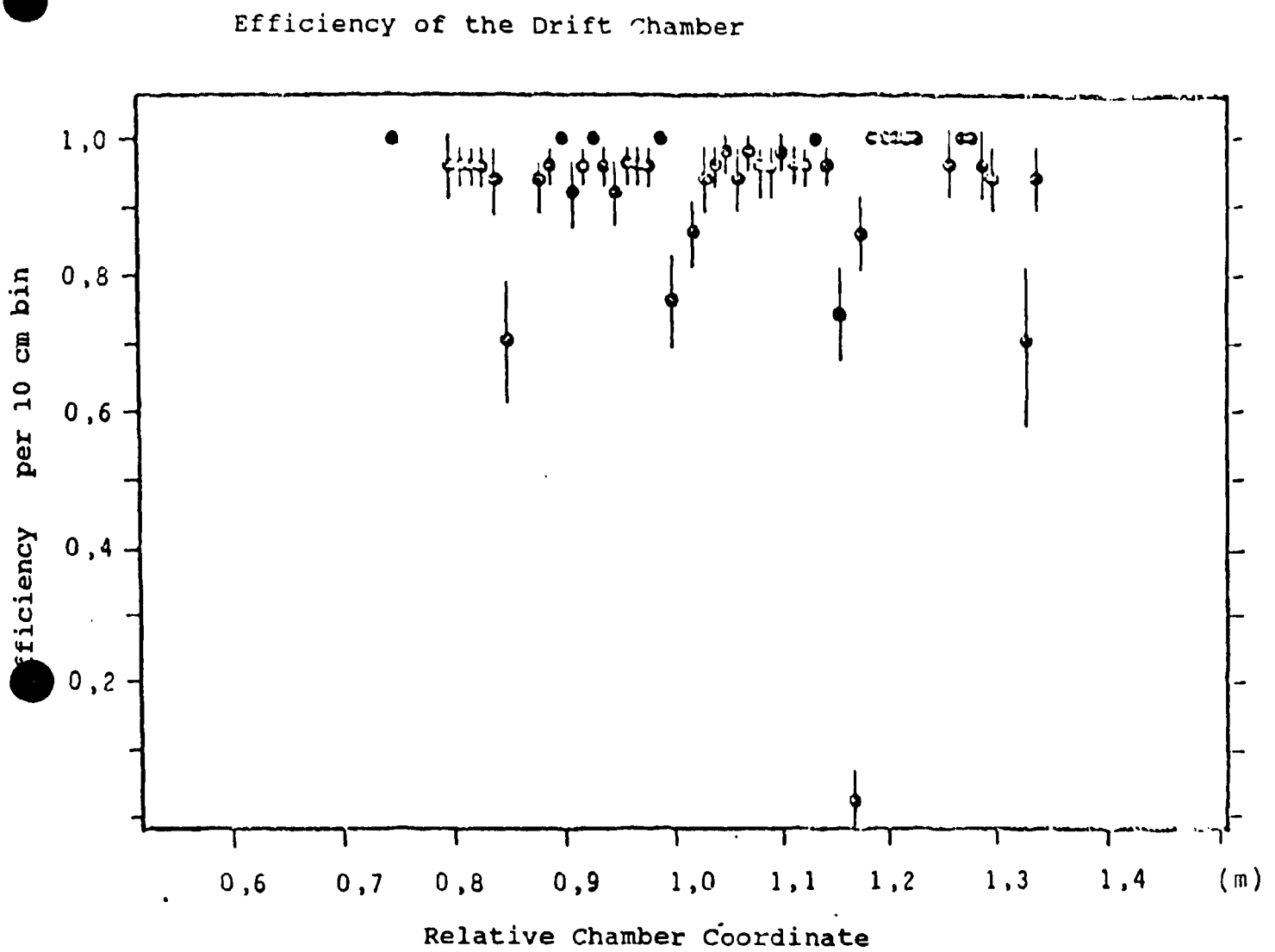

Efficiency of the Muon Chamber as Function of a Relative Chamber Coordinate.

Fig. 41

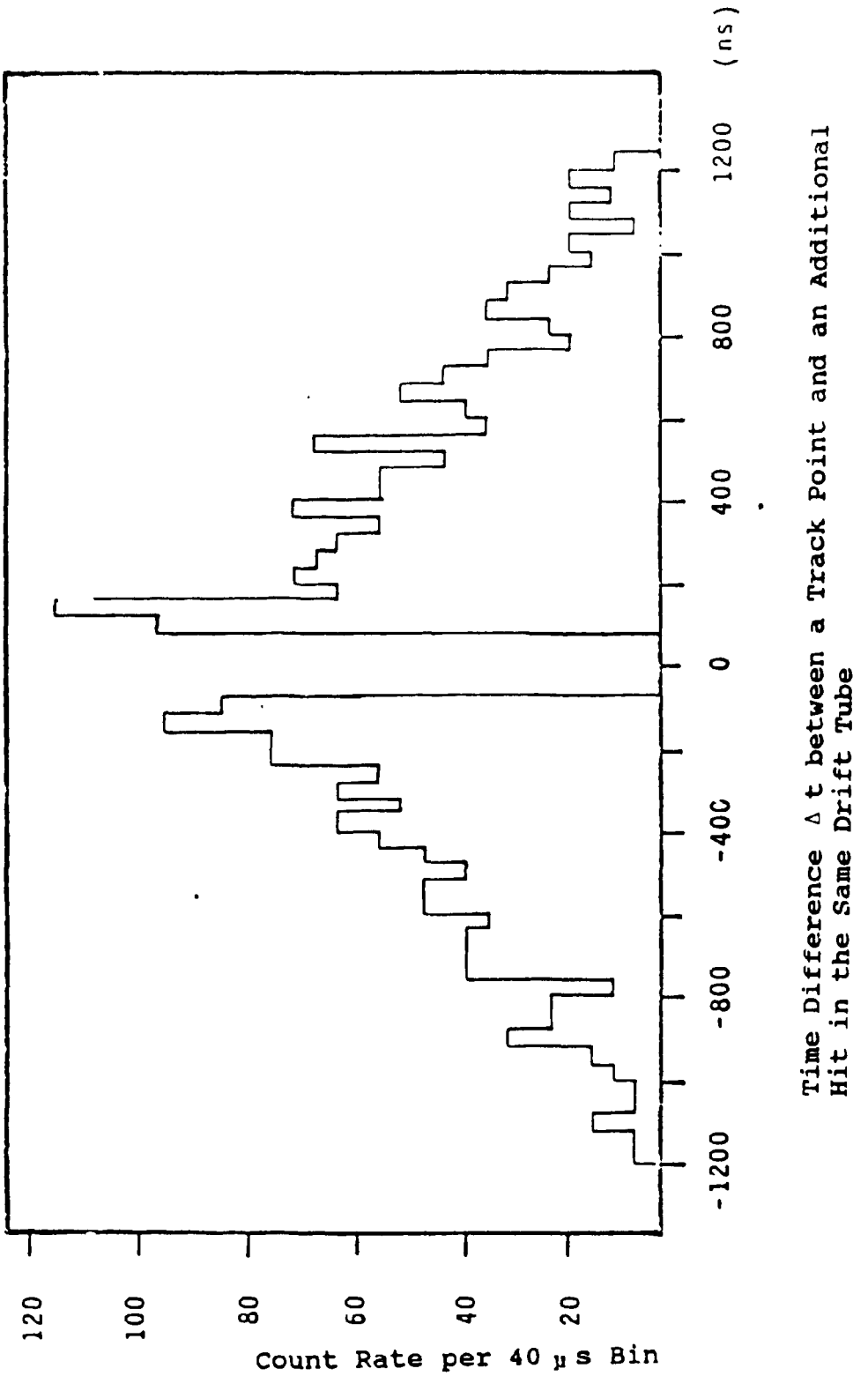

Time Difference Spectrum dN/d(Δt). The Difference is formed between a point on the track and the next hit in the drift tube.

Fig. 42

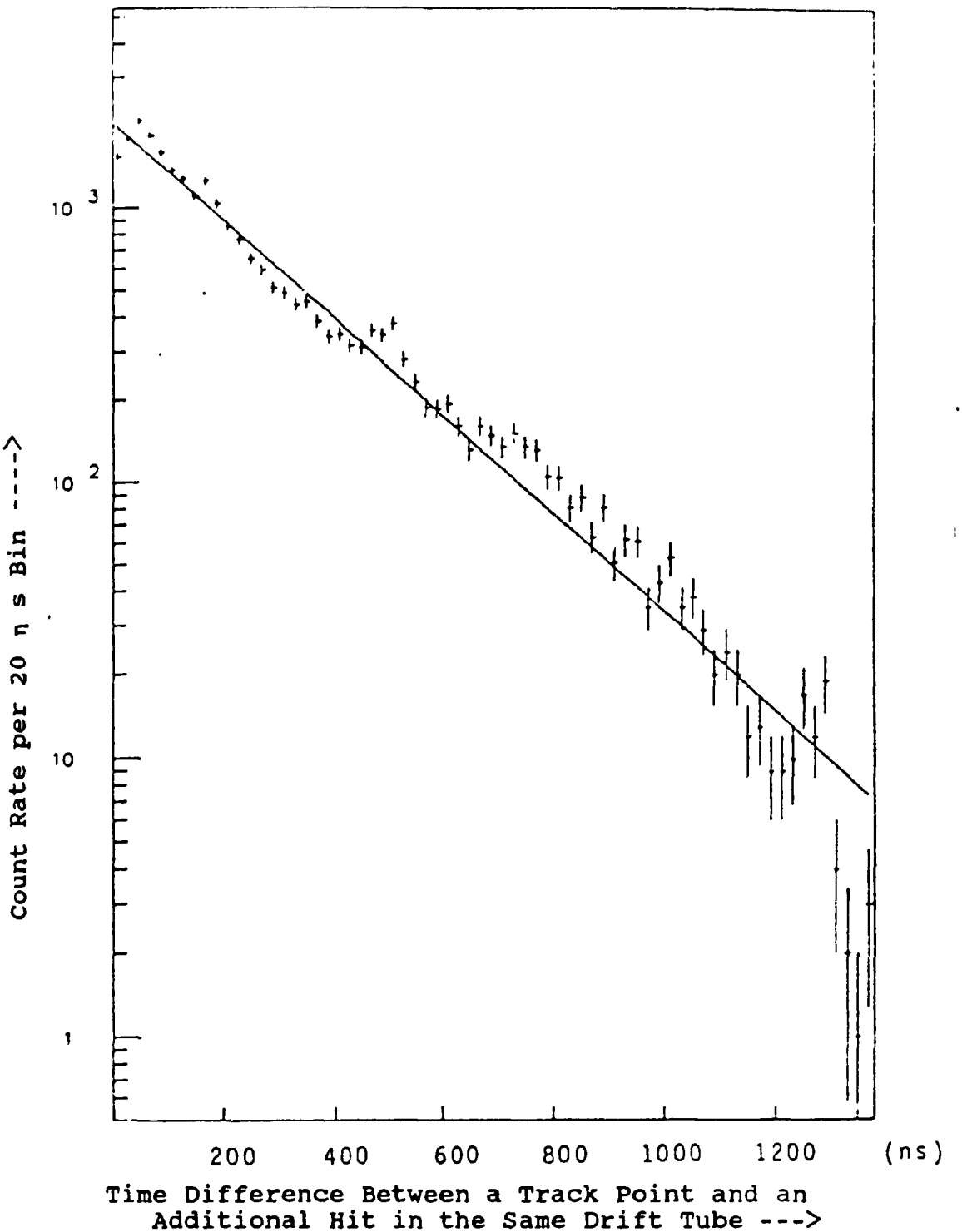

One Side of the Time Difference Spectrum with an Exponential Fit.

Fig. 43

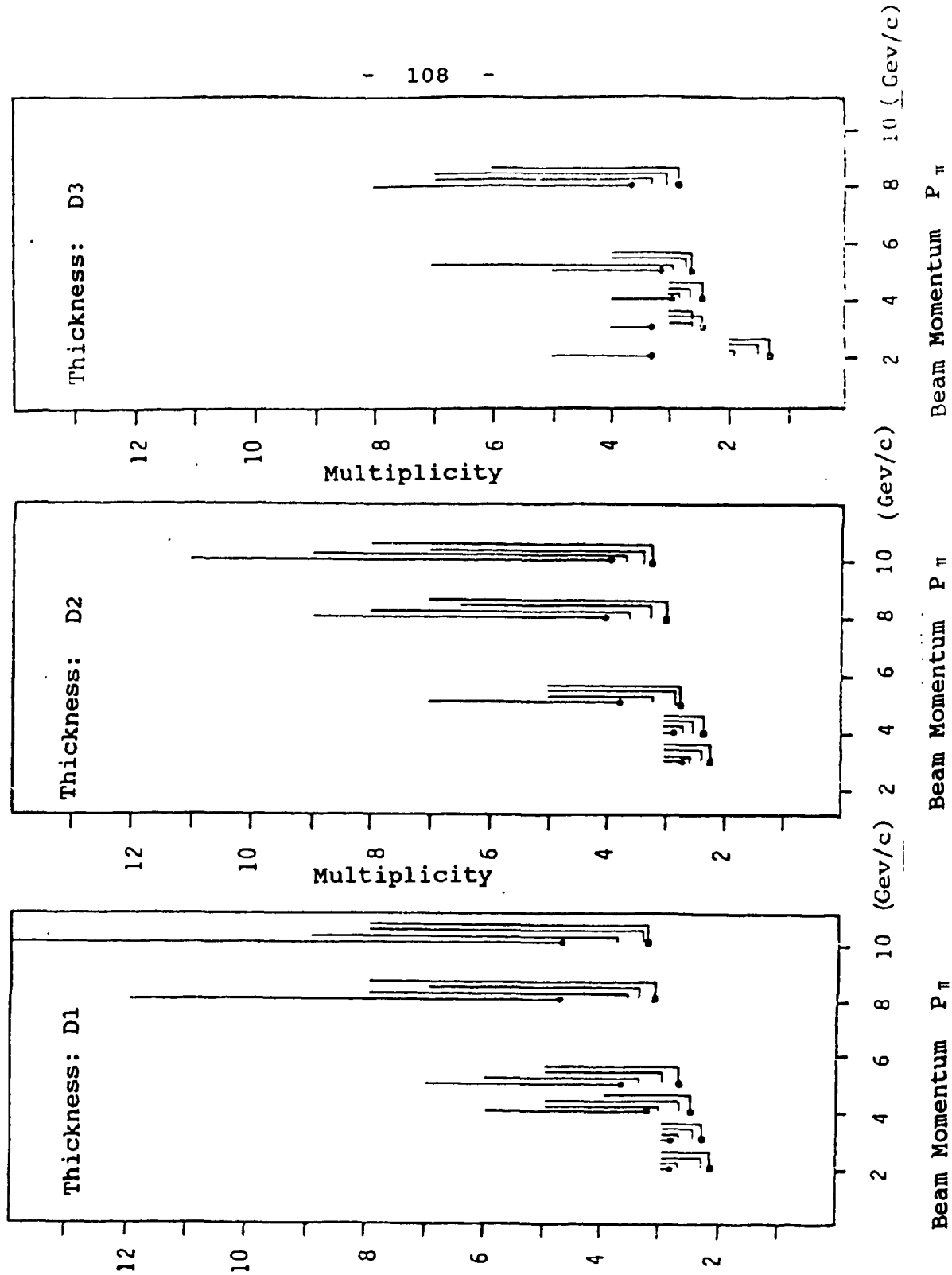

Average Hit Multiplicities and the 90% Limit of the Individual Distributions as Function of the Beam Momentum for Three Different Absorber Thicknesses.

Fig. 44

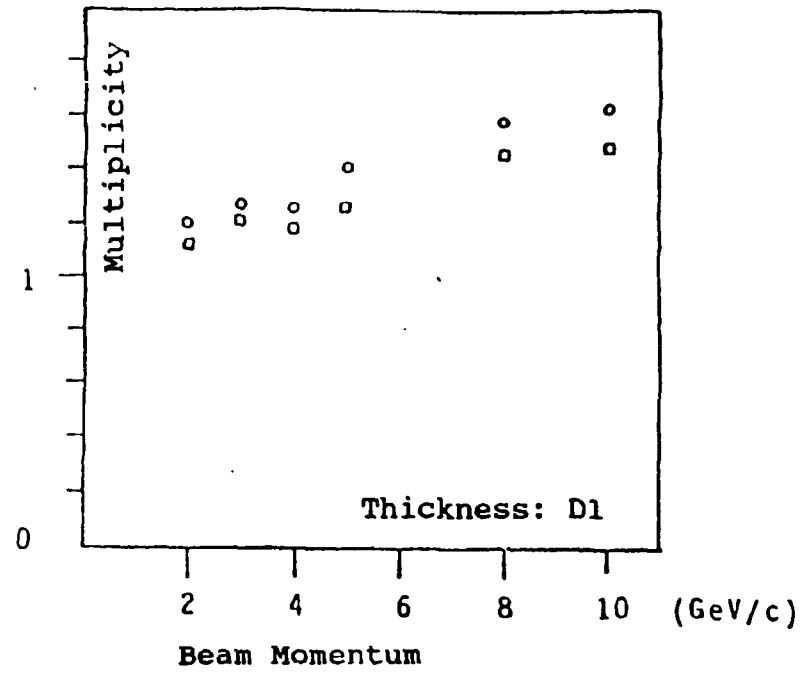

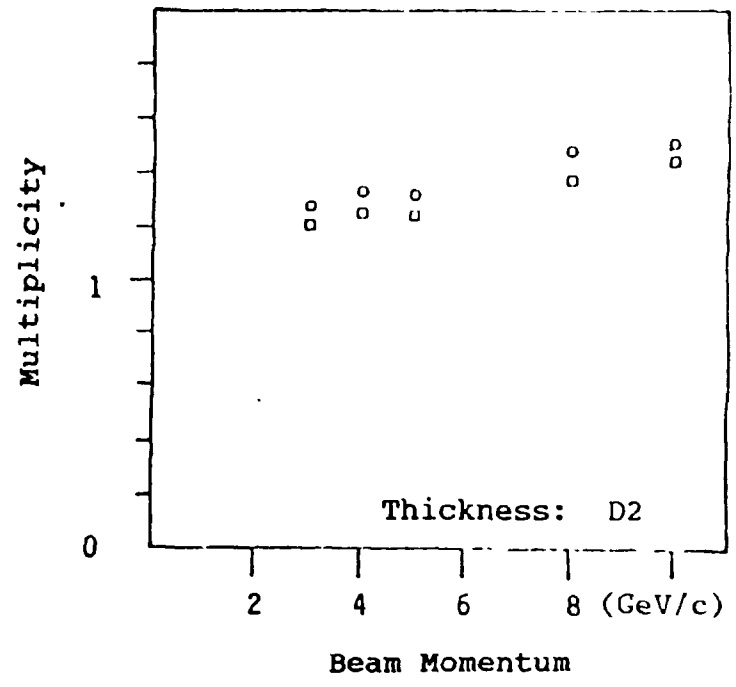

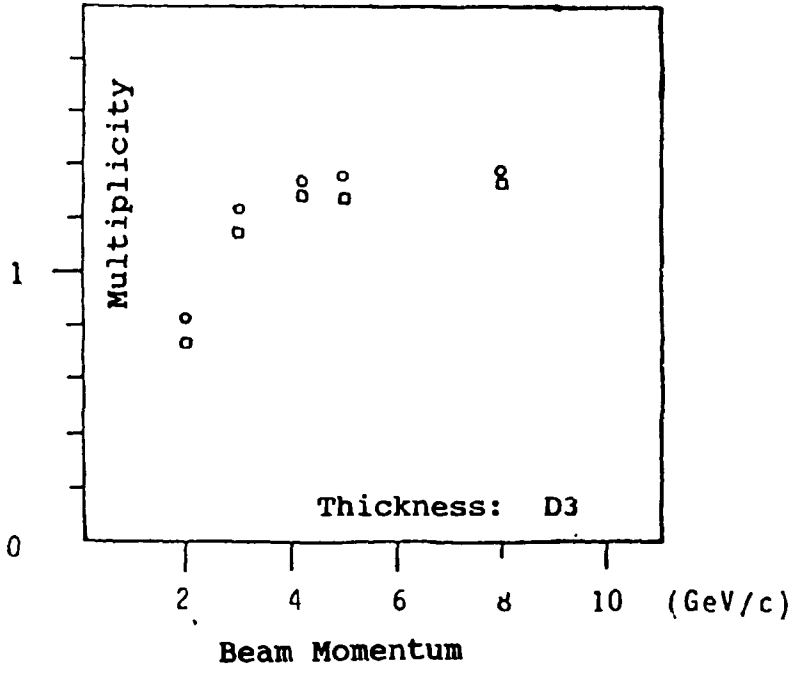

Mean Track Multiplicities in

Projection Y ○

Projection Z □

Fig. 45 Average Track Multiplicities as Function of the Beam Momentum.

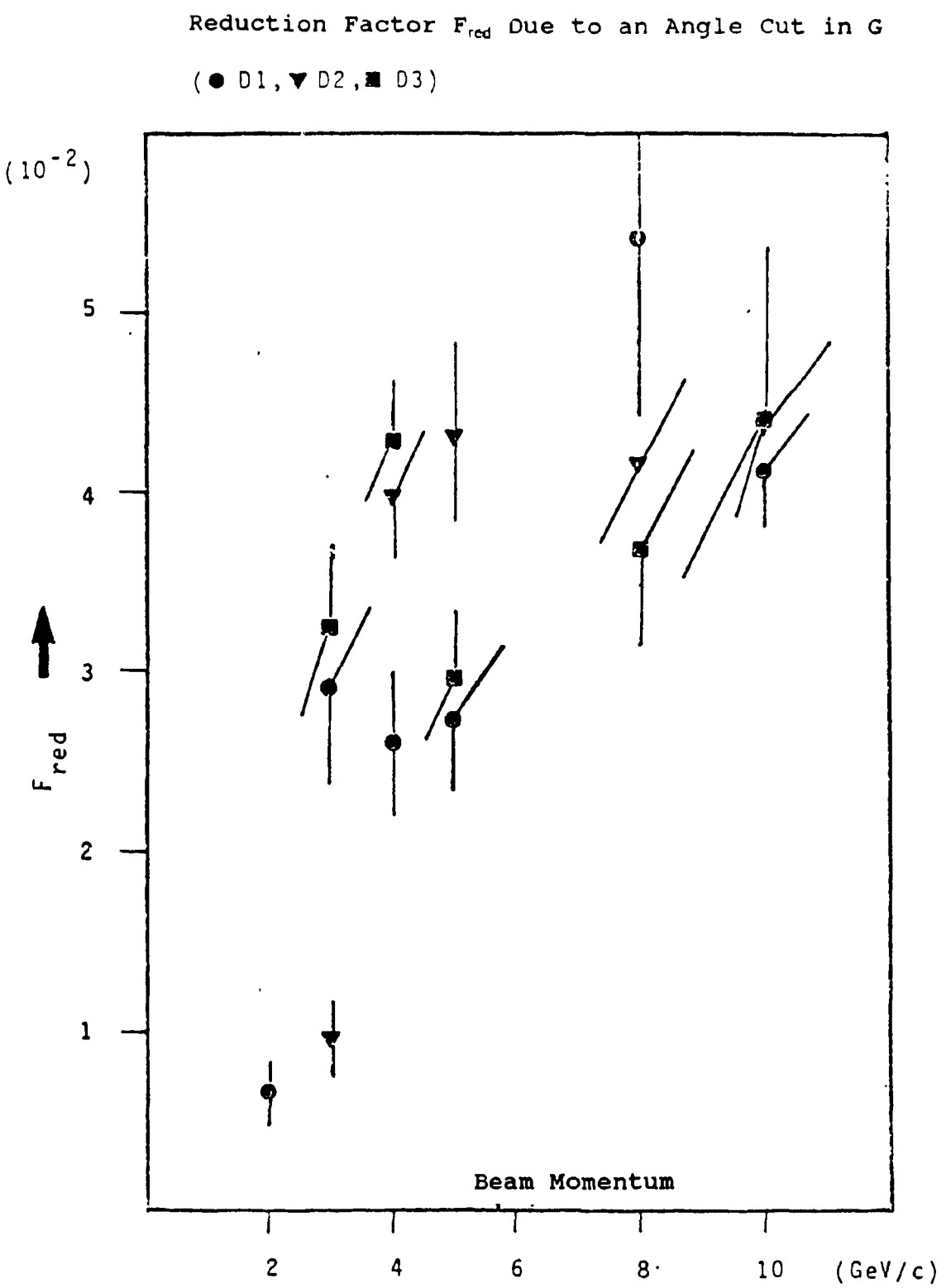

Reduction Factor F_{red} of the Hadronic Background by an Angle Cut in G.

Fig. 46

Biography

[redacted]

1962-1966	Attended Evangelical Public School in Wuppertal-Elberfeld.
1966-1974	Attended State Natural Sciences Gymnasium, Wuppertal-Elberfeld
6/10/1974	Baccalaaureate Examination (Reifeprüfung)
WS 1974/75	Enrolled in the RWTH Aachen, major in Physics
4/25/1977	Physics-Diplomate Preliminary Examination
July 1979 - September 1979	Stipend as summer student at the European Nuclear Research center CERN
September 1979 - December 1981	Stay at CERN to build the muon detector for the UA1 Experiment in the $p\bar{p}$ Project
July 1981 - October 1982	Preparation of the Diploma Thesis in the Third Physical Institute und the Direction of Priv. Doz. Dr. K. Eggert: "Messung des hadronischen Untergrundes bei der Identifizierung von Myonen" (Measurement of the Hadronic Background in the Identification of Muons)